

**ROLES OF NANOFILLER STRUCTURE ON MECHANICAL
BEHAVIOR OF THERMOPLASTIC NANOCOMPOSITES**

A Dissertation

by

JONG IL WEON

Submitted to the Office of Graduate Studies of
Texas A&M University
in partial fulfillment of the requirements for the degree of

DOCTOR OF PHILOSOPHY

August 2005

Major Subject: Mechanical Engineering

**ROLES OF NANOFILLER STRUCTURE ON MECHANICAL
BEHAVIOR OF THERMOPLASTIC NANOCOMPOSITES**

A Dissertation

by

JONG IL WEON

Submitted to the Office of Graduate Studies of
Texas A&M University
in partial fulfillment of the requirements for the degree of

DOCTOR OF PHILOSOPHY

Approved by:

Chair of Committee,
Committee Members,

Head of Department,

Hung-Jue Sue
David M. Ford
Terry S. Creasy
Chii-Der S. Suh
Dennis O'Neal

August 2005

Major Subject: Mechanical Engineering

ABSTRACT

Roles of Nanofiller Structure on Mechanical Behavior of Thermoplastic

Nanocomposites. (August 2005)

Jong Il Weon, B.S., Dongguk University;

M.S., Sungkyunkwan University

Chair of Advisory Committee: Dr. Hung-Jue Sue

The roles of nanofiller structural parameters, such as filler shape, aspect ratio and orientation, on mechanical properties of thermoplastic nanocomposites have been studied. A commercial grade nylon-6/clay nanocomposite is subjected to a large-scale simple shear orientation process and the resulting morphology is investigated on various length scale levels. Both the orientation and the aspect ratio of nanoclays, which can be altered by the simple shear process, have been studied. The incorporation of well-dispersed nanoclays into the nylon-6 matrix greatly reduces the chain mobility as well as the crystallinity of nylon-6. The exfoliated nanocomposites show that the global orientation of clay layers dictates the orientation of crystalline lamellae. Two types of lamellar orientation are observed, as revealed by small-angle X-ray scattering. One type of lamellae is oriented $\sim 41^\circ$ away from the clay surface, whereas the simple shear process induces another weak preferred lamellar orientation nearly perpendicular to the clay surface. The formation of those lamellar orientations appears to be related to both

orientation of the clay in the nanocomposite and the simple shear process. It is found that the modulus, strength, and heat distortion temperature of the nanocomposites decrease as the clay aspect ratio and degree of orientation are reduced. The micromechanics-based models accurately describe the relationship between clay structural parameters and the corresponding moduli for exfoliated nanocomposites. The impact fracture mechanisms of polypropylene (PP)-calcium carbonate (CaCO_3) nanoparticles have been investigated. A detailed investigation reveals that the CaCO_3 nanoparticles act as stress concentrators to initiate massive crazes, followed by shear banding in the PP matrix.

DEDICATION

To my parents, my brothers and my wife, So Hee.

ACKNOWLEDGEMENTS

This document would not have been possible without the encouragement and help from Dr. H.-J. Sue. My deepest appreciation is given to him for his guidance and inspiration throughout my graduate study. I also wish to thank to my committee members, Dr. Terry S. Creasy, Chii-Der S. Suh and David M. Ford for their valuable advice, guidance and understanding.

I am grateful to Dr. Andreas Holzenburg, Dr. Zhiping Luo and Ms. Ann Ellis at the Microscopy and Imaging Center for their extensive instructions with TEM works. Special thanks are given to Mr. Eddy I. Garcia-Meitin at the Dow Chemical Co. for his help on TEM sample preparation. I extend my appreciation to Dr. Alex J. Hsieh of the US Army lab for his discussion and Dr. Nattamai Bhuvanesh of the X-ray Diffraction Lab in the Department of Chemistry, Texas A&M University for his professional help with small-angle X-ray scattering experiments.

The research funding by the Defense Logistic Agency (Contract #SP0103-02-D-0024) and the State of Texas ARP Grant (000512-00137-2001) are greatly appreciated.

I have greatly benefited from working with my colleagues in my research group, Dr. Jim Lu, Dr. Zhiyong Xia, Dr. Masaya Kotaki, Dr. Ki Tak Gam, Goy Tech Lim, Woong-Jae Boo and Francisco Tschen. Their friendship and unconditional support will always be remembered.

TABLE OF CONTENTS

	Page
ABSTRACT	iii
DEDICATION	v
ACKNOWLEDGEMENTS	vi
TABLE OF CONTENTS	vii
LIST OF TABLES	x
LIST OF FIGURES.....	xi
CHAPTER	
I INTRODUCTION.....	1
1.1 Polymer-Clay Nanocomposites.....	2
1.2 Polymer-CaCO ₃ Nanocomposites.....	2
1.3 Research Objectives and Significance	3
1.4 Dissertation Outline.....	4
II BACKGROUND AND LITERATURE REVIEW.....	6
2.1 Introduction.....	6
2.2 Characterization of Polymer Nanocomposites.....	7
2.2.1 Structure of layered silicate.....	7
2.2.2 Dispersion of nanofillers in polymer matrix	8
2.2.3 <i>In-situ</i> polymerization of nylon-6/clay nanocomposite	11
2.3 Continuum-based Micromechanical Models	12
2.3.1 Conventional filler-based micromechanical models.....	13
2.3.2 Effective filler-based micromechanical models.....	15
2.3.3 Shear lag model.....	17
2.4 Fracture Behaviors of Polymer Nanocomposites.....	18
2.4.1 Toughness evaluation.....	18
2.4.2 Toughening mechanism observation.....	20
III EFFECTIVENESS OF A SIMPLE SHEAR PROCESS ON ALTERATION OF NANOFILLER STRUCTURES IN POLYMER NANOCOMPOSITES	24
3.1 Introduction.....	24

CHAPTER	Page
3.2 Experimental	25
3.2.1 Materials	25
3.2.2 Sample preparation	25
3.2.3 ECAE process	26
3.2.4 Sample annealing	28
3.2.5 Differential scanning calorimetry (DSC) measurement	28
3.2.6 Density measurement	29
3.2.7 Microscopy observation	29
3.3 Results and Discussion	30
3.3.1 Sample annealing observation	30
3.3.2 DSC analysis and density measurement	32
3.3.3 Microscopy investigation	34
3.4 Summary	36
 IV MORPHOLOGICAL CHARACTERIZATION OF NYLON-6 NANOCOMPOSITE FOLLOWING A LARGE-SCALE SIMPLE SHEAR PROCESS	37
4.1 Introduction	37
4.2 Experimental	39
4.2.1 Materials	39
4.2.2 Morphology characterization	40
4.2.3 X-ray characterization	40
4.2.4 DSC measurements	42
4.3 Results and Discussion	43
4.3.1 Morphological characterization of nylon-6 nanocomposites	43
4.3.2 Morphological characterizations of neat nylon-6	47
4.4 Summary	65
 V EFFECTS OF CLAY ORIENTATION AND ASPECT RATIO ON MECHANICAL BEHAVIOR OF NYLON-6 NANOCOMPOSITE	66
5.1 Introduction	66
5.2 Continuum-based Micromechanical Models	68
5.3 Experimental	70
5.3.1 Materials	70
5.3.2 Sample preparation	70
5.3.3 Microscopy and image analysis	71
5.3.4 Mechanical testing	73
5.4 Results and Discussion	75
5.4.1 Microscopy investigation and image analysis	75

CHAPTER	Page
5.4.2 Mechanical properties	84
5.4.3 Effective filler-based micromechanical models	90
5.5 Summary	94
VI IMPACT TOUGHENING MECHANISMS OF CALCIUM CARBONATE-REINFORCED POLYPROPYLENE NANOCOMPOSITE.....	95
6.1 Introduction	95
6.2 Experimental	96
6.2.1 Materials.....	96
6.2.2 Sample preparation.....	97
6.2.3 Microscopy and toughening mechanism investigation	98
6.3 Results and Discussion.....	99
6.3.1 Study of fracture process based on the DN-4PB Charpy impact specimens	100
6.3.2 Study of fracture process based on the Izod impact specimens	108
6.4 Summary	113
VII CONCLUSIONS AND RECOMMENDATIONS.....	114
7.1 Morphological Characterizations of the Nylon-6 Nanocomposites	114
7.2 Effect of Clay Aspect Ratio and Orientation on Mechanical Behaviors of the Nylon-6 Nanocomposites	115
7.3 Impact Toughening Mechanisms in the PP/CaCO ₃ Nanocomposite.....	116
7.4 Recommendations for Future Work	117
7.4.1 Effect of nanofiller orientation and aspect ratio on property enhancement.....	117
7.4.2 Effect of dispersion of layer-structured nanofiller on reinforcement efficiency	118
7.4.3 Fabrication of desirable properties in terms of modulus and toughness in nanocomposites	119
REFERENCES	121
APPENDIX	128
VITA	162

LIST OF TABLES

TABLE	Page
3.1 Thermal analysis for the nylon-6 and nylon-6/clay nanocomposites	33
3.2 Density analysis results for the nylon-6 and nylon-6/clay nanocomposites	33
4.1 Characteristic parameters of the neat nylon-6 and nylon-6/clay nanocomposites	51
5.1 The results of TEM image analysis for the reference, A1, and C2 nanocomposites	84
5.2 Tensile properties of the neat nylon-6 and nylon-6/clay nanocomposites	86
5.3 Mechanical properties and heat distortion temperature of the neat nylon-6 and nylon-6/clay nanocomposites	87
6.1 Chemical composition (wt%) of the CaCO ₃ nanoparticles	97
6.2 Impact strengths of the PP and PP/CaCO ₃ nanocomposites	109

LIST OF FIGURES

FIGURE	Page
2.1 Schematic structure of single sodium montmorillonite [39].....	8
2.2 Typical WAXD patterns for the three different nanocomposites	10
2.3 Schematic of the <i>in-situ</i> polymerization process	12
2.4 Three principle orthogonal directions used to calculate nanocomposite modulus corresponding: (a) Halpin-Tsai and (b) Mori-Tanaka models	14
2.5 Schematic of DN-4PB specimen, and the regions for OM and TEM observation	23
3.1 The ECAE die used: (a) Schematic of the ECAE die and (b) the ECAE processing setup	27
3.2 Schematic showing the thin section cut for TEM observation	30
3.3 Annealing test results for the A1-ECAE processed nylon-6/clay nanocomposite: (a) before annealing and (b) after annealing	31
3.4 Typical TEM micrographs of the simple-shear-processed and annealed nylon-6/clay nanocomposites (NC): (a) NC_Reference, (b) NC_A1 and (c) NC_C2. The arrows indicate the flow direction	35
4.1 Schematic of the specimens used for TEM and X-ray observations, and the clay orientation with respect to the ECAE processing and annealing. ND = normal direction, TD = transverse direction and FD = flow direction	42
4.2 Typical TEM micrographs of the simple-shear-processed and non-annealed nylon-6/clay nanocomposites (NC) used for image analysis: (a) NC_Reference, (b) NC_A1 and (c) NC_C2. The arrows indicate the flow direction	44
4.3 Typical TEM micrographs of the simple-shear-processed and annealed nylon-6/clay nanocomposites (NC) used for image analysis: (a) NC_Reference, (b) NC_A1 and (c) NC_C2. The arrows indicate the flow direction	46

FIGURE	Page
4.4 Cross-polarized OM micrographs of the nylon-6 and nylon-6/clay nanocomposites: (a) simple-shear-processed and non-annealed A1 nanocomposite, (b) simple-shear-processed and annealed A1 nanocomposite, (c) non-simple shear processed and annealed reference nanocomposite and (d) non-simple shear processed and annealed neat nylon	48
4.5 The intensity (I) vs. azimuthal angle (χ) plots and the as-collected 2-D SAXS profiles for the nylon-6 and the nanocomposites: (a) annealed NC_Reference, (b) annealed nylon-6, (c) non-annealed NC_A1, (d) annealed NC_A1, (e) non-annealed NC_C2 and (f) annealed NC_C2	55
4.6 Schematic of the lamellar orientation with respect to the ECAE processing and annealing: (a) annealed NC_Reference, (b) annealed NC_A1 and (c) annealed NC_C2	58
4.7 Lorentz plot of the annealed A1 nylon-6/clay nanocomposite	60
4.8 TEM micrograph showing the lamellar orientation of the reference nanocomposite. The arrows indicate the flow direction	61
4.9 WAXS profiles of the annealed nylon-6 and the nanocomposites	62
4.10 DSC fusion endotherms of the annealed nylon-6 and the nanocomposites	63
4.11 Schematic of hierarchical structure and morphological parameters of the exfoliated reference nylon-6/clay nanocomposite	64
5.1 Schematic of route A and route C ECAE processes	72
5.2 Schematic of the specimens used for tensile, K_{IC} testing, and TEM observation, and the clay orientation with respect to the ECAE processing and annealing: ND = normal direction, TD = transverse direction and FD = flow direction	73
5.3 Typical TEM micrographs of the simple-shear-processed and non-annealed nylon-6/clay nanocomposites (NC) used for image analysis: (a) NC_Reference, (b) NC_A1 and (c) NC_C2. The arrows indicate the flow direction	76

FIGURE	Page
5.3 Typical TEM micrographs of the simple-shear-processed and non-annealed nylon-6/clay nanocomposites (NC) used for image analysis: (a) NC_Reference, (b) NC_A1 and (c) NC_C2. The arrows indicate the flow direction	76
5.4 Typical TEM micrographs of the simple-shear-processed and annealed nylon-6/clay nanocomposites (NC) used for image analysis: (a) NC_Reference, (b) NC_A1 and (c) NC_C2. The arrows indicate the flow direction	78
5.5 Schematic of the lamellar orientation with respect to the ECAE processes and annealing: (a) annealed NC_Reference, (b) annealed NC_A1 and (c) annealed NC_C2	80
5.6 TEM micrograph showing the fractured and shortened clays <i>via</i> an ECAE simple shear process. The arrows indicate the fractured clays	82
5.7 Quantitative TEM image analyses of the annealed nanocomposites: (a) clay length and (b) clay orientation (SD: standard deviation)	83
5.8 Typical engineering stress-strain curves for the annealed neat nylon-6 and nanocomposites	85
5.9 Effect of clay aspect ratio and clay orientation on tensile properties for the ECAE simple-shear-processed and annealed nanocomposites	86
5.10 Dynamic mechanical spectra for the annealed neat nylon-6 and nanocomposites: (a) storage modulus and loss tangent and (b) the HDT estimated from the plot of $\log G'$ vs. temperature	89
5.11 Effective filler-based model predictions of the Halpin-Tsai (H-T) and the Mori-Tanaka (M-T) theories: (a) clay aspect ratio (α) and (b) clay orientation (S) on the modulus improvement of exfoliated nanocomposites. Experimental data (E_{nc}) included	93
6.1 Schematic of the impact specimens used for OM and TEM observation: (a) notched Izod impact specimen and (b) DN-4PB Charpy impact specimen	99
6.2 TOM under cross-polarized field: (a) neat PP and (b) PP/CaCO ₃ nanocomposite	101

FIGURE	Page
6.3 TOM of DN-4PB Charpy impact damage zone of PP/CaCO ₃ nanocomposite: (a) bright field and (b) cross-polarized field. The crack propagates from left to right	103
6.4 TEM of DN-4PB Charpy impact-tested PP/CaCO ₃ specimen taken from: (a) 120 μm above the crack surface, (b) 60 μm above the crack surface, (c) immediately above the crack surface and (d) undamaged region. The arrow indicates the crack propagation direction	105
6.5 Schematic of the deformation mechanism in the DN-4PB Charpy impact-tested PP/CaCO ₃ specimen. The regions of the TEM taken in Fig. 6.4 are marked	108
6.6 TOM of neat PP: (a) bright field and (b) cross-polarized field. The arrow indicates the crack propagation direction	110
6.7 TOM of PP/CaCO ₃ nanocomposite: (a) bright field and (b) cross-polarized field. The arrow indicates the crack propagation direction.....	111

CHAPTER I

INTRODUCTION

Polymer nanocomposites have been one of novel materials, which have attracted great interests in academia and industry due to exceptional reinforcement at extremely low nanofiller loading [1-10]. A variety of inorganic nanofillers, such as clay layers, calcium carbonate, zirconium phosphate and carbon nanotube, have been successfully used as second phases to improve the physical and mechanical properties. In addition, a nanoscopic filler technology capable of good dispersion into a polymer matrix has drawn considerable scientific and technological attention over the last decade. The efficiency of property enhancement strongly depends on the nanofiller structural parameters, e.g., filler shape, modulus, aspect ratio, orientation, volume fraction and interfacial adhesion [11-15].

There are three types of nanofillers which are categorized by whether they have one-, two-, or three-dimensions in the nanometer range. One-dimensional nanofillers usually consist of the form of sheets with 1-3 nm in thickness and the other dimensions being two or more orders of magnitude larger. A variety of natural and synthetic inorganic fillers can be surface-treated to achieve intercalation and exfoliation [16].

Dissertation style and format follow that of *Polymer*.

Montmorillonite has been the most widely studied, because of its availability, ease of surface modification and relatively high cation exchange capacity (CEC) for property enhancement [16-18]. Two-dimensional nanofillers have two dimensions in the nanometer range, such as carbon nanotubes and cellulose whiskers. Such a nanocomposite has been extensively studied as multifunctional material that yields exceptional properties [19,20]. Three-dimensional nanofillers include isodimensional nanoparticles such as spherical calcium carbonate, and silica nanoparticles obtained *via in-situ* sol-gel methods. Semiconductor nanoclusters are included in this category [21]

1.1 Polymer-Clay Nanocomposites

Layered silicates consist of extremely thin (~1 nm), plate-like structures that have large surface areas and high aspect ratios. Polymer-layered silicate nanocomposites have been attractive potential for a more customized engineering application due to their exceptional properties even at very low clay content. These properties include enhanced modulus and strength [1-6], high heat distortion temperature [1,2], improved gas barrier property [22-25], good flame retardancy [26,27] and improved solvent and UV resistance [28,29]. All these improvements can be obtained by producing a nanoscopic system in which high-aspect-ratio clay particles are well exfoliated in a polymer matrix.

1.2 Polymer-CaCO₃ Nanocomposites

Calcium carbonate (CaCO₃) particles have a nearly isotropic particulate structure [30]. Typically, polymer-inorganic filler composites have shown an increase in modulus

but a decrease in toughness and ductility, because of the strong reinforcement effect of rigid filler phase. However, a few exceptions have also been reported in the literature. In toughening polyethylene (PE), CaCO_3 and chalk particles have been shown to be able to improve toughness of PE effectively [31-33]. For polypropylene (PP), Thio and Argon [34] found that the CaCO_3 -toughened PP composites could exhibit greatly improved impact strengths up to 40–50 kJ/m^2 , as compared to 2–8 kJ/m^2 for that of neat PP. More recently, Chan *et al.* [30] showed that the fracture toughness of PP could be enhanced by over 300% by incorporating nanometer-sized (ca. 40 nm) CaCO_3 particles. Therefore, the polymer- CaCO_3 nanocomposites can offer an attractive way for improvement in both Young's modulus and fracture toughness.

1.3 Research Objectives and Significance

The primary objective of this research is to fundamentally understand the roles of nanofiller structural parameters on mechanical behaviors of thermoplastic nanocomposites, with an emphasis on the effects of aspect ratio, orientation and shape of nanofiller for the property enhancement of semicrystalline nanocomposites. The significance of this dissertation is summarized as follows:

- Evaluate the effectiveness of a large-scale simple shear process on alternation of nanofiller aspect ratio and orientation.
- Investigate the morphological developments of both nanofiller and polymer crystalline in semicrystalline nanocomposites during a large-scale simple shear process.

- Correlate the morphological characterizations with the physical and mechanical properties in semicrystalline nanocomposites with variations in aspect ratio, orientation and shape of nanofiller.
- Understand the toughening mechanisms responsible for the impressive toughening effect in a semicrystalline nanocomposite.

1.4 Dissertation Outline

First, background knowledge essential related to this research and general overview of relevant literature are provided (Chapter II).

With the effectiveness of a large-scale simple shear process for altering nanofiller structural parameters (Chapter III), the first particular attention is given to the morphological characterizations of semicrystalline nanocomposites (Chapter IV). The morphological characterizations of both nanofiller and polymer crystalline will be studied at various length scales:

- The micrometer level information is characterized by optical microscopy (OM): the spherulite size of semicrystalline polymer.
- The nanometer level information is extracted from transmission electron microscopy (TEM) and small-angle X-ray scattering (SAXS): nanofiller aspect ratio, nano-filler orientation, correlation length between interlayers, lamellar orientation and long period.

- The crystallographic level information is revealed by wide-angle X-ray diffraction (WAXD) and differential scanning calorimetry (DSC): the formation of crystal phases, e.g., α -, γ - form nylon-6, and α -, β - form PP.

The second part of this dissertation is focused on the property evaluation in the exfoliated semicrystalline nanocomposites with variations in nano filler orientation and aspect ratio (Chapter V). Several physical and mechanical tests will be used. The micromechanics-based models will be implemented to account for the effect of the nanofiller structural parameters on the property enhancement of the nanocomposites.

The third attention will be placed on studying the underlying fracture and toughening mechanisms in the calcium carbonate (CaCO_3) nanoparticle-filled PP nanocomposite (Chapter VI). Double-notch four-point bending (DN-4PB) technique will be employed to gain the detailed fracture mechanism(s) observed in the PP/ CaCO_3 nanocomposite.

Finally, the overall concluding remarks of this dissertation and recommendations for future work are given (Chapter VII).

In appendix, due to the micron-sized particle of talc, mechanical properties of talc- and CaCO_3 -reinforced high-crystallinity polypropylene composites will be studied.

CHAPTER II

BACKGROUND AND LITERATURE REVIEW

2.1 Introduction

Polymeric materials have been reinforced by inorganic nanofillers, termed polymer nanocomposites, to improve physical and mechanical properties. Owing to their remarkable property enhancement, low cost and good processability, polymer nanocomposites are of particular interest.

The incorporation of second phase, novel nanofillers to a polymer matrix has been an attractive potential for a more customized engineering application. For instance, polyamide-6/clay nanocomposites have shown improvements in a variety of physical properties, such as modulus, strength, gas barrier properties, thermal stability, etc. Furthermore, such significant property enhancements are obtainable at very low nanoclay content. Shepherd *et al.* [35] proposed that single clay layers could be an ideal reinforcing nanofiller in 1974, due to their extremely high aspect ratio and the nanometer filler thickness. Clay layers have high cation exchange capacity (CEC), which allows surface modification of the clay interlayer to achieve better compatibility with a host polymer matrix. In addition to high CEC, clay is an abundant, inexpensive inorganic material. Those advantages have led to large-scale commercial uses. Moreover, an outstanding research by the Toyota group [36-38] has drawn forth efforts of many researchers on polymer-clay nanocomposites.

In this chapter, the morphological and structural characterizations of polymer nanocomposites will be reviewed. Continuum-based micromechanical models are presented in order to gain a better understanding with regard to the dependence of nanofiller structural parameters on the reinforcement effect of nanocomposites. The fundamentals related to toughness evaluation and toughening mechanisms for polymer nanocomposites will be reviewed.

2.2 Characterization of Polymer Nanocomposites

2.2.1 Structure of layered silicate

The most common nanofillers used in polymer-clay nanocomposite are sodium montmorillonites, which consist of the 2:1 layered system of silicate platelets. Two outer tetrahedral layers, containing Si and O atoms, are fused to an inner octahedral layer, containing Al and Mg atoms that are bonded to oxygen or hydroxyl groups, resulting in a sandwich type structure. Fig. 2.1 illustrates the schematic structure of sodium montmorillonite. The isomorphous substitution of divalent Mg (Mg^{2+}) for trivalent Al (Al^{3+}) causes to an electrostatic imbalance within the clay layers, resulting in an excess negative charge: the excess negative charge is counterbalanced by the adsorption of cations, e.g., Na^+ or Ca^{2+} . The thickness of single layer montmorillonite is ~1 nm and the lateral dimensions can range from a few hundred angstroms to several microns. Exceptional property enhancements can be achieved by well dispersing the individual silicate platelets in a polymer matrix. However, the smectite structure of native clay may be one of the obstacles for good dispersion. To make the clays more compatible with

polymers, the cations in the clay are typically exchanged with alkyl ammonium ions to form a swollen hybrid structure, termed organoclay.

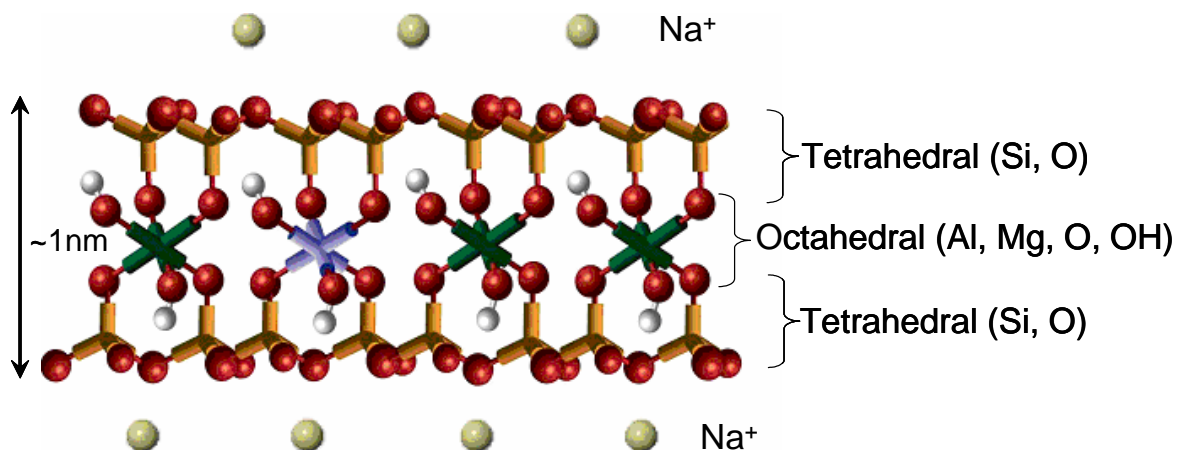


Fig. 2.1 Schematic structure of single sodium montmorillonite [39].

2.2.2 Dispersion of nanofillers in polymer matrix

Basically, polymer/clay nanocomposites can be classified as *immiscible*, *intercalated* or *exfoliated*:

(a) *Immiscible*: For these materials, polymer chains are unable to penetrate into the galleries of the organoclay layers, remaining originally stacked clay layers. The spacing of the layer structures is nearly identical to their pristine state. The morphology

and property characterization of immiscible composites, therefore, remain the same as conventional microcomposites.

(b) *Intercalated*: When several polymer chains diffuse into the galleries of the organoclay layers and then the clay layers expand, intercalated structures are formed. However, the interlayer d-spacing still remains a short range order ($d_{001} \sim 20\text{-}80 \text{ \AA}$).

(c) *Exfoliated*: The exfoliated structures are predominantly composed of individual, ~ 1 nm-thin layers dispersed in a polymer matrix, and are a result of extensive penetration of the polymer and delamination of the clay layers. The correlation length between the dispersed clay layers results in a long range ordering ($\geq 100 \text{ \AA}$), so that the interaction forces between the clay layers nearly diminish. Exfoliation has been the ultimate goal of most researchers in this area because this morphology is expected to lead to dramatic improvements in nanocomposite properties, with a much lower content of fillers than conventional composites.

Transmission electron microscopy (TEM) and wide angle X-ray diffraction (WAXD) are used to characterize those clay layer structures of nanocomposites. Fig. 2.2 illustrates the typical WAXD patterns for the three different nanocomposites.

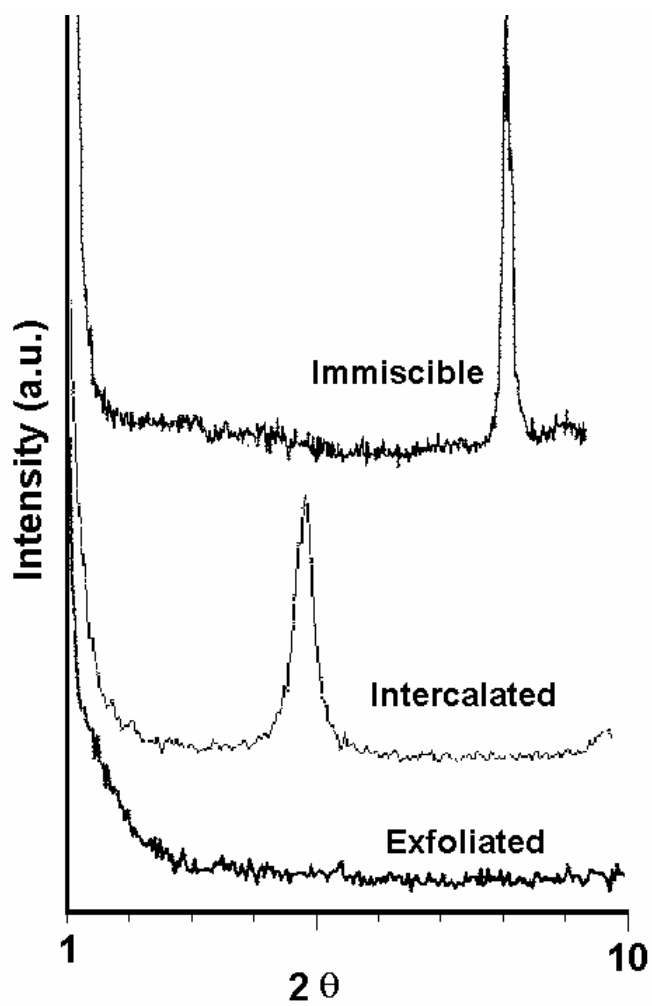


Fig. 2.2 Typical WAXD patterns for the three different nanocomposites.

2.2.3 *In-situ* polymerization of nylon-6/clay nanocomposite

Fujiwara *et al.* [40] reported in 1976 that the first polymer-clay nanocomposite was produced using an *in-situ* polymerization technique. However, early results yielded marginal property improvements. In the early 1980's, the Toyota group [36-38] successfully produced superior nanocomposites using a modified version of the *in-situ* polymerization technique. The detailed description and the overall process for preparing the resin and the nanocomposite are documented in [36,41]. Briefly, organically surface-modified montmorillonite was achieved by cation-exchange reaction with 12-aminolauric acid. The resulting ion-exchanged montmorillonite (termed as 12-montmorillonite) was mixed with ϵ -caprolactam. Ring-opening polymerization of the ϵ -caprolactam by help of a small amount of 6-aminocaproic acid was initiated by the carboxyl ends (-COOH) on the 12-montmorillonite, resulting in the chains (~32% of nylon-6 chains) with cationic ammonium ends (-NH₃⁺) tethered to the surface of negatively charged layer silicate (Fig. 2.3). The growth of those chains, which were driven by the free energy of polymerization, forces the clay layers apart until they are fully exfoliated.

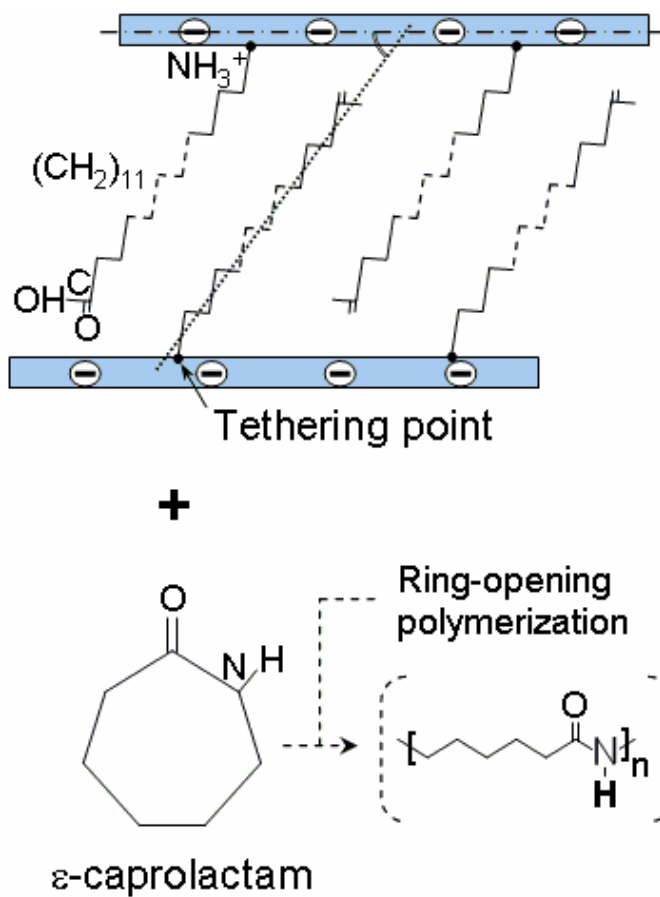


Fig. 2.3 Schematic of the *in-situ* polymerization process.

2.3 Continuum-based Micromechanical Models

Numbers of theoretical composite models have been developed for predicting the macroscopic mechanical properties of discontinuous second phase-filled composites in terms of the morphology of the composites [42-52]. Numerous assumptions inherent in

those micromechanical models are proposed. The detailed assumptions have been documented well in [53].

2.3.1 Conventional filler-based micromechanical models

In conventional micromechanical models, filler volume fraction (ϕ_f), filler aspect ratio (α), filler orientation (S) and filler modulus (E_f) or filler/matrix stiffness ratio (E_f/E_m) are the most important factors for predicting the macroscopic composite properties. Tucker *et al.* [54] reviewed the application of several micromechanical models to discontinuous fiber-reinforced composites. They reported that the Halpin-Tsai theory [48-50] provided reasonable prediction for composite modulus, and for composites with relatively large aspect ratio of fillers, the models based on Mori-Tanaka theory [45,47] showed the best prediction. The longitudinal engineering stiffness (E_{11}) and the transverse engineering stiffness (E_{33}) of the Halpin-Tsai and the Mori-Tanaka models are expressed in equations (2.1) and (2.2), respectively.

$$\frac{E_{11}}{E_m} = \frac{1 + 2(l/t_p)\eta\phi_f}{1 - \eta\phi_f} \quad (\text{Halpin-Tsai}) \quad (2.1a)$$

$$\frac{E_{33}}{E_m} = \frac{1 + 2\eta\phi_f}{1 - \eta\phi_f} \quad (2.1b)$$

$$\eta = \frac{E_f/E_m - 1}{E_f/E_m + 2(l/t_p)}$$

where l is the filler length and t_p is the filler thickness.

$$\frac{E_{11}}{E_m} = \frac{1}{1 + \phi_f [-2\nu_m A_3 + (1 - \nu_m)A_4 + (1 + \nu_m)A_5 A] / 2A} \quad (\text{Mori-Tanaka}) \quad (2.2a)$$

$$\frac{E_{33}}{E_m} = \frac{1}{1 + \phi_f (A_1 + 2\nu_m A_2) / A} \quad (2.2b)$$

where ϕ_f is the filler volume fraction, ν_m is the Poisson ratio of the matrix, A , A_1 , A_2 , A_3 , A_4 and A_5 are calculated from the matrix, filler properties and components of the Eshelby tensor [43], which depend on the filler aspect ratio (l/t_p) (where l and t_p are the major and minor diameters of an ellipsoidal disk-shaped inclusion) and dimensionless elastic constants of the matrix [45]. Fig. 2.4 shows the three principle orthogonal directions used to calculate composite stiffness corresponding (a) Halpin-Tsai and (b) Mori-Tanaka models.

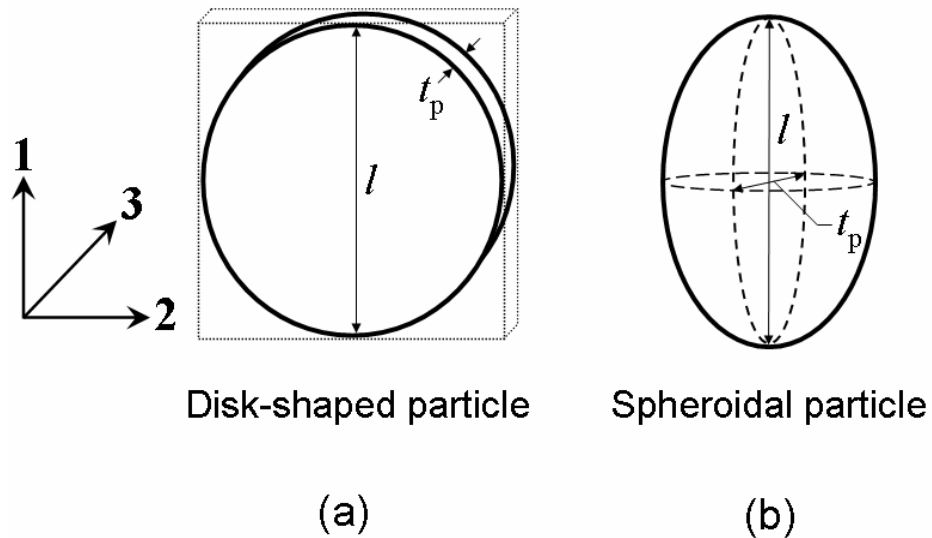


Fig. 2.4 Three principle orthogonal directions used to calculate nanocomposite modulus corresponding: (a) Halpin-Tsai and (b) Mori-Tanaka models.

2.3.2 Effective filler-based micromechanical models

The dispersion of fillers in a polymer matrix is typically described in terms of exfoliation or intercalation. The fully exfoliated nanocomposites are considered to consist of single clay layers dispersed in a polymer matrix, while in the intercalated systems, inter-layer domains of fillers (e.g., clay particles) are penetrated by polymer chains and consequently stacked typically with an inter-layer spacing of 1-4 nm. However, conventional filler-based micromechanical models for predicting the macroscopic properties of nanocomposites were not considered those clay structural parameters, which regards that nanocomposites just consist of two homogeneous phases, fillers and matrix. In an earlier work by Sheng and Boyce [55], in order to explain the geometric natures of intercalated clay they proposed the effective particles, which consist of the clay layers and clay inter-layer galleries. Therefore, effective filler structural parameters, the number of silicate layers per stacked clay (n) and the silicate inter-layer spacing (d_{001}), are used to assess macroscopic property enhancement of intercalated particle-filled nanocomposites. Mechanics-based models for intercalated clay structure are established by mapping of the effective filler structural parameters (n , d_{001}) to the conventional filler structural parameters (α , ϕ_f , E_f/E_m).

The thickness of effective filler can be expressed in terms of n and d_{001} by the following equation [53]:

$$t_{\text{eff}} = (n-1)d_{001} + t_p \quad (2.3)$$

where t_p is the thickness of a silicate platelet.

The number of platelets per effective filler thickness (κ) [55]:

$$\kappa = \frac{n}{t_{\text{eff}}} = \frac{n}{(n-1)d_{001} + t_p} \quad (2.4)$$

$$\frac{V_{\text{platelet}}}{V_f} = \frac{nt_p}{(n-1)d_{001} + t_p} = \kappa t_p \quad (2.5)$$

where V_{platelet} and V_f are the volumes of platelet in a stack and filler, respectively.

Effective filler aspect ratio (α_{eff}) of can be written as:

$$\alpha_{\text{eff}} = \frac{l}{t_{\text{eff}}} = \frac{l}{(n-1)d_{001} + t_p} \quad (2.6)$$

The filler weight fraction (ψ_f) can be converted to filler volume fraction (ϕ_f) using the following equation:

$$\phi_f = \frac{\psi_f / \rho_f}{\psi_f / \rho_f + (1 - \psi_f) / \rho_m} \quad (2.7)$$

where ρ_f and ρ_m are the densities of filler and matrix, respectively.

For an intercalated nanocomposite, the effective filler weight fraction (ψ_{eff}) is not equal to the filler weight fraction (ψ_f).

$$\frac{\psi_f}{\psi_{\text{eff}}} = \frac{\rho_f V_f}{\rho_{\text{platelet}} V_{\text{platelet}}} = \frac{\rho_f}{\rho_{\text{platelet}} \kappa} \equiv \delta \quad (2.8)$$

where ρ_{platelet} is the density of platelet.

Substituting $\psi_f = \delta \psi_{\text{eff}}$ into equation (2.7),

$$\phi_f = \frac{\psi_{\text{eff}} / \rho_f}{\psi_{\text{eff}} / \rho_f + (1/\delta - \psi_{\text{eff}}) / \rho_m} \quad (2.9)$$

If ψ_{eff} is small,

$$\phi_f \approx \left(\frac{\delta \rho_m}{\rho_f} \right) \Psi_{\text{eff}} = \left(\frac{\rho_m}{\rho_f} \cdot \frac{\rho_f}{\rho_{\text{platelet}} \kappa} \right) \Psi_{\text{eff}} = \left(\frac{\rho_m}{\rho_{\text{platelet}} \kappa} \right) \Psi_{\text{eff}} \quad (2.10)$$

where ρ_{platelet} and ρ_m is 2.83 and 1.14 (g/cm³) [53], respectively.

$$\phi_f = \frac{0.4 \Psi_{\text{eff}}}{\kappa} \quad (2.11)$$

If $E_{\text{gallery}} \ll E_{\text{platelet}}$,

$$\frac{E_f}{E_m} = \frac{\kappa t_p E_{\text{platelet}}}{E_m} \quad (2.12)$$

2.3.3 Shear lag model

In particular, rigid particles are naturally resistant to relatively high stress or strain. When such particle-filled composites are subject to axial load, a significant portion of the load is transmitted from the surrounding matrix to the rigid particles through shear stress at the interface.

Shear lag model [51] is employed to address the load-transfer efficiency on α , E_f/E_m .

$$\sigma_f = E_f \varepsilon \left[1 - \frac{\cosh\left(\frac{2x\lambda\alpha}{l}\right)}{\cosh(\lambda\alpha)} \right] \quad (2.13)$$

$$\tau_i = \frac{\lambda E_f \varepsilon}{2} \left[\frac{\sinh\left(\frac{2x\lambda\alpha}{l}\right)}{\cosh(\lambda\alpha)} \right] \quad (2.14)$$

$$\lambda = \left[\frac{4G_m}{E_f \ln(\phi_f)} \right]^{1/2}$$

where ε is the applied strain, x is the distance from the center of filler, τ_i is the interfacial shear stress along the filler length, and G_m is the shear modulus of the matrix. The shear lag model appears that large aspect ratio (α) and high E_f dominantly enable fillers to bear a large portion of the applied load.

2.4 Fracture Behaviors of Polymer Nanocomposites

2.4.1 Toughness evaluation

Linear elastic fracture mechanics (LEFM) can be used to describe the fracture behavior of brittle polymer nanocomposites (e.g., nylon-6/clay nanocomposite) below their glass transition temperature. The test specimens of these brittle polymer nanocomposites can easily satisfy the plane strain requirement in specimen geometry. To obtain plane strain conditions, ASTM D 5045 requires the following size criteria:

$$B, a, (W-a) > 2.5(K_Q/\sigma_y) \quad (2.15)$$

where B is the specimen thickness, a is the initial crack length, W is the specimen width, K_Q is the conditional K_{IC} and σ_y is the yield stress of the material tested. Those criteria effectively guarantee that the thickness will be at least an order of magnitude greater in

size than the plastic zone where small scale yielding occurs. However, the basic requirements and assumptions of LEFM are not satisfied in the case of a ductile polymer nanocomposite (e.g., PP/CaCO₃ nanocomposite) at room temperature. The reason is that a large plastic zone is developed at the crack tip, and this requires extra energy needed for crack propagation.

Another approach for the fracture behavior of ductile polymer nanocomposites is using the elastic plastic fracture mechanics (EPFM) by means of the J -integral, originally proposed by Rice [56,57].

It is well known that the J -integral is a path-independent energy line integral, an energy-based parameter used to characterize the stress-strain field around a crack tip surrounded by a plastic zone. The J -integral is given by:

$$J = \oint_{\Gamma} \left(w dy - T_i \frac{\partial u_i}{\partial x} ds \right) \quad (2.16)$$

where w is the strain energy density, T_i are components of the traction vector, u_i are the displacement vector, and ds is a length increment along the contour Γ . The strain energy density is defined as:

$$w = \int_0^{\varepsilon_{ij}} \sigma_{ij} d\varepsilon_{ij} \quad (2.17)$$

where σ_{ij} and ε_{ij} are the stress and strain tensors, respectively.

Equation (2.16) can be simplified to the J -integral value was calculated using the following equation:

$$J = \frac{\eta A}{B_N b_0} \quad (2.18)$$

where η is a dimensionless constant, A is the area under the load-load line displacement curve, B_N is the net thickness of the specimen (for no side grooved specimen $B_N = B$), b_0 is the initial ligament length. In order to obtain a J - R curve, the calculated J -values are plotted against the crack extension, Δa . The J_{IC} values are determined at the point of intersection between the J - R curve and the blunting line, $J = 2\sigma_y \Delta a$.

ASTM D 813 also requires the following size criteria to obtain plane strain conditions:

$$B, b_0 > 25(J_{IC}/\sigma_y) \quad (2.19)$$

2.4.2 Toughening mechanism observation

It is imperative to understand the fundamental parameters that govern the fracture behavior of polymer nanocomposites. To achieve these goals, unambiguous and effective methods have to be utilized to account for the crack evolution process in these nanocomposites.

Optical microscopy (OM), scanning microscopy (SEM) and transmission electron microscopy (TEM) techniques have been widely used to observe the fracture mechanism of the deformed specimen [58-64].

SEM observation

SEM is the most common technique to characterize the nature of the fracture surface. However, there is a disadvantage that the information gained from SEM works

is limited to the fracture surface, which usually leads to an incomplete understanding or misleading information concerning the exact fracture mechanism. On the other hand, if the sub-damaged surface can be carefully prepared using an etching technique, crazing and shear banding can still be observed using SEM in some polymer materials [65,66].

TOM observation

It has been shown that transmitted optical microscopy (TOM) can be used to detect deformation zone size, shear banding [63,64] and dilatational deformation such as crazing, cavitation and debonding [67]. However, the details of the damage processes cannot be determined by TOM due to its low resolution. Therefore, TEM is the most frequently used tool to probe the cavitation, crazing and debonding.

TEM observation

Rubber cavitation and matrix crazing of toughened polymers can be observed TEM [67]. Weon and co-workers [68] examined the toughening mechanism of the nanoscale calcium carbonate (CaCO_3)-filled PP nanocomposite using TEM. They clearly observed massive crazes in the matrix and shear deformation near the crack surface. This indicates that TEM is a very effective technique that can be used to reveal cavitation processes around the CaCO_3 particles.

The DN-4PB technique is one of the most effective ways of generating a subcritical crack tip damage zone [58-60]. The key toughening mechanism(s) and the

sequence of toughening events can be unambiguously identified in the arrested crack tip damage zone region in polymer nanocomposites using a variety of microscopy techniques. The schematic of DN-4PB specimen is shown in Fig. 2.5(a). Two edge-cracks of nearly equal length are generated on the same edge of a rectangular specimen. This specimen is loaded in a four-point bending geometry. The portion of the specimen between the two inner loading points is subjected to a constant bending moment. Thus the two cracks experience nearly identical stresses. When the load is applied, a plastic zone forms in front of the crack tips. Because the two cracks cannot be exactly identical, one crack will reach the critical state first and propagate unstably, thus leaving the remaining crack to develop a subcritical crack tip damage zone. The surviving crack can be used to probe the toughening mechanisms which occur at the crack tip and crack wake by means of thin-sectioning and various microscopy techniques (Fig. 2.5(b)).

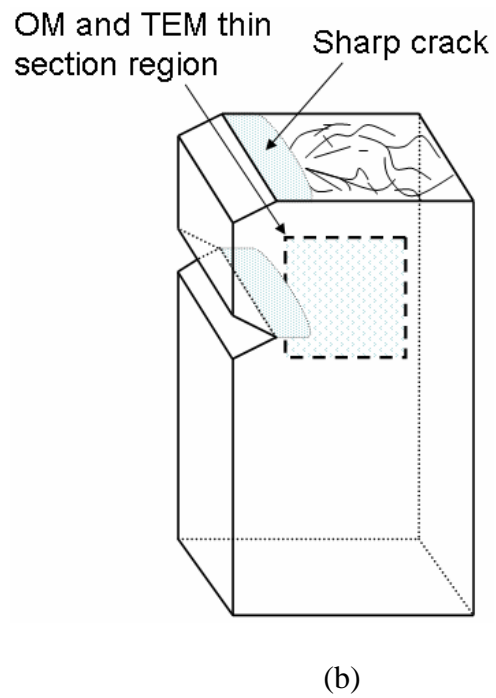
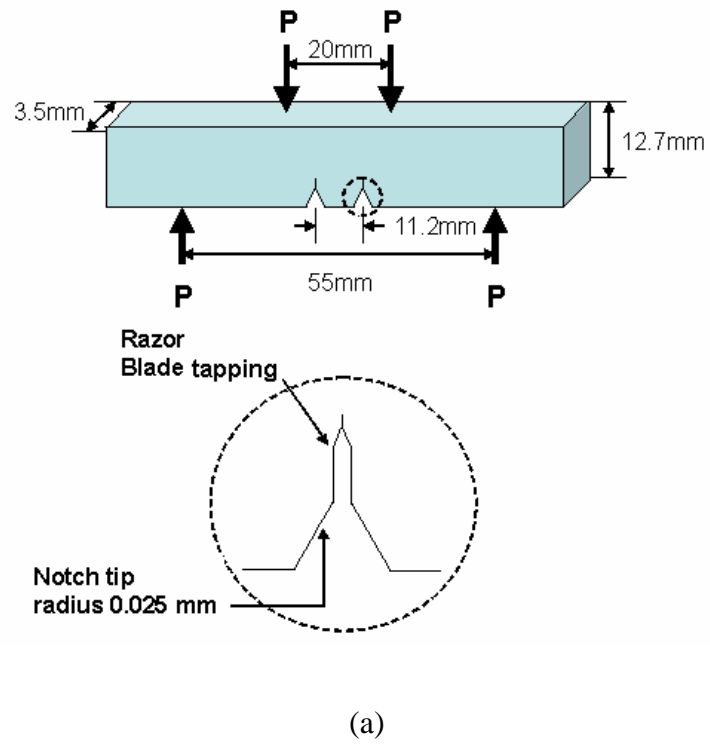


Fig. 2.5 Schematic of DN-4PB specimen, and the regions for OM and TEM observation.

CHAPTER III

EFFECTIVENESS OF A SIMPLE SHEAR PROCESS ON ALTERATION OF NANOFILLER STRUCTURES IN POLYMER NANOCOMPOSITES

3.1 Introduction

Equal channel angular extrusion (ECAE), a large-scale simple shear process, is a novel technique for fabricating bulk polymer with controlled levels of extreme plastic deformation [69-76]. The ECAE simple shear process alters the polymer microstructure and can improve properties [70]. Controlled anisotropy in polymers enhances physical and mechanical properties significantly [73]. ECAE applies a uniform simple-shear deformation through the thickness of a billet without changing the dimensions of the billet. Since the billet shape is constant, multiple extrusion passes can be applied.

It is nontrivial to alter the nanofiller structural parameters, e.g., filler aspect ratio and orientation, in a polymer matrix, and experimental efforts in this regard can rarely be found. Therefore, there is a need to experimentally generate variations in nanofiller aspect ratio and orientation. Some prior research efforts show that the ECAE simple shear process can tailor micron- and nanometer-scale polymeric structures through different extrusion routes. It was found that a large-scale simple shear process could control the fiber orientation of glass fiber/polyacetal composites, depending on the

process route [69]. In a previous work by Xia [70], it was speculated that controlled nanofiller orientation could be easily achieved through a simple shear process.

The main purpose of the current study is to examine the effectiveness of the ECAE process on the alternation of nanofiller structural parameters of polymer nanocomposites. The potential application of a simple shear process for tailoring the nanofiller geometry is discussed.

3.2 Experimental

3.2.1 Materials

Pellets of nylon-6/montmorillonite clay (2 wt%) nanocomposite, which prepared by *in-situ* polymerization of ϵ -caprolactam in the presence of ion-exchanged montmorillonite, were provided by Ube Industries Ltd., Japan.

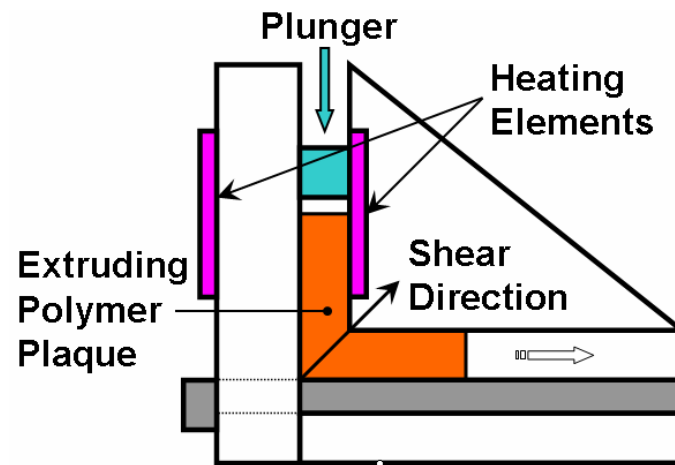
3.2.2 Sample preparation

Pellets of the nylon-6 and nylon-6/clay nanocomposite were dried at 100 °C for 12 h and were then slowly injection molded into plaques (152.4 mm × 76.2 mm × 9.5 mm) using a custom-built extrusion-injection molding machine powered by a HaakeBuchler Rheocord (system 40) machine with a screw revolving at 30 rpm. The temperature profiles of the extruder barrel were set at 235-245-255-260°C progressively toward the inlet of the injection mold, with the mold temperature set at 180 °C. After

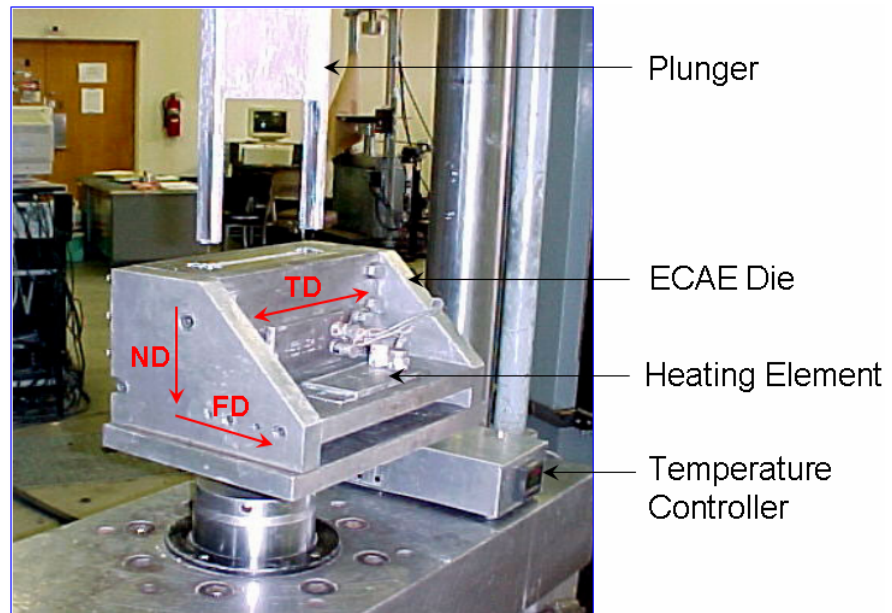
molding, the samples were immediately sealed in a polyethylene bag and kept in a vacuum desiccator prior to use to avoid moisture absorption.

3.2.3 ECAE process

An integrated die system for processing plaques was built. The die design and the process of ECAE appear schematically in Fig. 3.1(a). The ECAE die is a block with two intersecting channels of identical cross-sections. A servo-hydraulic mechanical testing system (MTS-810) pressed the specimens through a die, which was attached to the hydraulic ram of the test machine. An anti-seize lubricant (Permantex Industrial Type 80208) covered the internal die surfaces: it reduced friction between the polymer and the die. The testing system had a 490 kN load cell. A large-scale simple shear process was performed to alter the structural parameters of clay nanoparticles. This ECAE process was carried out at 60°C with an extrusion rate of 0.25mm/s. The samples before and after ECAE were categorized as follow: (1) Reference, (2) A1-received a single ECAE pass, and (3) C2-received two ECAE passes with a 180° rotation of the specimen between passes. The three orthogonal directions used to define the orientation of the specimen with respect to the processed plaque are the flow direction (FD), the transverse direction (TD), and the normal direction (ND) as shown in Fig. 3.1(b). A detailed description of the ECAE simple shear process can be found in [71-76].



(a)



(b)

Fig. 3.1 The ECAE die used: (a) Schematic of the ECAE die and (b) the ECAE processing setup.

3.2.4 Sample annealing

Annealing of the extrudate can relax the residual stresses, volumetric strains and thermal gradients to an acceptably low level by exposing the extrudate to an appropriate annealing temperature for a proper time. Conventional annealing has been done at or above the region of rapid crystallization temperature which is approximately halfway between the onset of glass transition (T_g) and the crystalline melting point (T_m) [77]. All samples were annealed at 150 °C for 3h to relax molecular orientation and pre-existing morphology in the matrix due to processing loads [78-81]. Furthermore, the heating chamber was purged with nitrogen gas to minimize sample oxidation during annealing. Subsequently, the annealing test was carried out at the same conditions to confirm the effect of annealing using samples of 10 mm × 10 mm × 2 mm. Afterward, the dimensional changes of the samples were recorded. The annealing temperature was controlled in ± 1 °C.

3.2.5 Differential scanning calorimetry (DSC) measurement

Non-isothermal crystallization behavior of the nylon-6 and nylon-6/clay nanocomposites was investigated using a Perkin-Elmer Pyris-1. All samples were sealed in aluminum pans and were protected in a nitrogen atmosphere during testing. The samples were first heated from 25 °C to 300 °C at a heating rate of 10 °C/min, subsequently held for 1 minute at 300 °C, and then cooled back to 25 °C at a rate of 10 °C/min. Additional scans were performed while re-heating the sample to 300 °C at the

same rate to assess the effect of the previous cooling scan. Samples of ~10 mg in weight were excised from the core regions for DSC measurements. The heat of fusion (Δh) was determined from the heating scan while the crystallization temperature (T_c) was analyzed from the cooling scan. The heat of fusion was determined by integrating the exothermic peak from 150°C to 250°C. the peak was then normalized by subtracting the amount of clay in the nanocomposites. The heat of fusion (Δh) values used in this study were based on the amount of pure nylon-6 of the nanocomposites.

3.2.6 Density measurement

Density measurements were performed using the displacement method to observe a change of density before and after simple shear process and annealing for the nylon-6 systems used in this study. As described in ASTM-D792-00, the density of samples can be determined by measuring sample weights in air and in solvent, respectively. Sample weights in air and in ethyl alcohol (C_2H_5OH) ($\rho = 0.789 \text{ g/cm}^3$) were measured. For the nanocomposite systems, the resulting density was based on the amount of pure nylon-6 of the nanocomposites.

3.2.7 Microscopy observation

Transmission electron microscopy (TEM) observations were conducted on a JEOL 1200EX transmission electron microscope operating at an accelerating voltage of 100 kV. Ultra-thin sections of ~90 nm in thickness were obtained under cryogenic

environment using a Reichert-Jung Ultracut E microtome with a diamond knife and placed on the 100-mesh Formvar/carbon-coated copper grids for TEM observation. Samples for TEM analysis were cut parallel to the flow direction (FD), as depicted in Fig. 3.2.

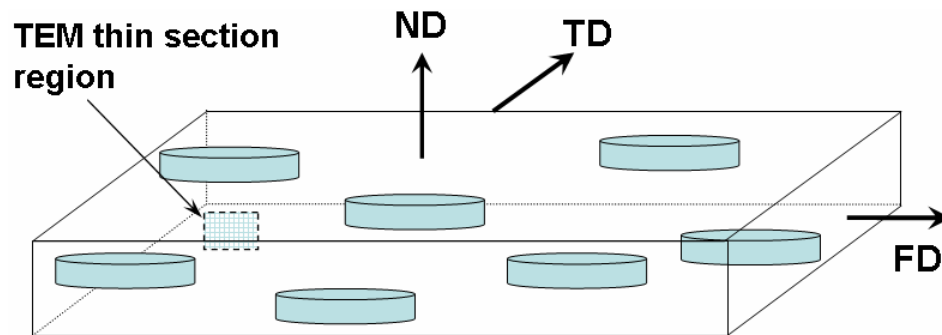


Fig. 3.2 Schematic showing the thin section cut for TEM observation.

3.3 Results and Discussion

3.3.1 Sample annealing observation

The annealing test results of simple-shear-processed nylon-6/clay nanocomposites show the extent of the shape recovery on annealing (Fig. 3.3). The left sample, which was cut parallel to the ND-FD plane from the A1 nanocomposite, appears to fully recover toward its original shape after annealing, while the right sample, which

is cut perpendicular to the FD, only shows the changes in height and width (Fig. 3.3(b)). This is consistent with the annealing effect of the right-sample. In order to ascertain that those geometry changes during annealing are due to simple shear process, a reference nanocomposite sample was also annealed under the same conditions. However, no appreciable changes in size and shape could be found.



(a)



(b)

Fig. 3.3 Annealing test results for the A1-ECAE processed nylon-6/clay nanocomposite: (a) before annealing and (b) after annealing.

3.3.2 DSC analysis and density measurement

DSC analyses shown in Table 3.1 indicate that the melting enthalpy (Δh) is inversely affected by the addition of clay. It should be noted that the simple-shear-processed but non-annealed, nanocomposites show that the melting enthalpy increases with simple shear process. This may be explained either by stress/strain-induced crystallization or by residual stress effect [70,75]. The incorporation of clay to nylon-6 matrix also causes a drop in density relative to the nylon-6 (Table 3.2), which is in qualitative agreement with the DSC observation. These findings are related to a decrease in crystallinity observed when clay is added to nylon-6. Lower crystallinity shown in the annealed nanocomposites is likely due to the constraint of chain mobility. The introduction of the well-dispersed clay to the nylon-6 matrix may cause the restriction of molecular mobility and space for crystal growth, which limits the formation of large crystallites. In addition, the presence of clay does not affect the crystallization temperature (T_c) of nylon-6. However, it is interesting to note that the melting enthalpy and the density of three different nylon-6 nanocomposites annealed are almost identical. These results indicate that the annealing is a very effective means to nullify any pre-existing shear-induced morphology in the nylon-6 matrix due to simple shear process. Thus, any effect and morphology induced by a simple shear process may be minimized or nullified through an annealing process.

Table 3.1

Thermal analysis for the nylon-6 and nylon-6/clay nanocomposites.

Sample	Melting enthalpy Δh (J/g)		Crystallization temperature T_c (°C)		Crystallinity χ_c (%)	
	Annealing					
	Before	After	Before	After	Before	After
NC_Ref	65.1	67.4	181	181	26.6	27.5
NC_A1	68.6	67.5	181	181	28.0	27.6
NC_C2	65.5	67.1	182	181	26.8	27.4
Nylon-6	74.9	80.2	182	182	31.2	33.5

χ_c is calculated by the ratio of Δh to Δh_0 .

Δh_0 (heat of fusion with 100% crystalline nylon-6) is 240 J/g [82].

Δh is calculated based on the amount of nylon-6 in the composites.

Table 3.2

Density analysis results for the nylon-6 and nylon-6/clay nanocomposites.

Sample	Density* (g/cm ³)		Crystallinity χ_c (%)	
	Annealing			
	Before	After	Before	After
NC_Ref	1.1165	1.1172	24.5	25.0
NC_A1	1.1135	1.1169	22.3	24.8
NC_C2	1.1133	1.1158	22.2	24.0
Nylon-6	1.1272	1.1303	32.3	34.5

* The average values were calculated after testing three specimens of each sample.

Density of the montmorillonite clay is 2.83 g/cm³ [83].

Densities of 100% amorphous and crystalline nylon-6 are 1.084 and 1.230 g/cm³, respectively [84].

Density and crystallinity is calculated based on the amount of nylon-6 in the nanocomposites.

3.3.3 Microscopy investigation

Fig. 3.4 shows the TEM micrographs that indicate different clay aspect ratio and orientation within the simple-shear-processed and annealed nanocomposites. The reference nylon-6/clay nanocomposite, which received no simple shear deformation, shows well-exfoliated clay structure along the flow direction (Fig. 3.4(a)). Also, it is observed that clay lengths and orientations of the A1 and C2 nylon-6/clay nanocomposites have been varied upon the simple shear process (Figs. 3.4(b) and (c)). Interestingly, careful observation indicates that the A1 process only reduces the clay aspect ratio, while the C2 route alters not only the clay aspect ratio but also the clay orientation.

For the controlled nanofiller size and orientation, ECAE simple shear process appears to be powerful. Altering nanofiller structural parameters within a polymer matrix offers an attractive way to produce desirable properties for engineering applications. A simple shear process with various processing scenarios may be encouraged to achieve those fabrications.

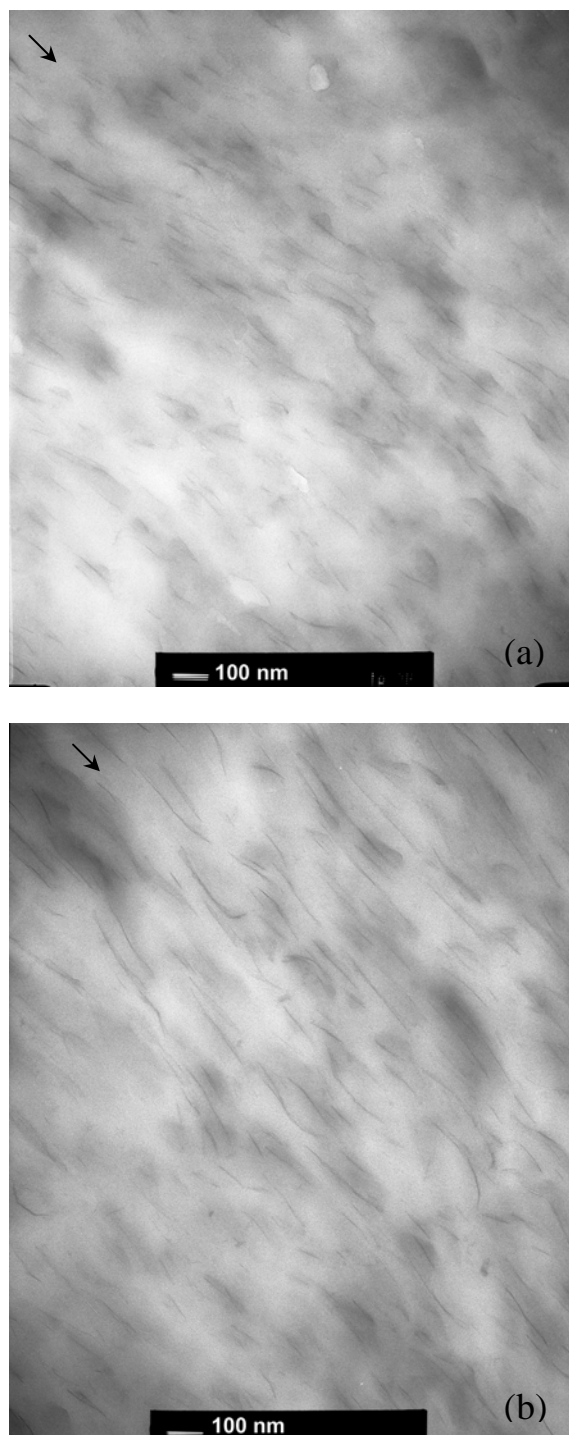


Fig. 3.4 Typical TEM micrographs of the simple-shear-processed and annealed nylon-6/clay nanocomposites (NC): (a) NC_Reference, (b) NC_A1 and (c) NC_C2. The arrows indicate the flow direction.

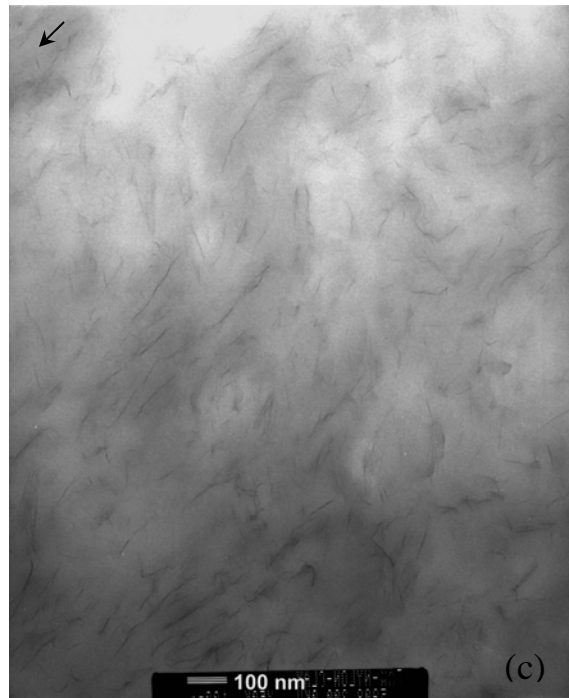


Fig. 3.4 Continued.

3.4 Summary

The effectiveness of ECAE process on the alternation of nanofiller structural parameters of the nylo-6/clay nanocomposite was investigated. Sample annealing appears to minimize pre-existing morphology due to processing. The annealing effect is verified using the annealing test, differential scanning calorimetry and density measurement. Consequently, a large-scale simple shear process is recommended to be one available method for tailoring the nanofiller structural parameters, e.g., nanoclay aspect ratio and orientation, within a polymer matrix.

CHAPTER IV

MORPHOLOGICAL CHARACTERIZATION OF NYLON-6 NANOCOMPOSITE FOLLOWING A LARGE-SCALE SIMPLE SHEAR PROCESS

4.1 Introduction

Polymer/layered silicate nanocomposites are attractive for a number of structural and functional applications due to their exceptional properties even at very low clay content. These properties include enhanced modulus and strength [1-6], high heat-distortion temperatures [1-2], improved gas barrier properties [22-25], and good flame retardancy [26-27]. All these improvements can be obtained by producing a nanoscopic system in which high-aspect-ratio clay particles are well exfoliated in the polymer matrix.

The physical and mechanical properties of the polymer nanocomposites strongly depend upon the clay aspect ratio, clay orientation, and interfacial adhesion [11-15]. Dispersed platelets may also affect the semi-crystalline polymer matrix morphological features, such as crystal structure, crystallinity, lamellae orientation, and spherulite formation. As a result, the clay layer structure can significantly affect the morphology and properties of nylon-6/clay nanocomposites [85].

It has been shown that, for semicrystalline polymer based nanocomposites, alignment of nano-size clay layers by injection-molding has an effect on the nanoscopic

orientation of crystalline lamellae. Earlier transmission electron microscopy (TEM) observations of injection-molded nylon-12/clay nanocomposite showed crystalline lamellae oriented perpendicularly to the surface of silicate layers [12]. X-ray diffraction studies by others have also revealed that the chain axes of nylon-6 crystallites are aligned parallel to the clay layers in the surface region of injection-molded articles, whereas the chain axes are oriented perpendicular to the surface of clay layers in the interior regions [86]. In addition, as pointed out by Kojima *et al.* [1] a large fraction of nylon-6 chains could also be tethered to the surface of clay layers through ionic bonding. From thermodynamic and kinetic standpoints, the polymer chain confinement introduced by the presence of nano-clays will impact both the final structure and the formation of the crystalline structures in semicrystalline polymers, thereby affecting the properties of the nanocomposite.

In this paper, particular attention is given to the influence of the orientation and aspect ratio of nano-clays on the morphological development in exfoliated nylon-6/clay nanocomposites. Optical microscopy (OM), TEM, differential scanning calorimetry (DSC), wide angle X-ray diffraction (WAXD), and small angle X-ray scattering (SAXS) are employed to provide detailed information on crystalline and clay layer structure in the exfoliated nanocomposites with variation in clay orientation and aspect ratio. Morphologies, at both micrometer and nanometer length scales, of a commercial grade nylon-6/clay nanocomposite before and after a large-scale simple shear process are characterized and described in detail.

4.2 Experimental

4.2.1 Materials

A commercial grade nylon-6 nanocomposite (grade number-1022C2) with 2 wt% layered silicate and neat nylon-6 (grade number-1022B) was provided by Ube Industries Ltd, Japan. For comparison purpose, a virgin nylon-6 has also been studied. Both the nylon-6/clay nanocomposite and neat nylon-6 pellets were dried under vacuum at 100 °C for 12 hrs. The materials were then injection molded into plaques (152.4 mm × 152.4 mm × 9.5 mm) by using a custom-built extrusion-injection molder powered by a HaakeBuchler Rheocord (system 40) machine operated at a screw speed of 30 rpm. The temperature profiles of the extruder barrel were set at 235-245-255-260°C (with the highest temperature at the inlet of the mold) and the mold temperature was set at 180 °C. The molded plaques were then sealed in a polyethylene bag and kept in a vacuum desiccator prior to use to avoid moisture absorption.

A large-scale simple shear process, termed equal channel angular extrusion (ECAE) [71], was performed to alter the aspect ratio and orientation of the clay nanoparticles. ECAE was carried out at 60°C and at an extrusion rate of 0.25mm/s using a servo-hydraulic mechanical test system (MTS-810). Samples before and after ECAE were categorized as follows: (1) reference-no ECAE pass, (2) A1-received a single ECAE pass, and (3) C2-received two ECAE passes with a 180° rotation of the specimen between passes. A detailed description of the ECAE simple shear process can be found in [69,70,71-76]. After the ECAE orientation, all samples were annealed at 150 °C for

3hrs to minimize any pre-existing residual stresses due to processing [77-81]. The annealing chamber was purged with nitrogen gas to minimize sample oxidation during annealing. After annealing, specimens were cut from the center of the plates and polished to the desired dimensions for structural characterization.

4.2.2 Morphology characterization

Cross-polarized OM, performed on an Olympus BX60 optical microscope, was used to observe the change of spherulite structure within the samples. For OM observation, samples were polished to thin sections with a thickness of $\sim 40 \mu\text{m}$.

TEM observations were conducted on a JEOL 1200 EX operated at an accelerating voltage of 100 kV. Ultra-thin sections ($\sim 90 \text{ nm}$ in thickness) were obtained under a cryogenic environment using a Reichert-Jung Ultracut E microtome with a diamond knife. The thin section was stained in a vial containing 0.4% aqueous osmium tetroxide (OsO_4) for 24 hrs [87]. Samples for TEM analysis were cut parallel to the ND-FD plane, as depicted in Fig. 4.1. The thin sections were then situated on the 100-mesh Formvar/carbon-coated copper grids for TEM observation.

4.2.3 X-ray characterization

WAXD experiments were performed at room temperature using a Bruker-AXS D8 powder diffractometer with a sealed X-ray source (Cu) in the standard vertical θ - 2θ geometry (40 kV and 50mA). A germanium incident beam monochromator was used to

produce $K\alpha_1$ free radiation, and a Si(Li) detector was utilized for data collection. The wavelength of the incident X-ray was 1.54\AA . Data were collected from 7° to 35° (2θ) at a scanning rate of $1^\circ/\text{min}$.

SAXS measurements were conducted at room temperature using a Bruker-Nano-star (40 kV and 35mA). SAXS samples were cut parallel to the flow direction (Fig. 4.1). The wavelength of the incident X-ray was 1.54\AA . The sample to detector distance was 6430 mm. Two-dimensional SAXS images, with a resolution of 1024 by 1024 pixels, were collected to directly display distributions of crystalline lamellar orientation (*via* the long period) in the plane of the sample. Samples with dimensions of $10\text{ mm} \times 10\text{ mm} \times 0.2\text{ mm}$ were cut parallel to the ND_FD plane using a diamond saw. All samples were marked to note the preferred long period orientation with respect to FD. The samples were mounted in the SAXS instrument with the incident beam perpendicular to the plane of the sample surface. In this geometry, the 2-D detector image directly showed the nano-scale orientation distributions in the plane of the sample.

Plots showing preferred orientation, i.e. intensity (I) vs. azimuthal angle (χ), were produced from the 2-D SAXS profiles by integrating over the scattering angle (2θ). The long period was determined from the Lorentz plots (q^2I vs. q) [88,89] of the background-corrected scattering data, where $q = (2\pi/\lambda)\sin(2\theta)$, 2θ is the scattering angle and λ is the wavelength of the X-ray used. It is worth noting that the Lorentz correction also tended to shift the maximum peak position to higher q values.

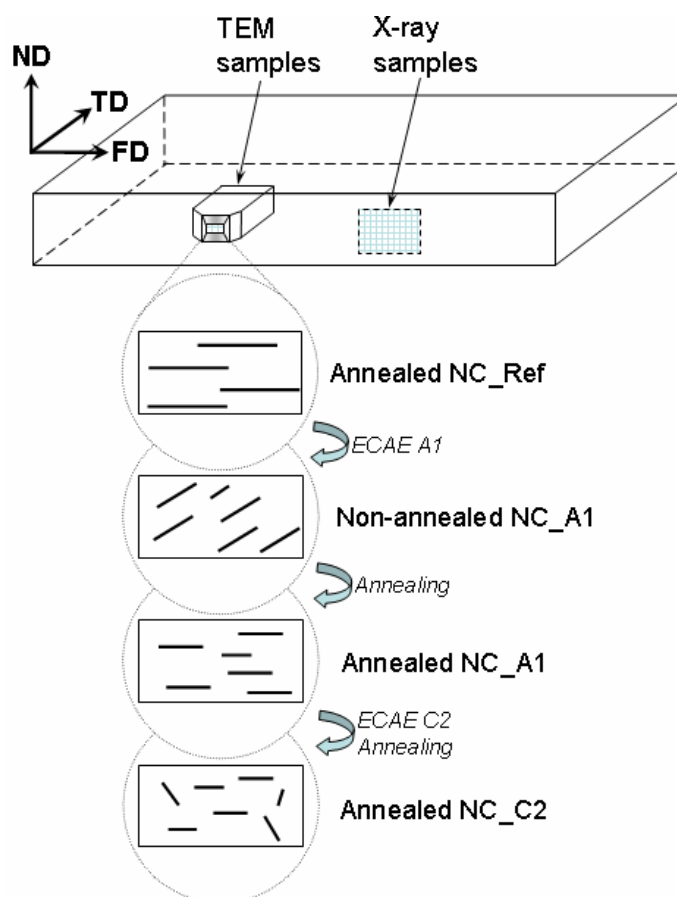


Fig. 4.1 Schematic of the specimens used for TEM and X-ray observations, and the clay orientation with respect to the ECAE processing and annealing. ND = normal direction, TD = transverse direction and FD = flow direction.

4.2.4 DSC measurements

Non-isothermal crystallization behavior of both nylon-6 and nylon-6/clay nanocomposites was investigated using a Perkin-Elmer Pyris-1 instrument. Samples weighing approximately 10 mg were excised from the center region of the plaque for

DSC measurements. All samples were sealed in aluminum pans and were situated in a nitrogen atmosphere during testing. Both DSC first heat and second heat scans were employed. The first heat was performed by heating the samples from 25 °C to 300 °C at a heating rate of 10 °C/min, subsequently held for 1 min at 300 °C, and then cooled to 25 °C at a rate of 10 °C/min. The second heat scan was performed while re-heating the sample to 300 °C at the same rate in order to assess the effect of the previous cooling scan.

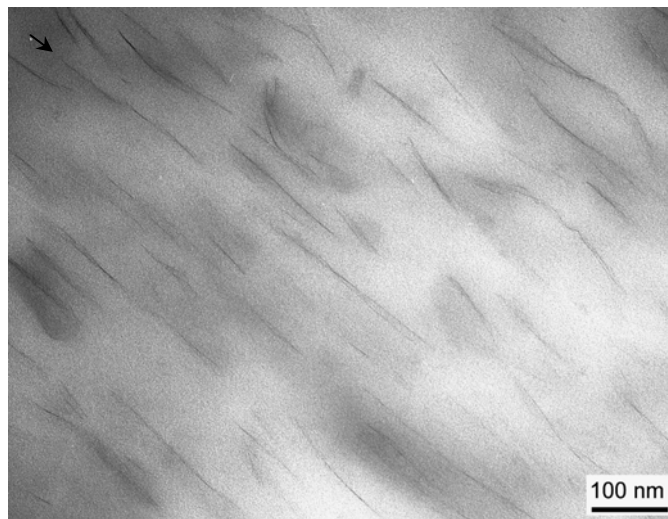
4.3 Results and Discussion

4.3.1 Morphological characterization of nylon-6 nanocomposites

The aspect ratio and orientation of nanoclays, before and after the ECAE process, are shown in Figs. 4.2 and 4.3. The reference nylon-6/clay nanocomposite, which received no ECAE processing, shows well-exfoliated clay layers with an orientation along the flow direction (FD) (Figs. 4.2(a) and 4.3(a)). However, the length and orientation of nano-clays in A1 and C2 nylon-6/clay nanocomposites have been changed by the ECAE process. A semi-automated image analysis scheme [53,90] is carried out to quantify the morphological variations in clay structures. Three different TEM micrographs from three different locations of each sample are used to ensure the statistical significance of the image analysis. The results of these analyses are given in Table 4.1. A detailed report of the image analyses can be found elsewhere [91].

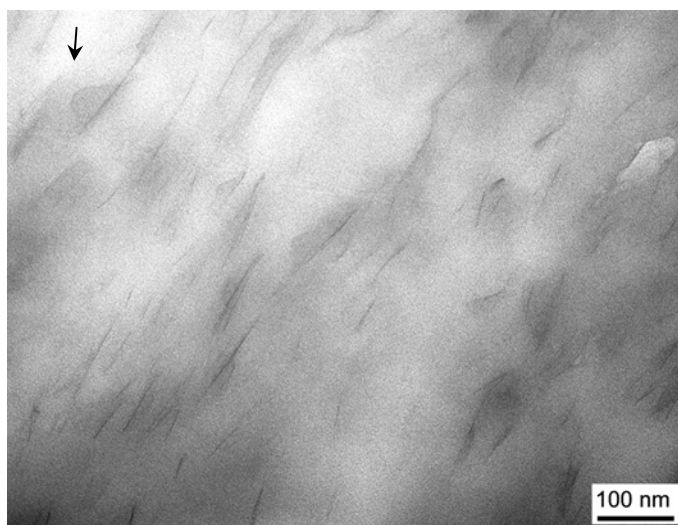
Based on clay morphological characterizations observed in TEM micrographs, a representation of clay orientation and aspect ratio with respect to the ECAE processing

direction can be ascertained (Fig. 4.1). It should be noted that after A1-ECAE process, the shortened clay layers [91] were aligned nearly parallel to the maximum simple shear direction [75], i.e. at an angle (θ) of 26° counterclockwise away from FD. Nevertheless, after annealing, the clay became oriented parallel to the FD. The annealed C2 composite exhibited a more random clay dispersion with lower aspect ratios.

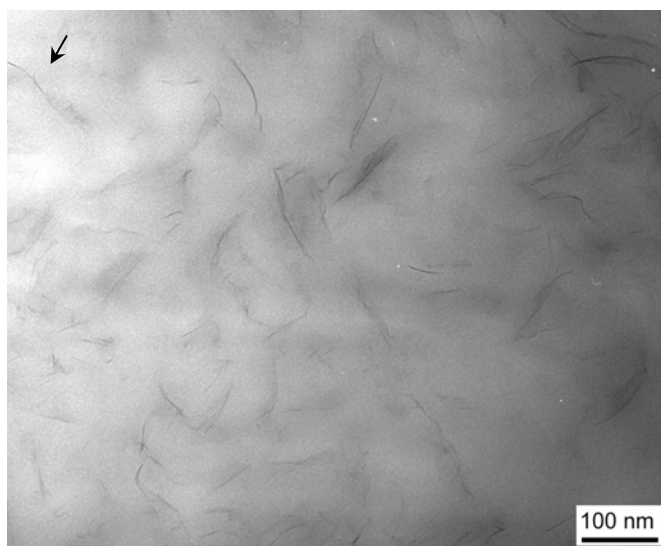


(a)

Fig. 4.2 Typical TEM micrographs of the simple-shear-processed and non-annealed nylon-6/clay nanocomposites (NC) used for image analysis: (a) NC_Reference, (b) NC_A1 and (c) NC_C2. The arrows indicate the flow direction.

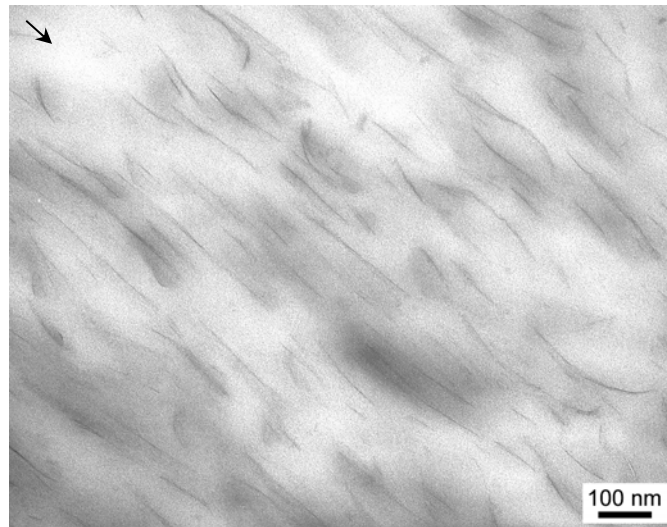


(b)

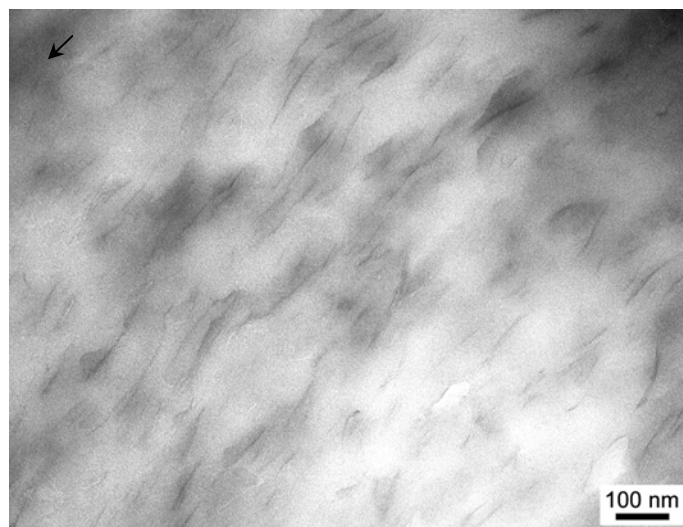


(c)

Fig. 4.2 Continued.

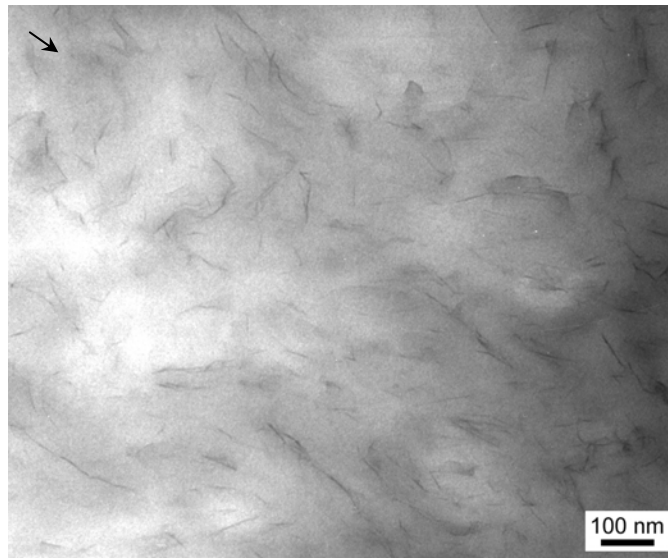


(a)



(b)

Fig. 4.3 Typical TEM micrographs of the simple-shear-processed and annealed nylon-6/clay nanocomposites (NC) used for image analysis: (a) NC_Reference, (b) NC_A1 and (c) NC_C2. The arrows indicate the flow direction.



(c)

Fig. 4.3 Continued.

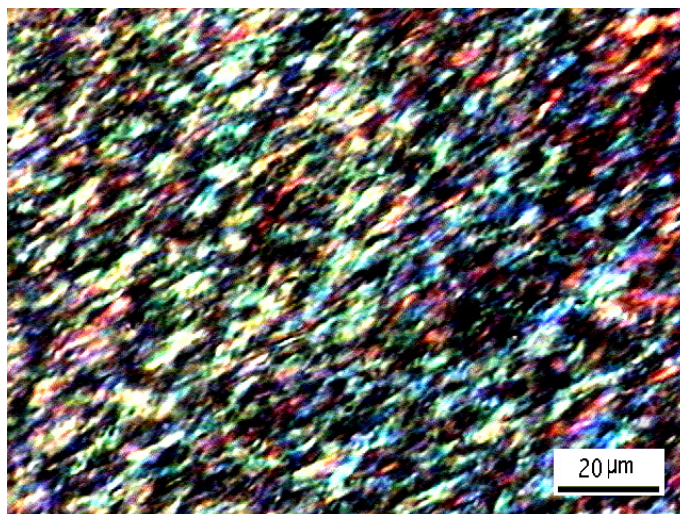
4.3.2 Morphological characterizations of neat nylon-6

Spherulitical Scale

Cross-polarized optical micrographs for the simple-shear-processed A1 nanocomposite prepared before and after annealing are shown in Fig. 4.4. All the samples are cut along the ND-FD plane with the viewing direction perpendicular to the ND-FD plane. Fig. 4.4(a) shows that the original spherulites are elongated into ellipsoids after the A1-ECAE process. However, the sample that was simple-sheared and then annealed (Fig. 4.4(b)) does not show much spherulite elongation, as shown in the

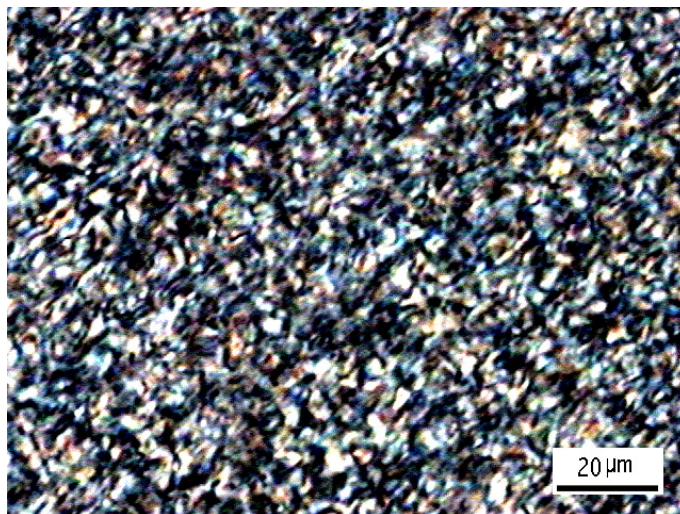
annealed reference nanocomposite (Fig. 4.4(c)). This implies that annealing has reduced the residual orientation in the matrix that was due to the ECAE simple shear process.

For comparison purpose, the OM micrograph of the annealed neat nylon-6 prepared under the same conditions is shown in Fig. 4.4(d). It is interesting to note that spherulite sizes found in the neat nylon-6 are much larger than those in their nanocomposite counterparts. This suggests that the introduction of the dispersed nanoclays to the nylon-6 matrix has possibly reduced the chain mobility and the spherulite size, leading to a decreased crystallinity in the nanocomposite systems (Table 4.1).

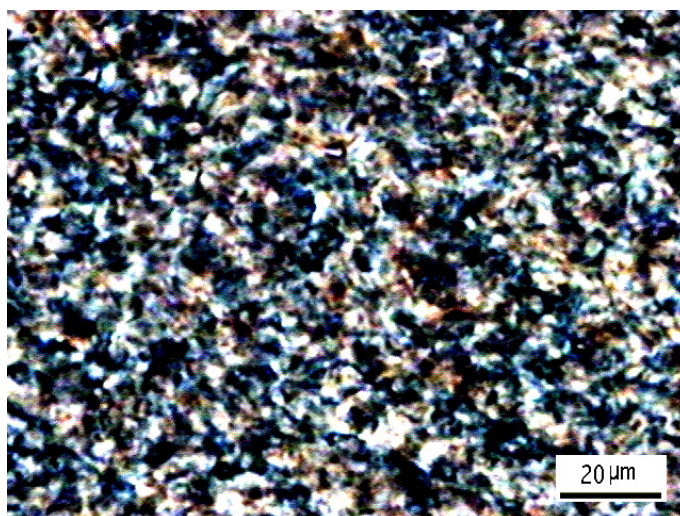


(a)

Fig. 4.4 Cross-polarized OM micrographs of the nylon-6 and nylon-6/clay nanocomposites: (a) simple-shear-processed and non-annealed A1 nanocomposite, (b) simple-shear-processed and annealed A1 nanocomposite, (c) non-simple shear processed and annealed reference nanocomposite and (d) non-simple shear processed and annealed neat nylon-6.

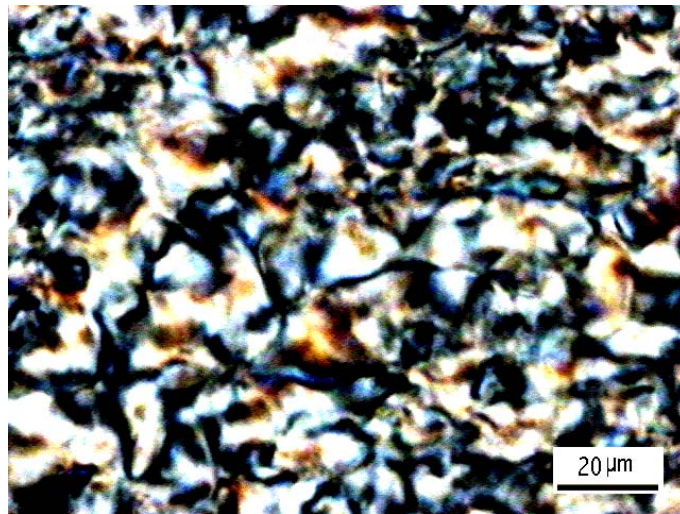


(b)



(c)

Fig. 4.4 Continued.



(d)

Fig. 4.4 Continued.

Table 4.1

Characteristic parameters of the neat nylon-6 and nylon-6/clay nanocomposites.

Property	Nylon-6 (Annealed)	NC_Ref (Annealed)	NC_A1		NC_C2	
			Annealing			
			Before	After	Before	After
TEM						
α_{platelet}	-	132±33	89±24	87±26	80±25	78±21
$S_{\text{platelet}} (^\circ)$	-	12	7	10	25	24
$\xi_{\text{platelet}} (\text{nm})$	-	51±20	45±15	49±17	48±19	48±15
SAXS						
$q_{\text{max}} (\text{nm}^{-1})$	0.71	0.81	1.16	0.93, 0.78	0.86	0.88, 0.77
$L_{\text{lamella}} (\text{Å})$	88.5	79.5	57.2	67.6, 80.6	73.1	71.4, 81.6
$\omega_{\text{lamella}} (^\circ)$	-	41	42	45, 89	47	39, -10, 86
FWHH ($^\circ$)	-	40	30	30	70	40, 50
WAXS						
$\chi_{\text{c}} (\%)$	39.2	29.2	28.4	29.0	27.8	28.7

†: α_{platelet} is the platelet aspect ratio (the platelet thickness was 0.94 nm [53]), S_{platelet} is the degree of platelet from unidirectional reinforcement, ξ_{platelet} is the correlation length between the dispersed platelets, L_{lamella} is the long period ($=2\pi/q_{\text{max}}$), ω_{lamella} is the lamellar orientation away from the flow direction, and χ_{c} is the crystallinity (the ratio of the areas of the crystalline reflections to that of total areas of the scattering curves).

Lamellar Scale

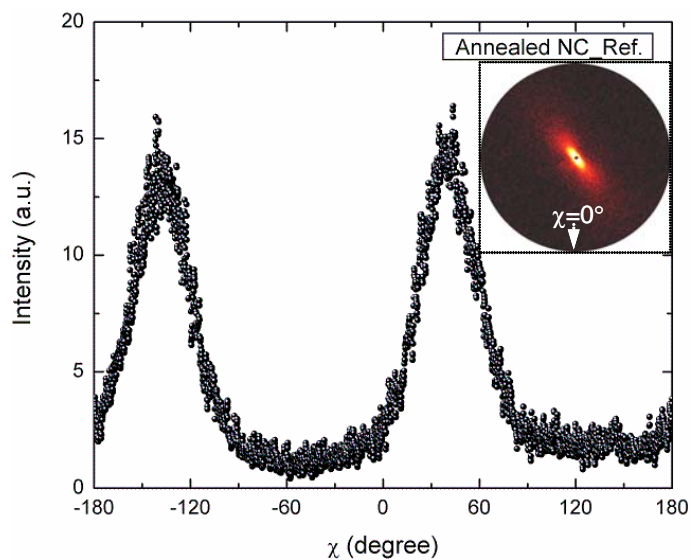
Fig. 4.5(a) shows the as-collected 2-D SAXS profile and intensity (I) vs. azimuthal angle (χ) plot for the annealed reference nanocomposite, which received no ECAE processing. The presence of preferred orientation of the lamellae within the sample is evident from the anisotropic SAXS scattering pattern. In such a 2-D SAXS image, the scattering angle (2θ) is zero at the center and increases with increasing radius. Azimuthal angle (χ) was set to zero at the 6 o'clock position of the detector plane and increased counter-clockwise. The I vs. χ plots were generated by integrating over scattering angle (2θ) from 0.7° to 1.6° . When transformed into real space, those angles correspond to a d-spacing equals 55 \AA to 126 \AA . This means that the strong scattering patterns observed in the I vs. χ plot should be assigned to the crystalline lamellae of nylon-6 since the diffraction from the low volume fraction (0.8 vol%) clay layers which is oriented parallel to the FD is nearly negligible at those scattering angles.

Based on the I vs. χ plot, the annealed reference nanocomposite shows a pair of strongly oriented scatterings, which indicates that the long period lies along the direction of $\sim 49^\circ$ clockwise away from the clay orientation direction, i.e. the crystalline lamellae are oriented preferentially $\sim 41^\circ$ counter-clockwise away from the clay orientation. Note that the clay layers are oriented parallel to FD (Fig. 4.1). In comparison, for the neat nylon-6 under the same condition, no preferred orientation of nylon-6 crystalline lamellae (Fig. 4.5(b)) was found. It can thus be concluded that the incorporation of high-aspect-ratio clay layers into the nylon-6 matrix has played an important role in the preferred orientation of nylon-6 crystallites.

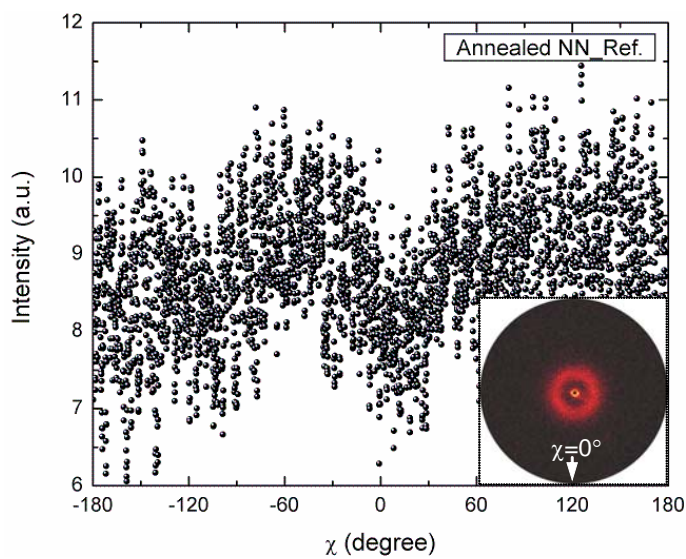
Figs. 4.5(c)-(f) show I vs. χ plots and as-collected 2-D SAXS profiles for the ECAE-processed nanocomposites before and after annealing. It is interesting to note that the non-annealed A1 nanocomposite (Fig. 4.5(c)) still exhibits a pair of preferred lamellar orientations along the direction of $\sim 43^\circ$ counter-clockwise away from the FD, despite the clay orientation shown in Fig. 4.1. A possible interpretation is that the crystalline lamellae are also aligned and closely packed to each other along the maximum simple shear plane since the interlamellar amorphous material is easily sheared and compressed during the A1-ECAE process [75]. It should be noted that the annealed A1 composite (Fig. 4.5(d)), which contains clay with a smaller aspect ratio and better alignment compared with those of the reference nanocomposite, exhibits another weak preferred lamellar orientation that is nearly perpendicular to the clay layers. This implies that the size of clay layers has an effect on the lamellar orientation of the nylon-6 matrix. During *in-situ* polymerization of nylon-6/clay nanocomposites, a large fraction ($\sim 32\%$) of nylon-6 chains is subjected to end-tethering to the clay surface through ionic interactions [1]. Due to those confinements of the nylon-6 chains, lamellar orientation may be governed significantly by the clay orientation, unless the confinements are relaxed by external factors. A decrease in aspect ratio may be considered one of the external factors dictating relaxation. Therefore, the reduction of clay length by the A1-ECAE process leads to increased relaxation of the constrained chains and provides enough room for lamella rearrangement. Moreover, the annealing step provides sufficient activation energy for the formation of weak preferred lamellae. Careful observation suggests that the weak preferred lamellar orientation is consistent with the

direction of recovery of closely packed lamellae during the annealing process. Additionally, the full width at half height (FWHH) value of the annealed A1 nanocomposite is smaller than that of the annealed reference, indicating that the lamellae of the annealed A1 nanocomposite are better aligned than the control sample. This is in good agreement with results of TEM image analysis for clay orientation (Table 4.1). Furthermore, this observation can partially support the above conjecture that the clay orientation globally dictates the lamellar orientation due to interfacial interactions.

The I vs. χ plots and 2-D SAXS profile of the non-annealed C2 nanocomposite show that the FWHH value increases after the C2-ECAE process (Fig. 4.5(e)). High FWHH values indicate broad orientation distribution. Therefore, the second pass in the C2 ECAE process has removed some orientation introduced by the first pass in A1 process. As shown in the metal systems [71], the second pass in C2 process can lead to micro-, or nano-domain rotation. In this study, it is possible that the second pass has led to the rotation of the nano-clays. Depending on the rigidity of the nano-clay sheets, some of the clays may likely become fractured during the rotation and re-organization in C2 process [91]. In other words, the clay sheets have been rotated and shortened slightly during the C2-ECAE process with a 180° rotation of the sample. Furthermore, the annealing (Fig. 4.5(f)) helps to cause a secondary lamellar orientation, which is nearly parallel to the flow direction and originates from the translation of molecular chains tethered to the rotating clay surface. Fig. 4.6 shows the schematic of lamellar orientation with respect to the ECAE processing direction.

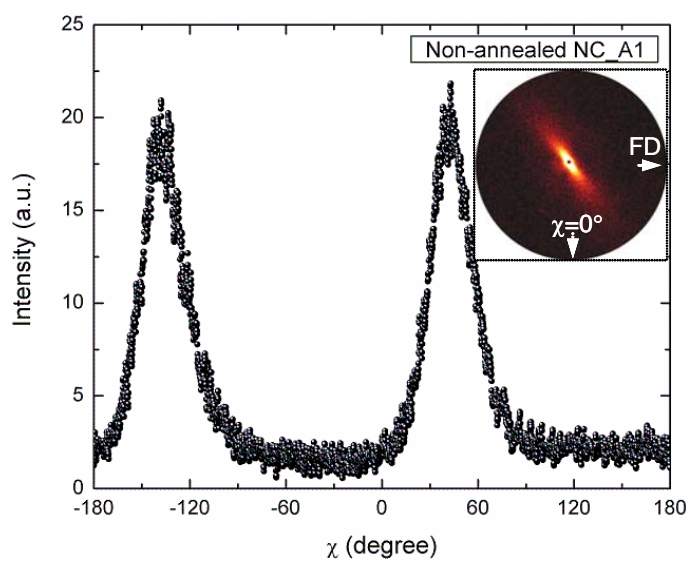


(a)

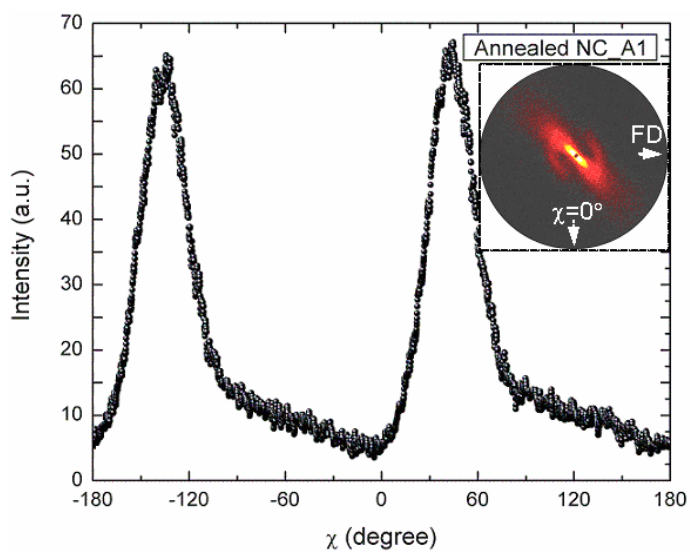


(b)

Fig. 4.5 The intensity (I) vs. azimuthal angle (χ) plots and the as-collected 2-D SAXS profiles for the nylon-6 and the nanocomposites: (a) annealed NC_Reference, (b) annealed nylon-6, (c) non-annealed NC_A1, (d) annealed NC_A1, (e) non-annealed NC_C2 and (f) annealed NC_C2.

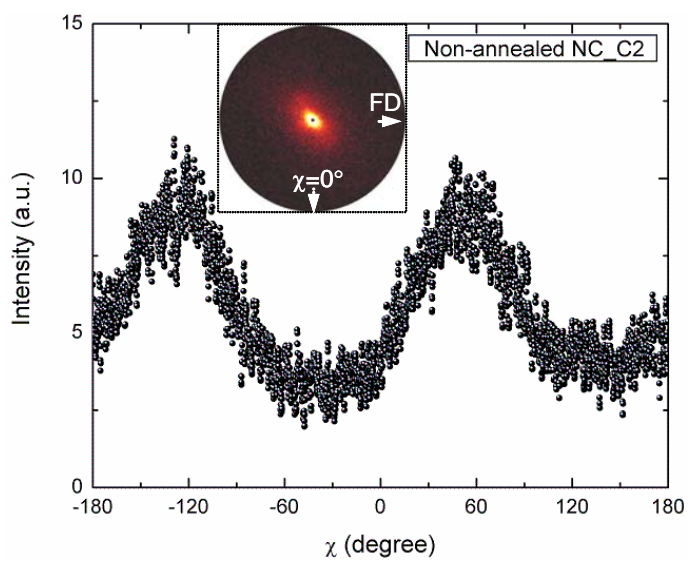


(c)

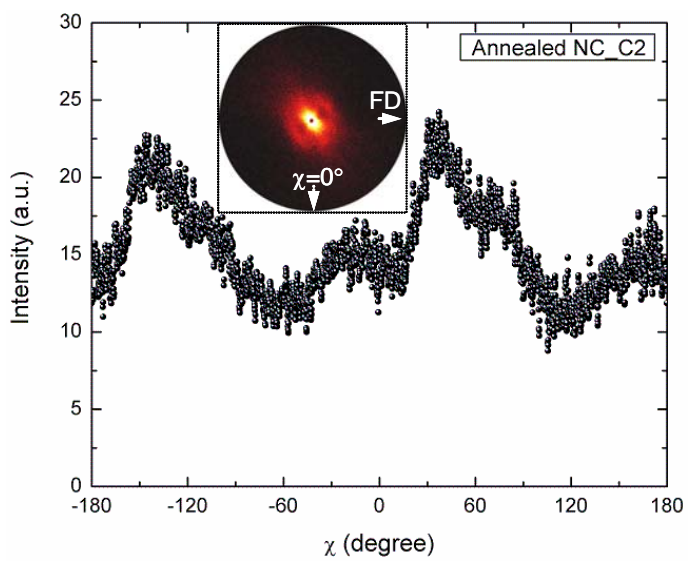


(d)

Fig. 4.5 Continued.



(e)



(f)

Fig. 4.5 Continued.

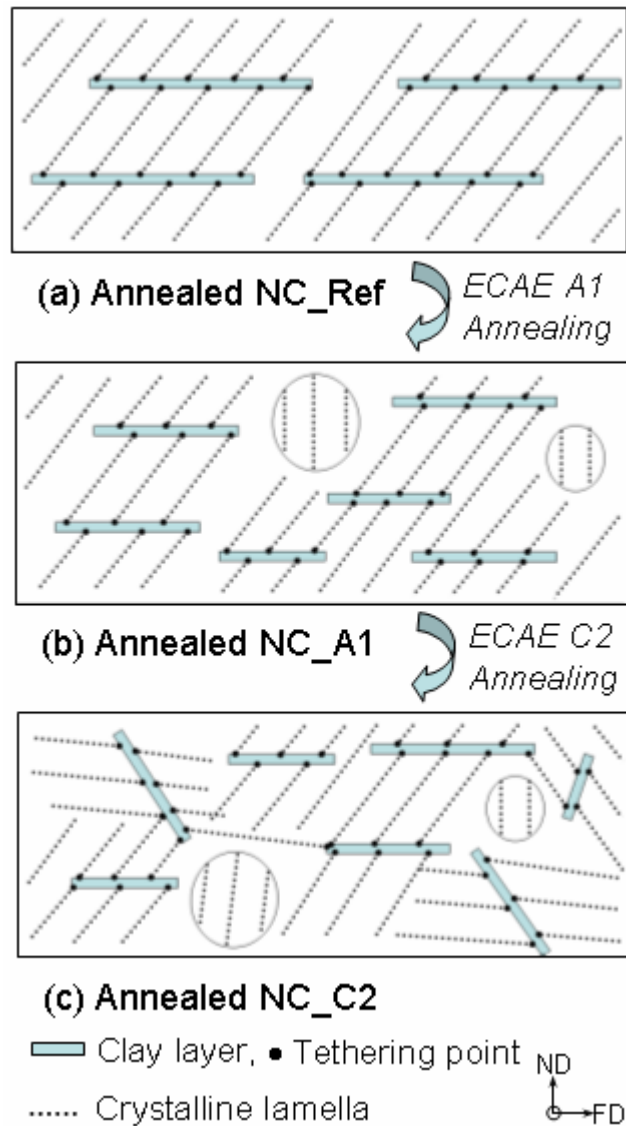


Fig. 4.6 Schematic of the lamellar orientation with respect to the ECAE processing and annealing: (a) annealed NC_Reference, (b) annealed NC_A1 and (c) annealed NC_C2.

Fig. 4.7 shows the Lorentz plot for the annealed A1 nanocomposite, which has an anisotropic distribution of lamellae. The long period of the anisotropic sample is determined by integrating a wedge-shaped region spanning the FWHH of one of the preferred orientation lobes, while for the isotropic sample (e.g., the annealed neat nylon-6), the entire 2-D profile is integrated over the whole range of azimuthal angles ($0^\circ \leq \chi \leq 360^\circ$). The annealed A1 nanocomposite shows that q_{\max} is 0.78 nm^{-1} , which yields a long period (L_{lamella}) of 8.06 nm. The long periods were determined in this same manner for all samples investigated and are listed in Table 4.1. After the A1-ECAE process, the long period decreases slightly due to the packing of crystalline lamellae. Still, the annealing process has increased the long period: its value is almost equal to that of the annealed reference nanocomposite.

Additional TEM observation was performed to confirm the SAXS results on the exfoliated nylon-6/clay nanocomposites. Fig. 4.8 is a TEM micrograph of the annealed reference nylon-6/clay nanocomposite that was cut from the center of plate. This demonstrates that the fine lamellae of the nylon-6 crystallites are oriented preferentially along the direction $\sim 41^\circ$ counter-clockwise from the clay orientation. This finding is in excellent agreement with the SAXS result. Interfacial ordering of crystalline lamellae may be a result of the interfacial interaction. As mentioned previously, the ends of nylon-6 chains are bound to the clay surface through ionic interactions. Once nylon-6 molecules are densely tethered to clay surfaces, the chain segments are oriented perpendicularly to clay surfaces [41]. Thus, the crystalline lamellae formed from a bundle of these molecular chains are most likely oriented perpendicularly to the clay

surfaces, and the growing face of the lamellae (i.e. the hydrogen-bonded planes) is parallel to the interface if external stress does not affect the crystallization [86]. The samples, however, experience strong shear stresses during extrusion-injection molding, and the long-range ordering (~ 51 nm) of clay inter-spacing in the exfoliated nanocomposites may lead to easy shear deformation of nylon-6 chains during processing. These could be considered the primary reasons for diagonally oriented lamellar structures. Consequently, the orientation of crystalline lamellae is dictated by the global orientation of clay layers arising from extrusion-injection molding and the ECAE simple shear process: the lamellae orientation is, however, dependent upon the degree of post-process annealing.

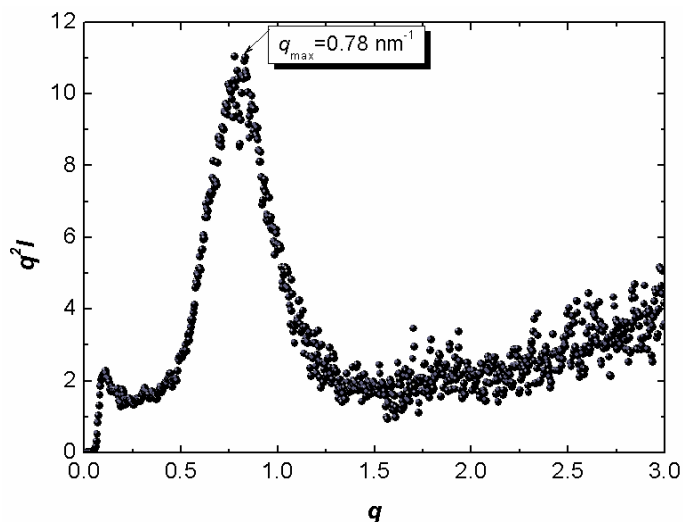


Fig. 4.7 Lorentz plot of the annealed A1 nylon-6/clay nanocomposite.

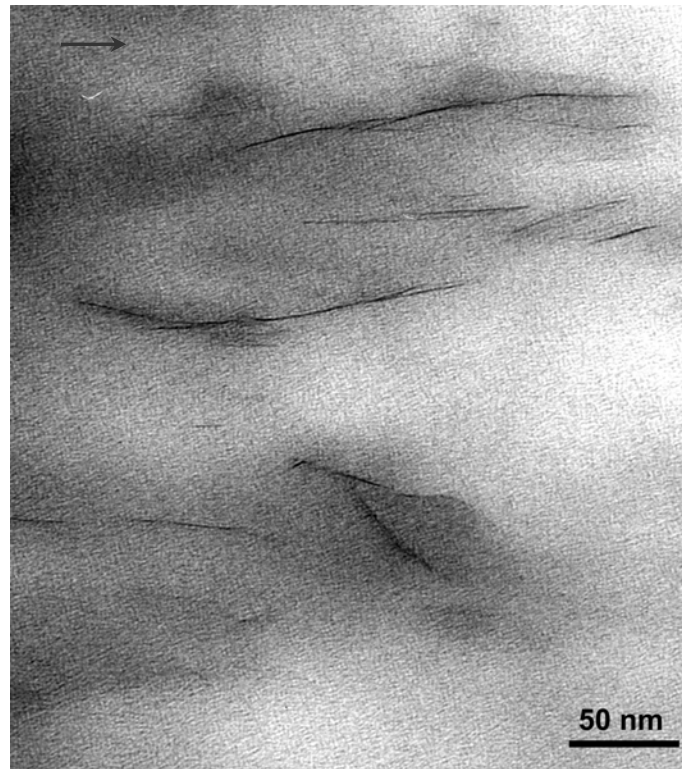


Fig. 4.8 TEM micrograph showing the lamellar orientation of the reference nanocomposite. The arrows indicate the flow direction.

Crystallographic scale

WAXD profiles of the annealed nylon-6 and nanocomposite samples are shown in Fig. 4.9. The peaks at $2\theta = 20.2$ and 23.7° , shown in the neat nylon-6, imply that the material is dominantly crystallized into an α -form: while the reference nanocomposite, having peaks at $2\theta = 10.6$ and 21.4° , shows that a γ -form is dominant. These WAXD results are in good agreement with earlier work by Lincoln *et al.* [85]. The WAXD study

helps to validate the hypothesis that the addition of nanoclay hinders chain mobility and facilitates the formation of γ -form crystals. It should be noted that the annealed A1 and C2 nanocomposites exhibit relatively strong α -phase and γ -phase peaks, implying that the clay aspect ratios and orientations play important roles in the formation of the γ -form. A decrease in clay aspect ratio may cause relaxation of chain mobility restrictions imposed in the high-aspect-ratio systems. Furthermore, annealing helps to transform the meta-stable γ -phase into the stable α -crystalline phase [77]. The degree of crystallinity (χ_c) for the annealed nylon-6 and nanocomposites is defined as the ratio of the areas beneath the X-ray scattering curve of the crystalline reflection to the total areas of amorphous and crystalline reflection (Table 4.1).

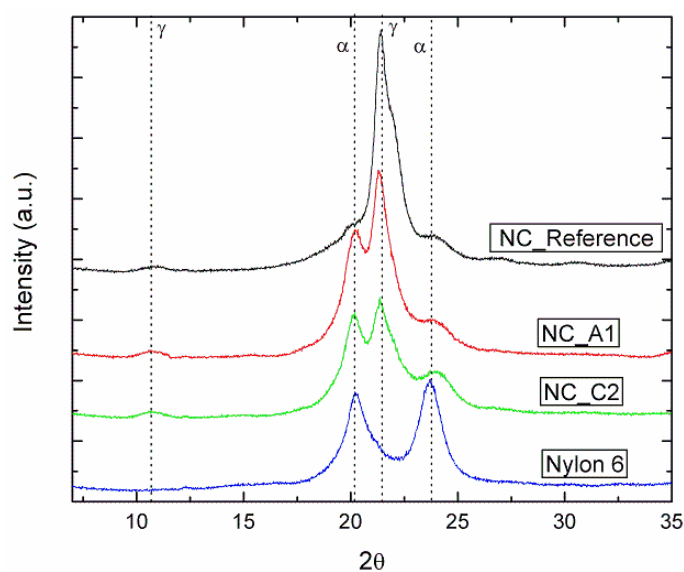


Fig. 4.9 WAXS profiles of the annealed nylon-6 and the nanocomposites.

DSC traces of the annealed samples of nylon-6 and nanocomposites show two melting peaks (Fig. 4.10). The high-temperature melting peak corresponds to the α -crystalline phase and the low-temperature peak corresponds to the γ -form. A higher level of γ -crystalline phase is observed in the reference nanocomposite, which is consistent with Kojima's study [1]. Interestingly, it is found that the amount of α -form increases as the clay aspect ratio and orientation decrease. These DSC results are also in good agreement with the WAXD results.

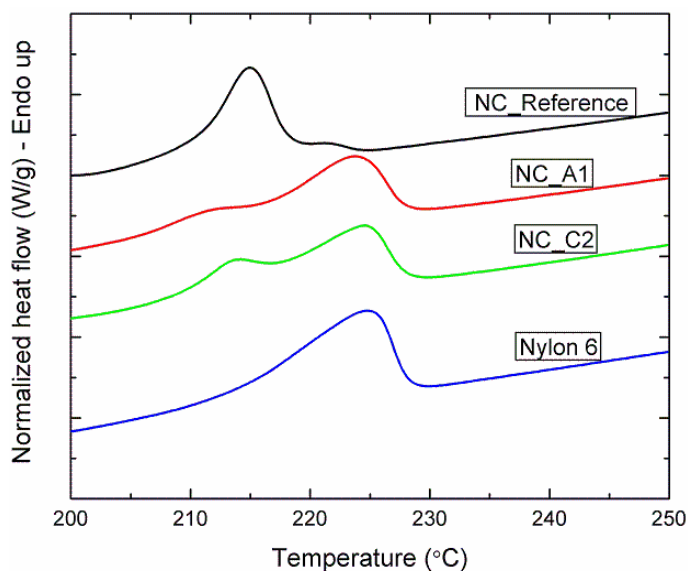


Fig. 4.10 DSC fusion endotherms of the annealed nylon-6 and the nanocomposites.

The morphological parameters at different length scales in the nylon-6 and nylon-6 nanocomposites are listed in Table 4.1. Nam *et al.* [92] proposed a hierarchical structure for intercalated polypropylene/clay nanocomposites based on the characteristic parameters obtained. Fig. 4.11 illustrates such a structure of the exfoliated reference nylon-6/clay nanocomposite used in this study. Despite a variation in clay aspect ratio and orientation, the correlation length (ξ_{platelet}) between the dispersed platelets and the long period (L_{lamella}) are nearly constant when compared with the annealed nanocomposites.

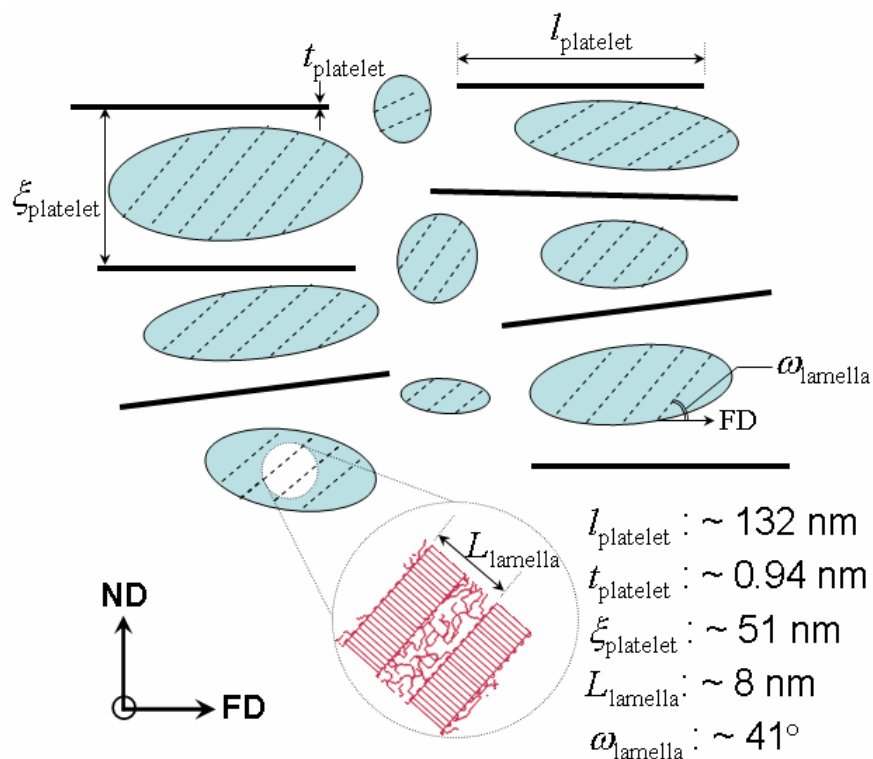


Fig. 4.11 Schematic of hierarchical structure and morphological parameters of the exfoliated reference nylon-6/clay nanocomposite.

Tethering of the polymer chains to the clay surface leads to a decrease in chain mobility and the confinement of lamellar orientation near clay layers. Reduced chain mobility may be responsible for smaller spherulites (Fig. 4.4(c)) and a decreased crystallinity (Table 4.1) of the nanocomposites compared with the neat nylon-6. This indicates that the effect of clay layers as nucleation sites is markedly suppressed during crystallization.

4.4 Summary

Experimental findings indicate that the morphological development of a semi-crystalline polymer in a clay-reinforced nanocomposite depends significantly upon the clay structural parameters, such as clay orientation, aspect ratio, and interfacial interactions between the clay surface and polymer chains. It is concluded that the orientation of crystalline lamellae is affected by the orientation and the size of clay layers. In addition, the clay orientation and aspect ratio affect the formation of a crystalline phase. The correlation length and the long period appear to be independent of the clay orientation and aspect ratio. Tethering of the polymer chains to the clay surface has resulted in a decrease in chain mobility and confinement of lamellar orientation, thereby a significant reduction in crystallinity.

CHAPTER V

EFFECTS OF CLAY ORIENTATION AND ASPECT RATIO ON MECHANICAL BEHAVIOR OF NYLON-6 NANOCOMPOSITE

5.1 Introduction

Filler-reinforced polymeric nanocomposite systems with well-dispersed inorganic nanoparticles typically exhibit significant improvements in physical and mechanical properties over their neat resin counterpart. The most commonly produced nanocomposite systems are polymer-layered silicate nanocomposites, which are of interest because of their exceptional reinforcement effects at very low clay loading. This characteristic has been exploited to prepare commercially viable structural components since minimized nanofiller loading results in a lighter structure, good processability, and increased ductility. Moreover, a negligible loss in fracture toughness is usually observed in such nanocomposite systems [1].

Layered silicates are composed of extremely thin (~1 nm), plate-like structures that have large surface areas and high aspect ratios. In addition, the platelets have an exceptionally high modulus compared to that of the surrounding polymer matrix. The reinforcement effect of polymer nanocomposites strongly depends on the filler's structural parameters, such as shape, aspect ratio, modulus, volume fraction, interfacial adhesion, surface characteristics and orientation [11-15]. Recent research efforts have focused on developing well-exfoliated nanocomposites using various processing

techniques (e.g., *in-situ* polymerization [24,36], emulsion polymerization [93,94], melt compounding [3,95,96], and sol-gel processing methods [37,97,98]): only limited success has been achieved [2,5,22,25,67,99-103]. Fornes *et al.* [103] investigated the effect of organic surfactant structure and molecular weights of nylon-6 on the mechanical properties of nylon-6 nanocomposites. Sue *et al.* [67] reported that, for α -zirconium phosphate-based epoxy nanocomposites, surface modifiers had a significant effect on the thermal properties and toughening mechanisms of the nanocomposites.

Using micromechanics-based composite models, a few of recent studies [53,55] have attempted to examine how the nanofiller structural parameters (e.g., shape, aspect ratio and orientation) affect the mechanical properties. Although these micro-mechanical models cannot be used to fully account for the exact mechanical behavior of polymer nanocomposites, it generally gives satisfactory correlations. Yet, there is no experimental effort within the literature to address how the aspect ratio and orientation of clay layered structures affect mechanical properties of polymer nanocomposites. This is partially owed to the fact that it is nontrivial to experimentally control the aspect ratio and orientation of nanoscopic fillers in a polymer matrix without simultaneously changing other material parameters. Therefore, there is a significant interest to experimentally prepare variations in nanofiller aspect ratios and orientations in polymer nanocomposites and study how they influence mechanical properties.

It has been shown that the presence of clay layers may affect the nucleation and growth of crystalline lamellae in nylon, resulting in the formation of complex morphologies within the matrix. Kojima *et al.* [1] found that the γ -crystalline phase

would dominate when clay layers are dispersed in a nylon matrix, whereas neat nylon exhibits a high level of α -form crystalline structure. Because it has been well-established that lamellar orientation can greatly affect the mechanical properties of semi-crystalline polymers, it is important to determine the nanoscale morphological characteristics of crystalline lamellar orientation as well as the clay orientation in nylon-6/clay nanocomposite.

The present paper attempts to study how the aspect ratio and orientation of clay layered structures affect the mechanical properties of nylon-6/clay nanocomposites. Characterization of nylon-6/clay nanocomposite morphology is presented elsewhere [104]. Creasy *et al.* [69] found that a large-scale simple shear process can control the fiber orientation of glass fiber/polyacetal composites, depending on the processing routes. Xia [71] also speculated that controlled nanoparticle orientation could be easily achieved through a simple shear process. The same simple shear process was, therefore, carried out to alter clay aspect ratios and orientations within the nylon-6 matrix.

Both the Halpin-Tsai and Mori-Tanaka micromechanics-based composite models were implemented to account for the effect of the nanofiller structural parameters on the reinforcement of the nanocomposites. The fundamental structure-property relationship of polymer nanocomposites, based on this micromechanical model, is discussed.

5.2 Continuum-based Micromechanical Models

A number of micro-mechanical composite models have been developed to describe the macroscopic mechanical properties of discontinuous, filler-based

composites [42-52]. Many assumptions are inherent in these micromechanical models. The detailed description and discussion of assumptions of these micromechanical models have been documented [53]. In conventional micromechanical models, filler volume fraction (ϕ_f), aspect ratio (α), orientation (S), and modulus (E_f) are important factors for describing the macroscopic composite properties. Tucker *et al.* [54] reviewed the application of several composite models for fiber-reinforced composites. They reported that the Halpin-Tsai theory [48-50] offered reasonable predictions for composite modulus. The model proposed by Mori-Tanaka [45,47] exhibited better predictive capabilities for fillers with relatively high aspect ratios. The longitudinal engineering modulus (E_{11}) of the Halpin-Tsai and the Mori-Tanaka model are expressed in equations (1) and (2), respectively.

$$\frac{E_{11}}{E_m} = \frac{1 + 2(l/t_p)\eta\phi_f}{1 - \eta\phi_f} \quad (5.1)$$

$$\eta = \frac{E_f/E_m - 1}{E_f/E_m + 2(l/t_p)}$$

where l is filler length and t_p is filler thickness and

$$\frac{E_{11}}{E_m} = \frac{1}{1 + \phi_f[-2\nu_m A_3 + (1 - \nu_m)A_4 + (1 + \nu_m)A_5 A]/2A} \quad (5.2)$$

where ϕ_f is filler volume fraction, ν_m is the Poisson's ratio of the matrix, and A , A_3 , A_4 , and A_5 are calculated from the matrix and filler properties and the components of the Eshelby tensor [43]. The above models were utilized to describe the clay reinforcement effect in nylon-6/clay nanocomposites.

5.3 Experimental

5.3.1 Materials

Commercially available nylon-6/clay nanocomposite pellets containing 2 wt% of layered silicate clay (commercial grade, 1022C2) and neat nylon-6 (commercial grade, 1022B) were provided by Ube Industries, Japan. The detailed description and the overall process for preparing the resin and nanocomposite are documented in [36,41]. Briefly, organic, surface-modified montmorillonite clay was prepared *via* a cation-exchange reaction with 12-aminolauric acid. The resulting ion-exchanged montmorillonite clay (termed 12-montmorillonite) was mixed with ϵ -caprolactam. Ring-opening polymerization of the ϵ -caprolactam, with addition of a small amount of 6-aminocaproic acid, was initiated by carboxyl ends (-COOH) of the 12-montmorillonite clay, resulting in the chains (~32% of nylon-6 chains) with cationic ammonium ends ($-\text{NH}_3^+$) tethered to the surface of negatively charged layer silicates.

5.3.2 Sample preparation

Pellets of the neat nylon-6 and nylon-6/clay nanocomposite were dried at 100 °C for 12 h, and were then slowly injection molded using a custom-built extrusion-injection molding machine powered by a HaakeBuchler Rheocord (system 40) machine with a screw revolving at 30 rpm. The temperature profiles of the extruder barrel were set at 235-245-255-260°C progressively toward the inlet of the injection mold, with the mold temperature set at 180 °C. After molding, the samples were immediately sealed in a

polyethylene bag and kept in a vacuum desiccator prior to use to avoid moisture absorption.

A large-scale simple shear process, termed equal channel angular extrusion (ECAE) [75,76], was performed to alter the aspect ratio and orientation of the clay nanoparticles. This ECAE process was carried out at 60°C and at an extrusion rate of 0.25mm/s using a servo-hydraulic mechanical system (MTS-810). The samples before and after ECAE were categorized as follow: (1) Reference, (2) A1-received a single ECAE pass, and (3) C2-received two ECAE passes with a 180° rotation of specimen between the passes (Fig. 5.1). Detailed description of the ECAE simple shear process can be found in [71-76]. After the sample preparation, all samples were annealed at 150 °C for 3h to minimize any pre-existing molecular and clay orientation in the matrix due to processing [77-81]. Furthermore, the annealing chamber was purged with nitrogen gas to minimize sample oxidation during annealing. After annealing, the specimens were cut to an appropriate size and polished to desired dimensions for mechanical testing and structural characterizations.

5.3.3 Microscopy and image analysis

Transmission electron microscopy (TEM) observations were conducted on a JEOL JEM-2010A TEM operating at an accelerating voltage of 200 kV. Ultra-thin sections of ~90 nm in thickness of nylon-6/clay nanocomposite were obtained, under cryogenic condition, using a Reichert-Jung Ultracut E microtome. A diamond knife was used for the thin-sectioning, and the thin-sections were placed on 100-mesh

Formvar/carbon-coated copper grids for TEM observation. Note that samples for TEM analysis were cut parallel to the ND-FD plane, as depicted in Fig. 5.2.

In order to determine the clay aspect ratio and degree of clay orientation in nylon-6/clay nanocomposites, a semi-automated image analysis procedure, described by Fornes *et al.* [53,103], was carried out.

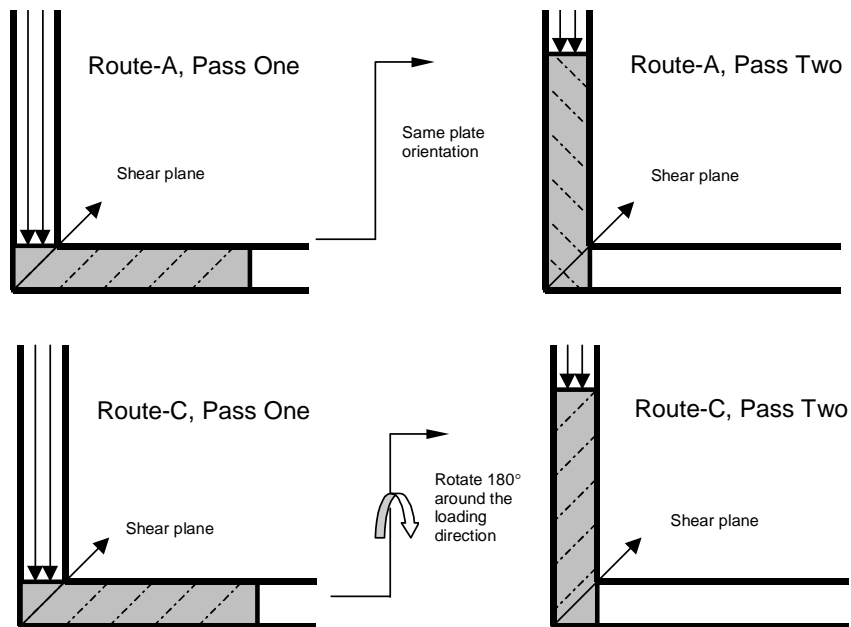


Fig. 5.1 Schematic of route A- and route C-ECAE processes.

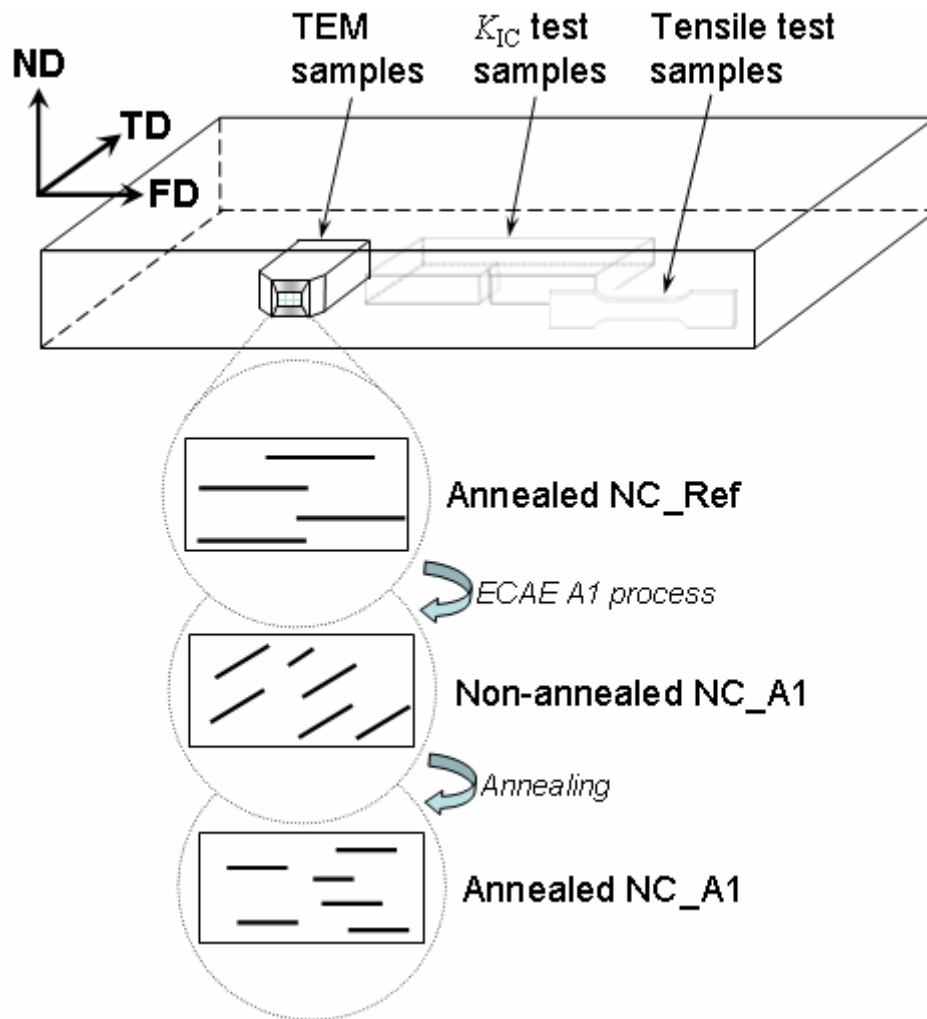


Fig. 5.2 Schematic of the specimens used for tensile, K_{IC} testing, and TEM observation, and the clay orientation with respect to the ECAE processing and annealing: ND = normal direction, TD = transverse direction and FD = flow direction.

5.3.4 Mechanical testing

Tensile properties were evaluated at room temperature according to ASTM-D638-02. The tensile specimens cut parallel to the flow direction (Fig. 5.2) were tested

using a screw-driven mechanical testing machine (Sintech II) at a constant crosshead speed of 0.085 mm/s (0.2"/min). An extensometer was used to measure the displacement in the gauge region. Young's modulus was calculated at 1% strain, and yield stress and elongation at break were determined in accordance with the above ASTM standard. The average values and standard deviations were determined from testing five specimens of each sample.

The stress intensity factor (K_{IC}) of the samples was obtained according to ASTM-D5045-99, with the K_{IC} specimens in a single-edge-notch 3-point-bend (SEN-3PB) geometry. By tapping a liquid-nitrogen-chilled razor blade into the wedge, thumb nail-shaped sharp cracks were generated. The ratio of the initial crack length (a) to the specimen width (W), a/W , was fixed between 0.4 and 0.6. The crack propagation was parallel to the transverse direction (Fig. 5.2). Five specimens from each sample were tested at room temperature and at a crosshead speed of 10 mm/min, using a screw-driven mechanical testing machine (Instron Model 1125).

The dynamic mechanical analysis (DMA) tests were performed under torsional mode on a Rheometric Mechanical Spectrometer (RMS-800) at temperatures ranging from -140 to 250°C. The DMA specimens were cut parallel to the flow direction. Measurements were made at 5°C per step with 45s of soaking time. The spectrometer was set to produce a sinusoidal wave function with a peak strain of 0.1% and frequency of 1 Hz. The storage moduli versus temperature and $\tan \delta$ versus temperature profiles were recorded and reported. The glass transition temperature, T_g , was determined based on the maximum $\tan \delta$ peak temperature of the $\tan \delta$ versus temperature curve.

5.4 Results and Discussion

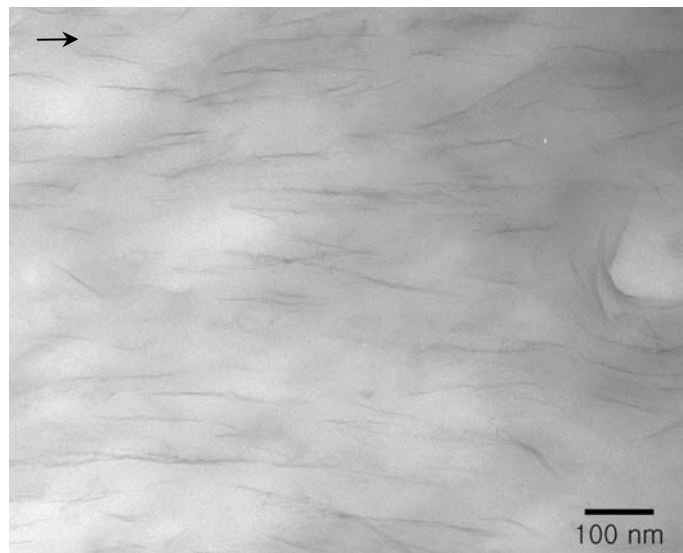
5.4.1 Microscopy investigation and image analysis

The morphology characterization of nylon-6/clay nanocomposite before and after ECAE process, and before and after annealing, has been described elsewhere [104]. Only the final morphologies of the nanocomposites are briefly reported here.

Fig. 5.2 shows the schematic of clay orientation with respect to the ECAE processing direction. It should be noted that after a one-pass (A1) ECAE process which induced the maximum shear strain of 180%, the shortened clay layers are aligned nearly parallel to the maximum simple shear plane [75], i.e. at an angle (θ) of $\sim 26^\circ$ counterclockwise away from the flow direction (FD). However, after annealing, the clay orientation becomes parallel to the FD. This clay orientation recovery is most likely due to the thermally activated relaxation of molecular/lamellar orientation of the nylon-6 matrix and the pre-existing residual stresses [75,76]. Figs. 5.3 and 5.4 show the TEM micrographs that indicate different clay aspect ratios and orientations of the ECAE-processed nanocomposite samples before and after annealing. The reference nylon-6/clay nanocomposite, which received no ECAE simple shear deformation, exhibits a well-exfoliated clay structure with an orientation along the FD (Figs. 5.3(a) and 5.4(a)). Also, it is observed that the clay lengths and orientations of the A1 and C2 nylon-6/clay nanocomposites have been altered upon the ECAE simple shear process.

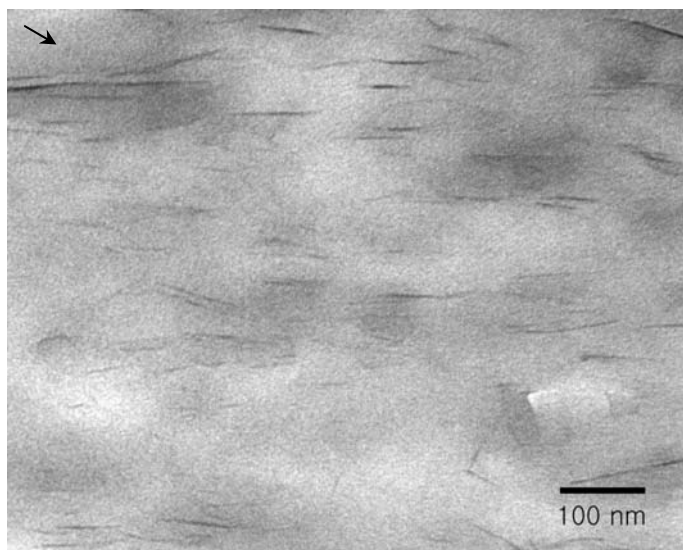
Fig. 5.5 shows the schematic of lamellar orientation with respect to the ECAE processing direction. The exfoliated nanocomposites exhibit a global orientation of clay layers, arising from the flow-induced alignment and local orientation of crystalline

lamellae caused by the clay particles. The annealed reference nanocomposite shows that the crystalline lamellae are oriented preferentially along $\sim 41^\circ$ counter-clockwise away from the clay orientation. For the annealed A1 and C2 nanocomposites, a reduction in clay aspect ratio helps to form another weak preferred lamellar orientation, which is almost perpendicular to the clay layer orientation. In addition, a misalignment in clay orientation leads to a more randomized lamellar orientation in the annealed C2 nanocomposite. The detailed experimental procedure for obtaining the above morphological features is reported elsewhere [104].

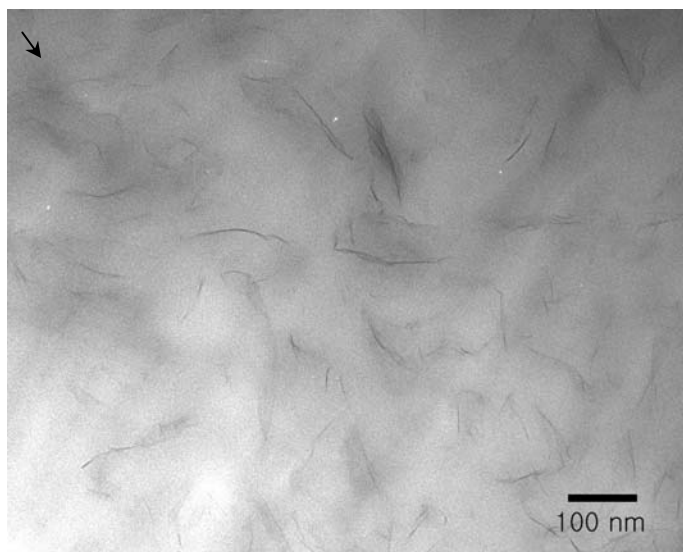


(a)

Fig. 5.3 Typical TEM micrographs of the simple-shear-processed and non-annealed nylon-6/clay nanocomposites (NC) used for image analysis: (a) NC_Reference, (b) NC_A1 and (c) NC_C2. The arrows indicate the flow direction.

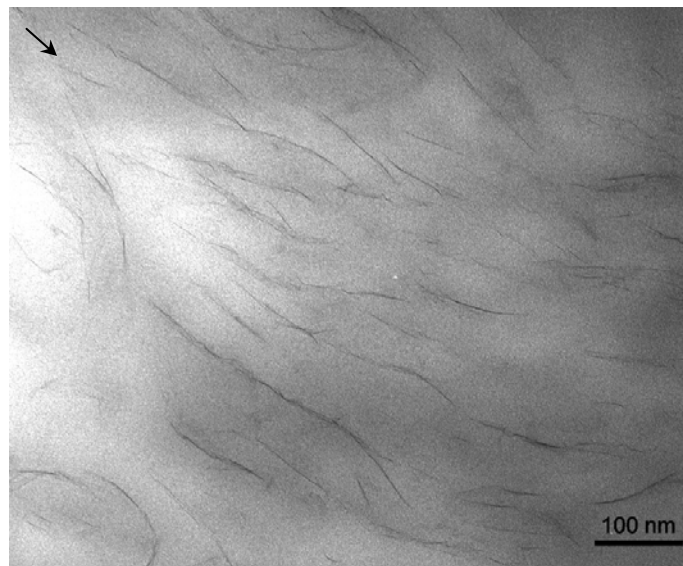


(b)

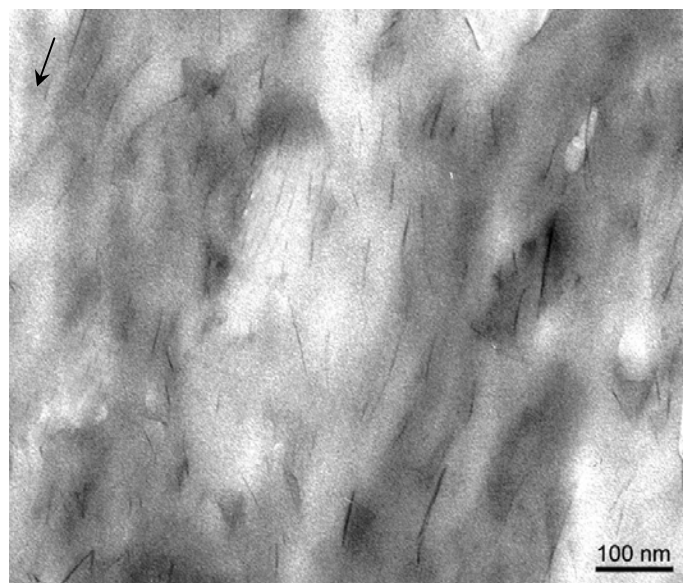


(c)

Fig. 5.3 Continued.

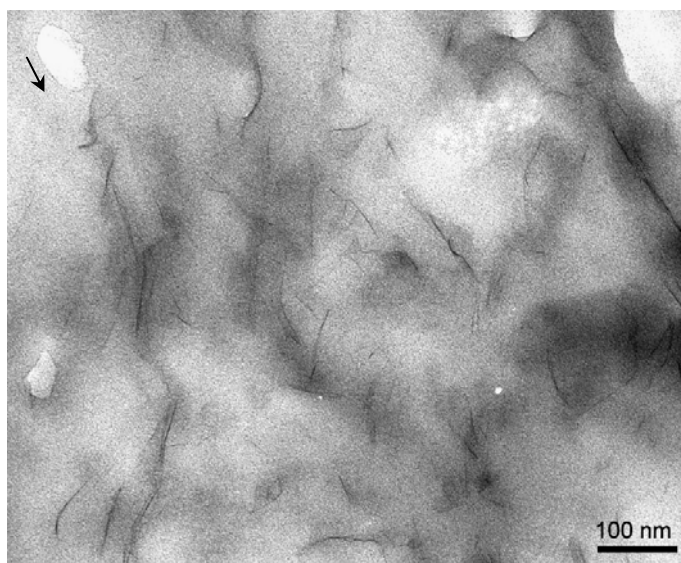


(a)



(b)

Fig. 5.4 Typical TEM micrographs of the simple-shear-processed and annealed nylon-6/clay nanocomposites (NC) used for image analysis: (a) NC_Reference, (b) NC_A1 and (c) NC_C2. The arrows indicate the flow direction.



(c)

Fig. 5.4 Continued.

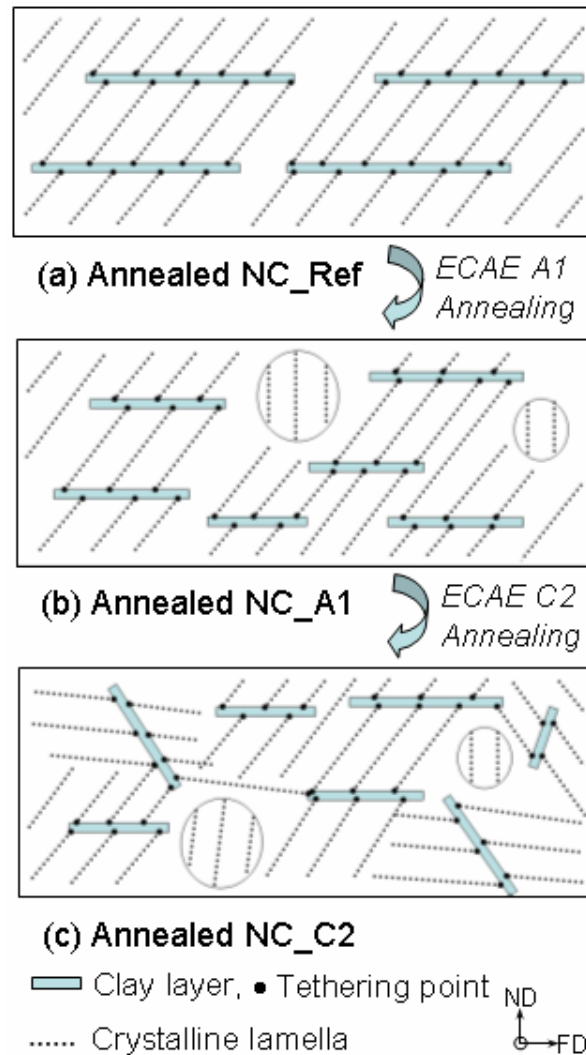


Fig. 5.5 Schematic of the lamellar orientation with respect to the ECAE processes and annealing: (a) annealed NC_Reference, (b) annealed NC_A1 and (c) annealed NC_C2.

It is interesting to note that the C2-ECAE simple shear process can exert highly localized stresses to reduce the aspect ratio of clay. Fig. 5.6 shows the fractured clay layers after the C2-ECAE process, thus greatly reducing the aspect ratio of clay in the matrix.

A semi-automated image analysis scheme was performed to quantify these morphological variations. It should be mentioned that three different TEM micrographs from three different locations of each sample were used to ensure the reliability of the image analysis. The distribution and statistical boxplot of the platelet length for the annealed samples of the reference, A1, and C2 nanocomposites are shown in Fig. 5.7(a).

The aspect ratios (α) of dispersed platelets are determined by:

$$\alpha = \frac{\bar{l}}{\bar{t}} \quad (5.3)$$

where \bar{l} is mean platelet length and \bar{t} is mean platelet thickness.

It is well known that the commercial Ube nylon-6/clay nanocomposite used in this study is a fully exfoliated system. Thus, it is safe to take the mean platelet thickness to be 0.94 nm, which is the single layer thickness of the clay [29].

Fig. 5.7(b) shows the distribution and statistical boxplot of the degree of platelet orientation in the reference, A1, and C2 annealed nanocomposites. The degree of platelet orientation (S) is defined as

$$S = \sqrt{\frac{\sum_{i=1}^n (\Phi_i - \bar{\Phi})^2}{N}} \quad (5.4)$$

(i.e. standard deviation), where Φ_i is the actual platelet orientation ($0^\circ \leq \Phi \leq 90^\circ$), $\bar{\Phi}$ is the mean platelet orientation, and N is total number of platelets counted. It should be noticed that the degree of platelet orientation was determined in relation to the uniaxial tension orientation on which the tensile tests were performed.

The results of the image analyses are summarized in Table 5.1. Interestingly, these results indicate that the A1 process only reduces the clay aspect ratio, while the C2 route alters not only the clay aspect ratio but also the clay orientation due to the accumulated crisscross residual plastic deformation generated by an additional ECAE process with 180° rotation of the specimen (Fig. 1). It is noted that although there is little difference in clay aspect ratio, there is a slight variation in degree of orientation between the reference and annealed nanocomposites. This discrepancy may be caused by the relaxation of nylon-6 matrix during sample annealing. The details of the morphological characterization can be found elsewhere [104].

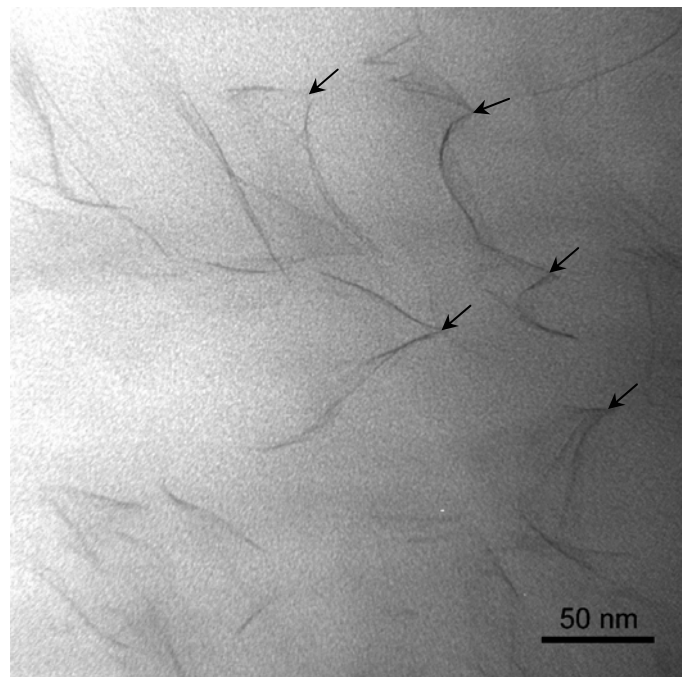
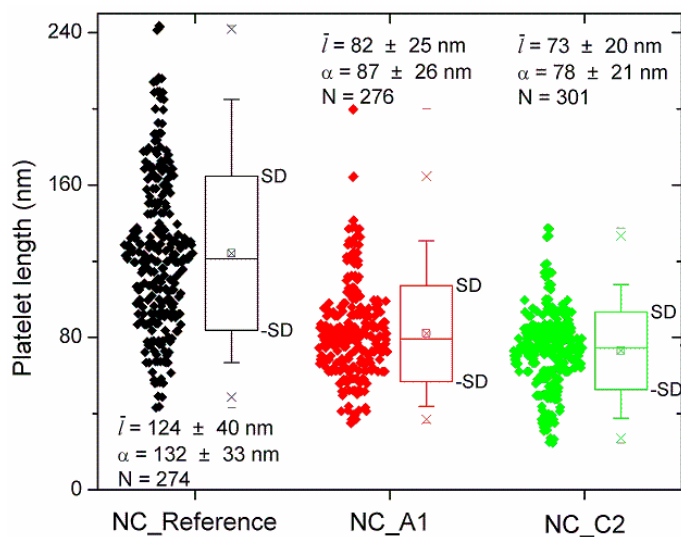
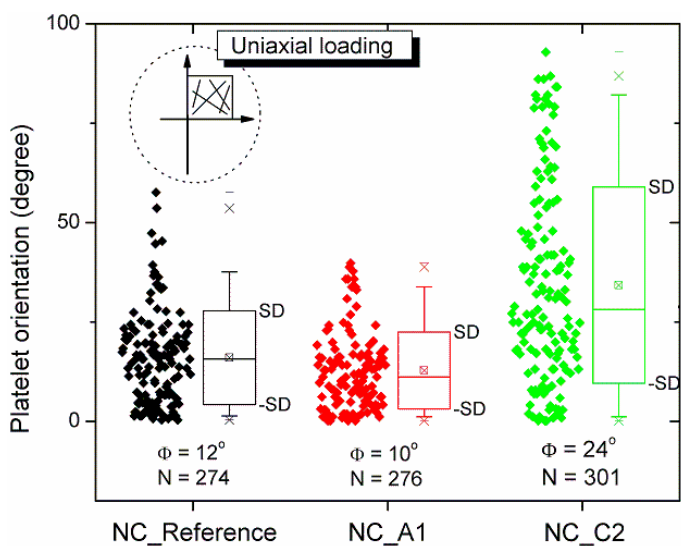


Fig. 5.6 TEM micrograph showing the fractured and shortened clays *via* an ECAE simple shear process. The arrows indicate the fractured clays.



(a)



(b)

Fig. 5.7 Quantitative TEM image analyses of the annealed nanocomposites: (a) clay length and (b) clay orientation (SD: standard deviation).

Table 5.1

The results of TEM image analysis for the reference, A1, and C2 nanocomposites.

Sample	Aspect ratio (α)		Degree of orientation (S) [*]	
	Annealing			
	Before	After	Before	After
NC_Ref	131±37	132±33	8°	12°
NC_A1	89±24	87±26	7°	10°
NC_C2	80±25	78±21	25°	24°

* Degree of platelet orientation from unidirectional reinforcement.

5.4.2 Mechanical properties

Typical engineering stress-strain curves and their key tensile property dependence on clay aspect ratio and orientation are shown in Fig. 5.8 and Table 5.2. All of the specimens tested were annealed samples. A decrease in aspect ratio from 132 to 87 causes an obvious reduction in modulus and yield stress. However, a slight increase in elongation at break is also observed. In addition to the change in aspect ratio, the degree of clay orientation has an effect on tensile properties. The annealed C2 nanocomposite, which has a more randomly dispersed clay and lower aspect ratio, exhibits a much lower modulus (~19 %) and yield stress (~10 %) than those of the annealed reference nanocomposite. For comparison purposes, the Young's modulus and the yield stress of non-annealed A1 nylon-6 are given to be 3.03 ± 0.13 GPa and 77.2 ± 1.7

MPa, respectively. These values are not much different from the annealed nylon-6 since the ECAE process on semi-crystalline polymers tends to only destroy spherulites and cause some lamellar orientation. No significant molecular orientation throughout the sample is observed [70,74-76]. Fig. 5.9 highlights the influences of clay aspect ratio and degree of clay orientation on the tensile properties. When normalized by the tensile modulus of the reference nanocomposite, a decrease in aspect ratio results in a distinctive decrease in Young's modulus. On the other hand, a large decrease (100%) in alignment of clay, seen in the C2 nanocomposite, seems to have a relatively small effect ($\approx 8\%$) on tensile modulus. Based on the above finding, the effect of clay aspect ratio on tensile properties appears to be more significant.

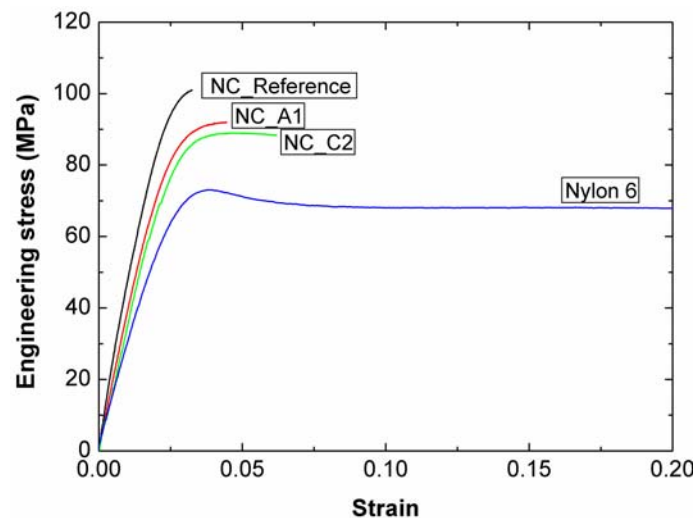


Fig. 5.8 Typical engineering stress-strain curves for the annealed neat nylon-6 and nanocomposites.

Table 5.2

Tensile properties of the neat nylon-6 and nylon-6/clay nanocomposites.

Sample	Young's modulus* (GPa)	Yield stress* (MPa)	Elongation at break (%)
NC_Ref	4.67±0.20	98.2±2.3	4.7
NC_A1	4.09±0.18	93.0±1.3	5.3
NC_C2	3.80±0.14	88.9±2.4	5.8
Nylon-6	3.14±0.11	76.4±1.2	45

*Standard deviation for the five samples tested.

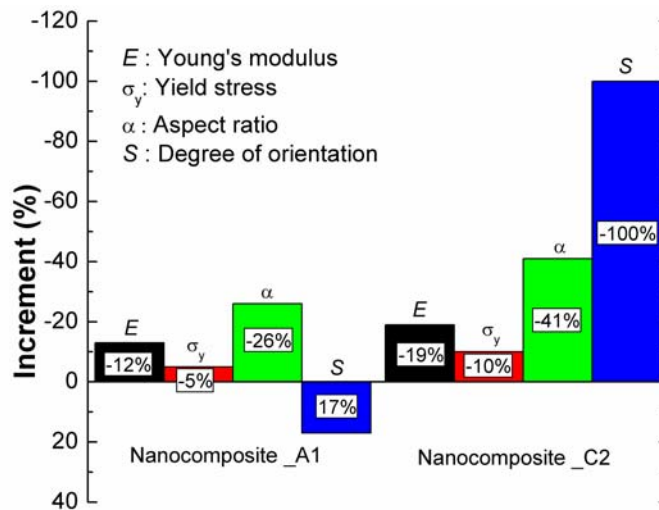


Fig. 5.9 Effect of clay aspect ratio and clay orientation on tensile properties for the ECAE processed and annealed nanocomposites.

The K_{IC} values for the annealed nanocomposites are given in Table 5.3. A reduction in aspect ratio and alignment of clay results in an improved fracture toughness. It is interesting to note that the clay orientation perpendicular to the crack propagation direction does not seem to improve fracture toughness. This suggests that the natural crack tip radius of the nylon-6/clay nanocomposite is too large compared to the clay dimensions to show an effect.

Table 5.3

Mechanical properties and heat distortion temperature of the neat nylon-6 and nylon-6/clay nanocomposites.

Sample	Storage modulus, G' (Pa)		K_{IC}^* (MPa·m ^{0.5})	HDT (°C)
	at 25 °C	at 100 °C		
NC_Ref	1.28E9	3.33E8	2.7±0.07	110
NC_A1	1.12E9	2.89E8	3.1±0.13	90
NC_C2	1.07E9	2.51E8	3.0±0.11	84
Nylon-6	1.05E9	1.94E8	3.0 ^a	75

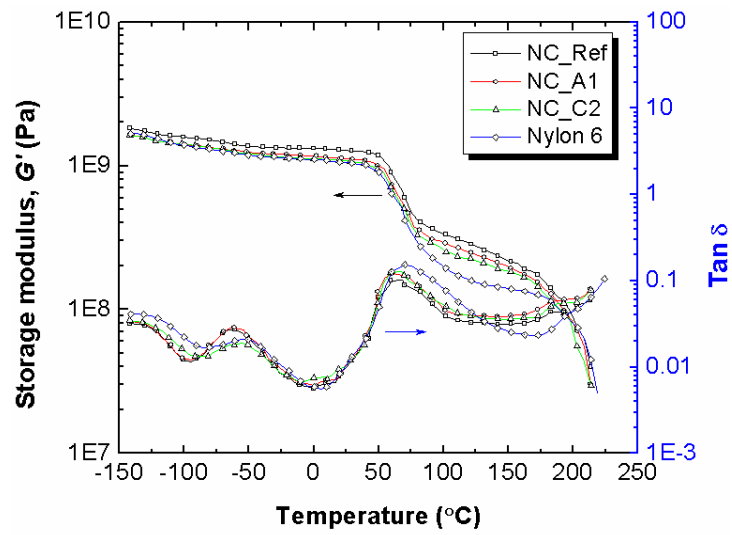
^a The value is quoted from [105].

* Standard deviation for the five samples tested.

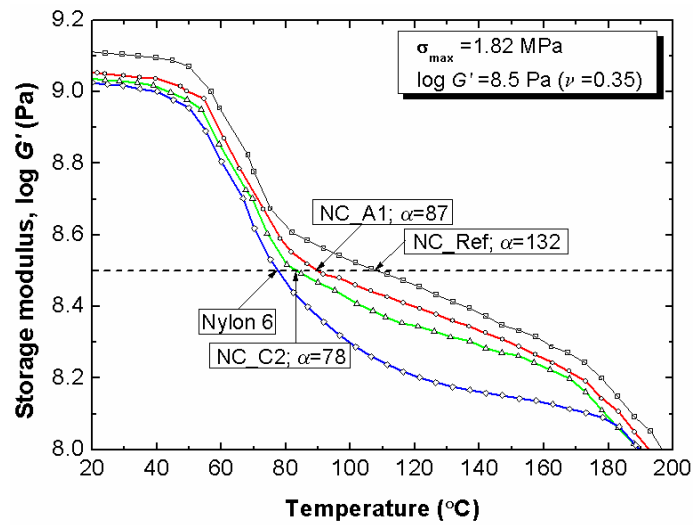
The dynamic mechanical properties for the annealed neat nylon-6 and nanocomposites are shown in Fig. 5.10. There is virtually no difference in T_g variation among the nanocomposites investigated. The addition of clay results in a significant increase in storage moduli throughout the whole temperature range studied (Table 5.3). The reinforcing effect of clay aspect ratio and orientation appears to be the highest at temperatures above T_g . This may be due to the fact that the exfoliated clay is most effective in resisting the mobility of the nylon-6 molecules above T_g .

The heat distortion temperature (HDT), defined as a deflection-temperature at which polymeric materials undergo an arbitrary deformation under a constant load, is one of the key indicators that can address load-bearing capabilities at elevated temperatures. Fig. 5.10(b) illustrates HDT values obtained from the storage modulus vs. temperature curve of DMA results [106]. A significant increase in HDT is observed in the annealed reference nanocomposite (Table 5.3), implying that high aspect ratios of nanofillers yields a significant increases in HTD.

It is noted that the lamellar orientations and crystallinity of nylon-6 [104] in the nanocomposites investigated remain more or less the same after annealing. Consequently, the ECAE process is unlikely to cause any significant changes in matrix properties. The mechanical properties variations reported above should, therefore, be mainly due to the changes in clay aspect ratios and orientations.



(a)



(b)

Fig. 5.10 Dynamic mechanical spectra for the annealed neat nylon-6 and nanocomposites: (a) storage modulus and loss tangent and (b) the HDT estimated from the plot of $\log G'$ vs. temperature.

5.4.3 Effective filler-based micromechanical models

The dispersion of fillers in a matrix is typically described in terms of exfoliation or intercalation. The fully exfoliated nanocomposites are considered to consist of single clay layers dispersed in a polymer matrix. While in the intercalated systems, inter-layer domains of fillers are typically penetrated by polymer chains and consequently stacked with an inter-layer spacing of 1-4 nm. However, conventional filler-based micromechanical models for predicting the modulus of nanocomposites do not consider the clay structural characteristics. Here, typical effective filler structural parameters are defined by the number of platelets per stacked clay (n) and the platelets inter-layer spacing (d_{001}): these parameters can be used to account for mechanical property enhancement for both exfoliated and intercalated nanocomposites. The mechanics-based model for effective filler structure is established by mapping the effective filler structural parameters (n, d_{001}) to the conventional filler structural parameters (α, ϕ_f, E_f).

The thickness of effective filler can be expressed in terms of n and d_{001} by the following equation [29]:

$$t_{\text{eff}} = (n-1)d_{001} + t_p \quad (5.5)$$

The effective filler aspect ratio (α_{eff}), volume fraction (ϕ_{eff}) and modulus (E_f^{eff}) can be written as [28]:

$$\alpha_{\text{eff}} = \frac{l}{t_{\text{eff}}} = \frac{l}{(n-1)d_{001} + t_p} \quad (5.6)$$

$$\phi_{\text{eff}} = \frac{\psi_{\text{eff}} [(n-1)d_{001} + t_p]}{n t_p} \cdot \frac{\rho_m}{\rho_f} \quad (5.7)$$

$$E_f^{\text{eff}} = \frac{n t_p E_f}{[(n-1)d_{001} + t_p]} \quad (5.8)$$

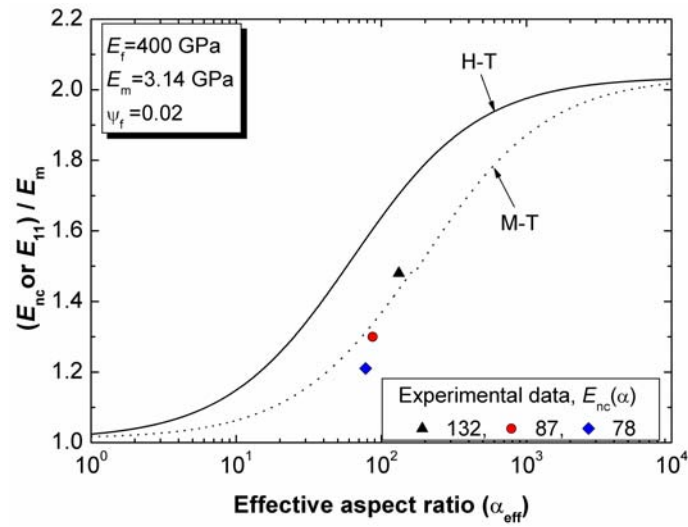
where ψ_{eff} is effective filler weight fraction and ρ_f and ρ_m are the densities of the filler and matrix, respectively. The influence of filler effective aspect ratio (α_{eff}) and orientation (S) on the modulus improvement was examined using the Halpin-Tsai (H-T) and Mori-Tanaka (M-T) theories. Similar trends are observed in the parametric study plots for both models (Fig. 5.11). The improved reinforcement efficiency is observed with the higher aspect ratio fillers. However, the Mori-Tanaka model is more conservative in estimation than the Halpin-Tsai model. This difference may originate from the discrepancies between assumptions inherent in the two models [53]. To compensate for these disparities, an adjustment of shape parameter ($2l/t_p$) in the Halpin-Tsai equation may be used. It should be noticed that E_{11}/E_m increases non-linearly with α_{eff} for both models (Fig. 5.11(a)). This underlying phenomenon may be explained by the load-transfer mechanism. The nature of these physics was well addressed in [55] using the shear lag model [51]. It should be mentioned that when the aspect ratios are 87 and 132, the clay length is sufficient for maximum load-transfer.

Disk-shaped platelets provide the same reinforcement in the two orthogonal directions: E_{11} and E_{22} . In the case of randomly oriented platelets, the following equation was proposed [107,108]:

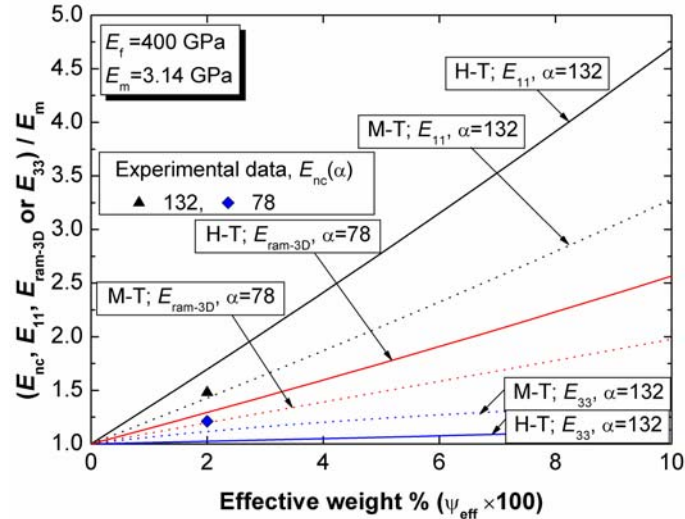
$$E_{\text{radom-3D}}^{\text{platelet}} = 0.49E_{11} + 0.51E_{33} \quad (5.9)$$

The effect of filler orientation (S) on modulus enhancement of nanocomposite was examined using the Halpin-Tsai and Mori-Tanaka theories (Fig. 5.11(b)). It was found that misalignment of unidirectional reinforcement leads to detectable modulus reductions. Experimental results are compared with model predictions from the Halpin-Tsai and Mori-Tanaka theories (Fig. 5.11). In the case of the clay filler modulus, E_f , it has been estimated to be 400 GPa based on molecular dynamic simulation [109]. The predictions of Mori-Tanaka model are in good agreement with the experimental data. Conversely, the Halpin-Tsai model slightly overpredicts the results. Note that the data for an aspect ratio of 78 in Fig. 5.11(a) needs to shift slightly to the left since the clay in the nanocomposite is more randomly oriented. It is also observed that the modulus of the C2 nanocomposite is in good agreement with the case for the radom-3D orientation.

Both experimental observations and micro-mechanical model predictions carried out in this study have clearly indicated that clay aspect ratio and orientation significantly affect the nanocomposite modulus. A high aspect ratio and unidirectional orientation lead to significantly improved moduli. Consequently, it is desirable to prepare polymer nanocomposites that exhibit full exfoliation with a preferred orientation along the tensile direction for maximum reinforcement effect.



(a)



(b)

Fig. 5.11 Effective filler-based model predictions of the Halpin-Tsai (H-T) and the Mori-Tanaka (M-T) theories: (a) clay aspect ratio (α) and (b) clay orientation (S) on the modulus improvement of exfoliated nanocomposites. Experimental data (E_{nc}) included.

5.5 Summary

Effects of aspect ratio and orientation on mechanical properties of nylon-6/clay nanocomposites were investigated. The aspect ratio and orientation of clay layers in nylon-6 matrix appear to be responsible for variations in mechanical properties. Unidirectional reinforcement and higher aspect ratios can lead to significant improvements in modulus, strength and heat distortion temperature, with a marginal loss in ductility. The effective filler-based Mori-Tanaka model offers a reasonably accurate prediction to account for modulus enhancement of the nanocomposites, which is consistent with experimental findings. Further, the model may be used to predict elastic properties of other types of polymer nanocomposites. The ECAE simple process appears to be an effective method for tailoring clay aspect ratios and orientations in nylon-6. The clay aspect ratio and orientation are dominating factors responsible for mechanical property improvements of these polymer nanocomposites.

CHAPTER VI

**IMPACT TOUGHENING MECHANISMS OF CALCIUM
CARBONATE-REINFORCED POLYPROPYLENE
NANOCOMPOSITE**

6.1 Introduction

It is well known that inorganic fillers are effective in improving stiffness, hardness, chemical resistance and dimension stability, as well as gas barrier properties of polymers [2,5,22,110-115]. Considerable literature can be found with focuses on improving mechanical properties of polypropylene (PP) using various kinds of fillers [30,34,114,115]. The effectiveness of inorganic fillers on improving physical and mechanical properties of PP strongly depend on the filler size, shape, aspect ratio, interfacial adhesion, surface characteristics and degree of dispersion [116-119].

Calcium carbonate (CaCO_3) particles have a nearly isotropic particulate structure [30]. The addition of such an inorganic rigid filler to a semi-crystalline polymer matrix may affect crystal structure, crystallinity, spherulite size, lamellar thickness and thickness of interlamella amorphous layers. Typically, inorganic particle-filled polymer composites show an increase in modulus but a decrease in toughness and ductility, mainly because of the induced stress concentration, agglomeration, and confinement of matrix molecular mobility around the rigid filler phase. However, a few exceptions have also been reported in the literature. In toughening polyethylene, CaCO_3 and chalk

particles have been shown to be able to improve toughness of PE effectively [31-33]. For PP, Thio and Argon [34] found that the CaCO₃-toughened PP composites could exhibit greatly improved impact strengths up to 40–50 kJ/m², as compared to 2–8 kJ/m² for that of neat PP. More recently, Chan *et al.* [30] showed that the fracture toughness of PP could be enhanced by over 300% by incorporating nanometer-sized (ca. 40 nm) CaCO₃ particles.

In this study, investigation will be focused on understanding the underlying toughening mechanisms responsible for the impressive toughening effect found in PP/CaCO₃ nanocomposite. Roles of CaCO₃ nanoparticles on PP crystalline size, crystalline structure, and the observed toughening effect are also studied and discussed.

6.2 Experimental

6.2.1 Materials

PP homopolymer, PD403 (density = 1.04 g/cc) from Basell USA, was used in this study. CaCO₃ nanoparticles were obtained from Guang Ping Nano Technology Group Ltd. The average primary particle size of CaCO₃ is about 44 nm. Irganox 1010[®] (Ciba Specialty Chemicals) was used as an antioxidant. The chemical composition of CaCO₃ nanoparticles was measured by inductively coupled plasma spectroscopy (Perkin Elmer Optima 3000 ICP) and the content of carbon and hydrogen was determined by a carbon, hydrogen and nitrogen analyzer (Table 6.1). The CaCO₃ nanoparticles used in this study were surface-modified by stearic acid.

Table 6.1

Chemical composition (wt%) of the CaCO₃ nanoparticles.

C	O	H	Ca	Mg	Al
12.9	44.2	0.5	41.6	0.6	0.2

6.2.2 Sample preparation

Prior to mixing, PP and CaCO₃ were dried in an oven at 120 °C for an hour and then cooled to room temperature and kept in a desiccator. Compounding was carried out at 180 °C with a rotor speed of 60 rpm in a batch mixer (Haake 40 System). The content of CaCO₃ nanoparticles in PP matrix was 9.2 vol%.

The samples used in this study were injection-molded. For comparison, neat PP sample was also prepared. The detailed description of the sample preparation using injection-molding process has been documented [30]. Izod impact bars with dimensions of 64 mm × 12.7 mm × 3.2 mm were notched with a notch cutter (250 μm tip radius) to a notch depth of 3 mm, in accordance to ASTM D-256. The double notch four-point bending (DN-4PB) specimens were first notched with a 250 μm radius notch cutter to a depth of 3 mm, followed by tapping two nearly identical sharp cracks ahead of the two notches using a liquid nitrogen-chilled razor blade. Notched Izod impact test and DN-4PB Charpy impact test were conducted at room temperature on a pendulum impact tester (Model TMI-43-02) with a single-head striker and a double-head striker, respectively.

6.2.3 Microscopy and toughening mechanism investigation

Optical microscopy (OM) and transmission electron microscopy (TEM) were employed to observe the morphology and to determine the fracture mechanisms of the nanocomposite specimens after the impact tests. The impact damage zones were cut along the crack propagation direction but perpendicular to the plane of fracture surface using a diamond saw. The plane-strain core regions of the damage zone were prepared for OM and TEM observations (Fig. 6.1). For OM investigations, the damage zones of the impact specimens were polished into thin sections with thicknesses of about 40 - 80 μm , following the procedures described by Holik *et al.* [120]. These thin sections were investigated using an Olympus BX60 optical microscope, under both bright field and cross-polarization conditions, to observe the overall damage zone and features.

For the TEM effort (JEOL JEM1200EX), the plane strain region of the damage zone was isolated and embedded in an epoxy mount and cured at room temperature to avoid thermally induced stress on the sample. The cured epoxy block was carefully trimmed to a size of 0.3 mm \times 0.3 mm and then faced off using a diamond knife prior to staining. The face-off block were then stained with ruthenium tetroxide (RuO_4) and cut into thin sections using a Richard Chung Ultracut[®] microtome. Staining with RuO_4 was necessary to allow for better image contrast between CaCO_3 particles and the PP matrix. The staining of RuO_4 also helped harden the PP matrix and fill in the voids inside the craze bands, which stabilize the integrity of craze structure during microtoming. In this study, thin-sections of about 90 nm in thickness were prepared and placed on 100-mesh Formvar/carbon-coated copper grids for TEM observation.

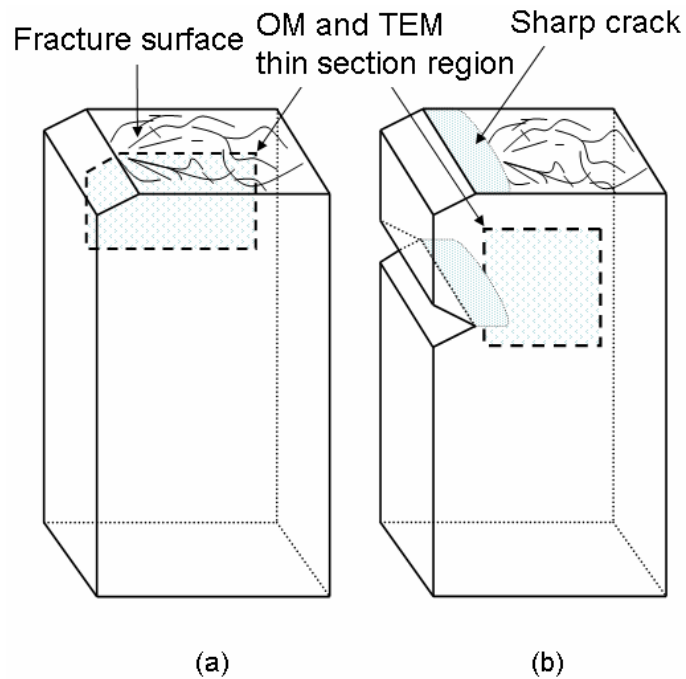


Fig. 6.1 Schematic of the impact specimens used for OM and TEM observation: (a) notched Izod impact specimen and (b) DN-4PB Charpy impact specimen.

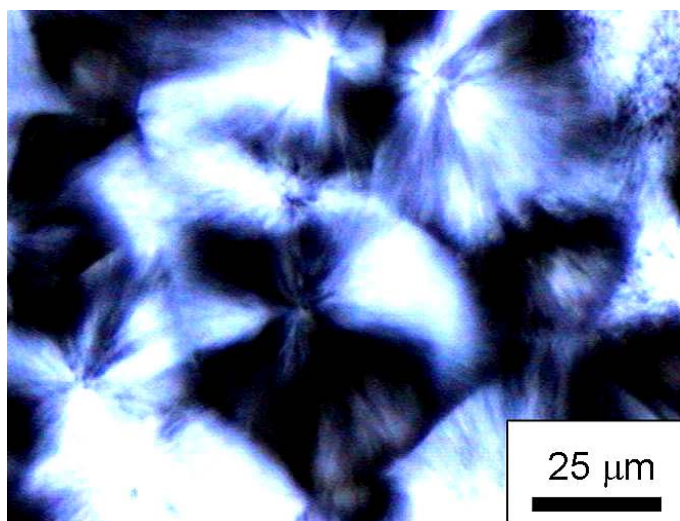
6.3 Results and Discussion

The incorporation of CaCO_3 nanoparticles in PP matrix can greatly affect the morphology of the PP matrix, which may influence the ductility and toughenability of PP. As shown in Fig. 6.2, the sizes of spherulites ($< 30 \mu\text{m}$) found in the PP/ CaCO_3 nanocomposite are much smaller than those found in neat PP ($> 50\mu\text{m}$). This suggests that CaCO_3 nanoparticles are effective nucleating agents for PP [30]. A decrease in spherulite size should positively contribute to the toughenability of semi-crystalline polymers [121,122]. In a previous work by Chan *et al.* [30], their differential scanning

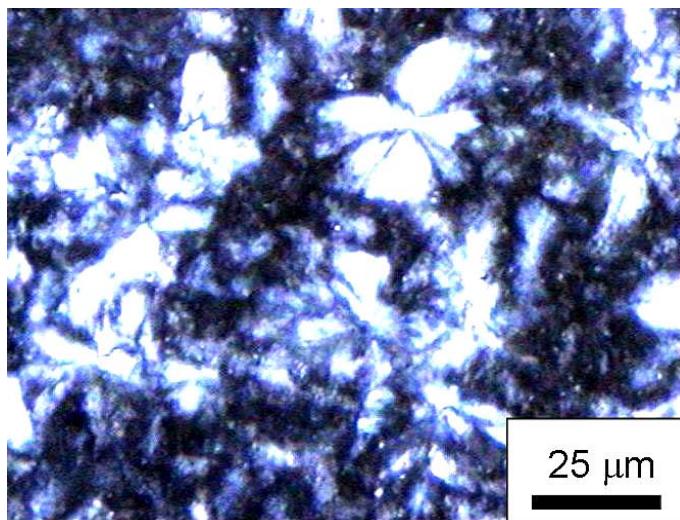
calorimetry (DSC) results indicated the presence of a small amount of β -phase PP after the addition of CaCO_3 nanoparticles. Labour *et al.* [123] found that, since the β -phase has a less crystal density than that of the α phase, the β -phase PP exhibits a lower modulus by about 10 % and a reduced hardness by 15%, respectively, than the α phase PP. The presence of the β -phase crystal around the CaCO_3 particles in PP may greatly affect the operative toughening mechanisms in the PP/ CaCO_3 nanocomposite, as well.

6.3.1 Study of Fracture process based on the DN-4PB Charpy impact specimens

The DN-4PB Charpy impact test was employed to investigate the detailed toughening mechanism in the PP/ CaCO_3 nanocomposite. The DN-4PB technique is one of the most effective ways of generating a subcritical crack tip damage zone [58-60]. The key toughening mechanism(s) and the sequence of toughening events can be unambiguously identified in the arrested crack tip damage zone region using a variety of microscopy techniques.



(a)

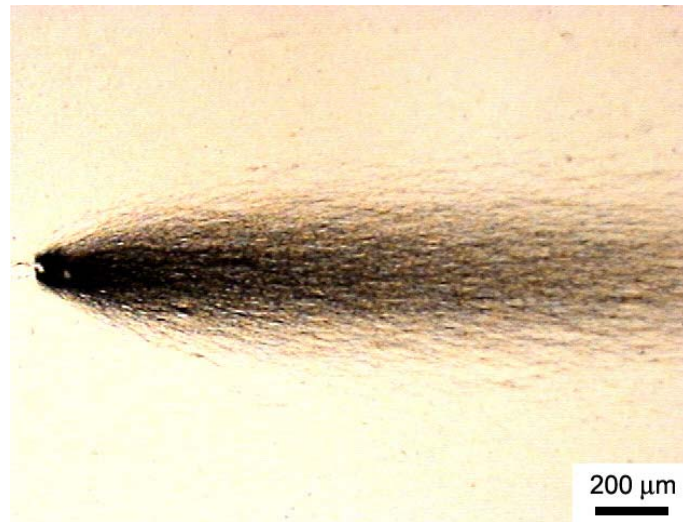


(b)

Fig. 6.2 TOM under cross-polarized field: (a) neat PP and (b) PP/CaCO₃ nanocomposite.

When OM is conducted, massive crazing (Fig. 6.3(a)) and birefringent plastic deformation (Fig. 6.3(b)) around the arrested crack tip are observed. The intensive plastic deformation is evidenced by the presence of a birefringent zone encapsulated by a larger light scattering cavitation zone, indicating that shear yielding mechanism occurs along the crack wake. These damage features are similar to the damage features observed in other toughened polymers [58-62], suggesting that massive crazing is effective in facilitating plastic deformation of PP matrix. TEM study is further employed to confirm the above conjecture.

To learn about the early stages of the toughening process, it is necessary to investigate the damage feature far away from the crack tip, but inside the damage zone. TEM observation at about 120 μm above the crack tip region has been made and found the presence of small, but widespread crazes (Fig. 6.4(a)). Interestingly, these crazes appear to be initiated by the CaCO_3 nanoparticles. This indicates that the CaCO_3 nanoparticles act as effective stress concentrators, which help trigger craze formation and growth. However, based on the TEM finding, it is unclear whether or not CaCO_3 nanoparticles have debonded from the PP matrix to allow for craze growth. It is possible that since the specimen being analyzed has been unloaded, any prior debonding process during loading would have been recovered from the snap-back of the PP matrix upon unloading, especially when the scale of plastic deformation is small, i.e. away from the crack tip region.



(a)



(b)

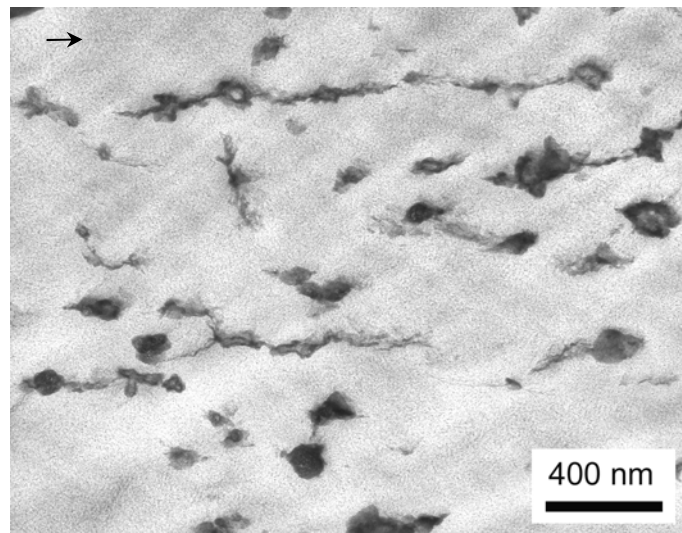
Fig. 6.3 TOM of DN-4PB Charpy impact damage zone of PP/CaCO₃ nanocomposite: (a) bright field and (b) cross-polarized field. The crack propagates from left to right.

In the region at the transition between the light-scattering craze zone and the birefringent shear banding zone, the crazes appear to be more diffuse and slightly distorted (Fig. 6.4(b)). This finding is consistent with our earlier observation on the toughening mechanisms found in nylon 6,6/polyphenylene ether and PP/Noryl systems [59,60]. However, no sign of CaCO₃ nanoparticles debonding is observed in this region, either.

To check whether or not possible debonding of CaCO₃ nanoparticles from the PP matrix has taken place, TEM micrographs were taken immediately below the fracture surface near the crack tip (Fig. 6.4(c)). The crazes were further smeared by the shear banding process, making the crazes even more defused and less well-defined. Careful observation reveals that some of the CaCO₃ nanoparticles have debonded from the PP matrix (See arrows in Fig. 6.4(c)). This finding is consistent with the recent work of Chan *et al.*, who have shown that CaCO₃ nanoparticles can be easily debonded from the PP matrix upon tensile loading [30]. For reference, the morphology of the intact, undeformed PP/CaCO₃ is shown in Fig. 6.4(d).

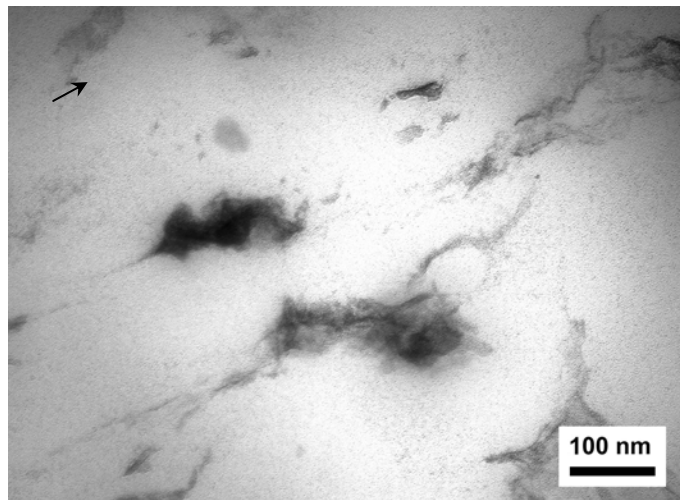
Fig. 6.5 summarizes the operative toughening mechanisms found in PP/CaCO₃ nanocomposite based on the above microscopy study. The CaCO₃ nanoparticles appear to be effective stress concentrators to help initiate and grow massive crazes. Therefore, the cavitation process, which is a prerequisite process for promoting shear banding mechanism in the plane strain region [61-64], is triggered by massive crazing at the crack tip region.

It should be noted that judging from the fact that the crazes are initiated near the equatorial region of the CaCO_3 nanoparticles and/or their small aggregates, particle-matrix debonding and/or splitting of aggregated nanoparticles should have taken place before the formation of crazes. This is simply because the maximum stress concentration site around an inclusion is located at the equatorial region if the inclusion phase is softer than the matrix phase. Since the CaCO_3 nanoparticles are much harder than the PP matrix, the CaCO_3 nanoparticles should have been debonded and/or split between the aggregated particles before the crazes were initiated.

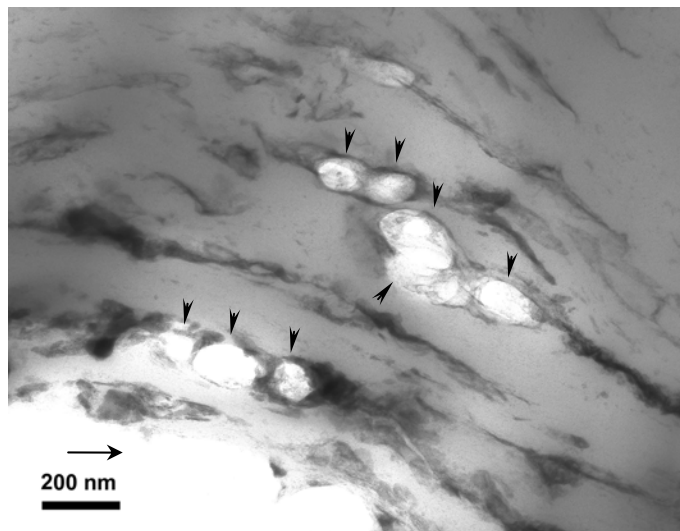


(a)

Fig. 6.4 TEM of DN-4PB Charpy impact-tested PP/ CaCO_3 specimen taken from: (a) 120 μm above the crack surface, (b) 60 μm above the crack surface, (c) immediately above the crack surface and (d) undamaged region. The arrow indicates the crack propagation direction.

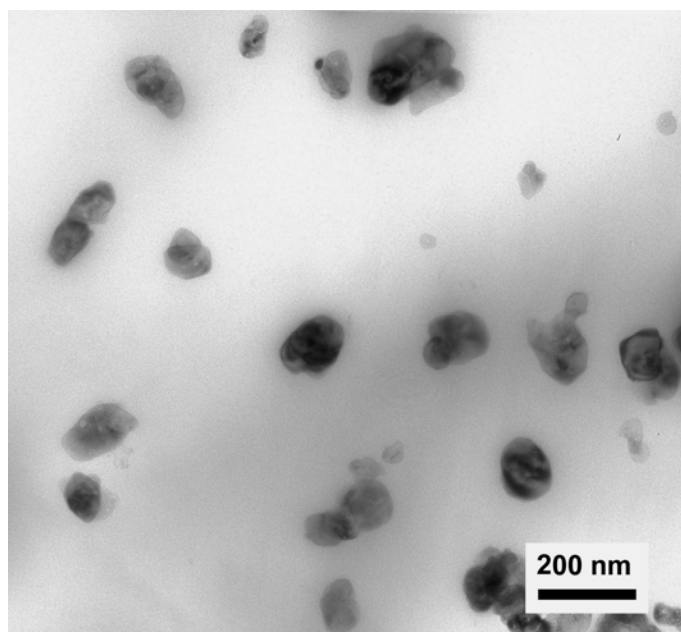


(b)



(c)

Fig. 6.4 Continued.



(d)

Fig. 6.4 Continued.

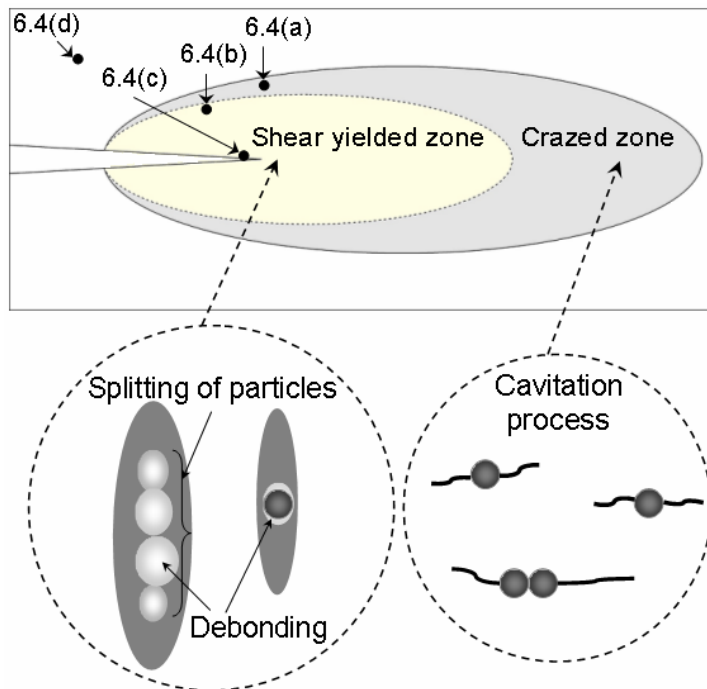


Fig. 6.5 Schematic of the deformation mechanism in the DN-4PB Charpy impact-tested PP/CaCO₃ specimen. The regions of the TEM taken in Fig. 6.4 are marked.

6.3.2 Study of fracture process based on the Izod impact specimens

The incorporation of CaCO₃ in PP has significantly increased the Izod impact strength of the PP matrix (Table 6.2). As shown in Fig. 6.6, neat PP, under bright field OM, exhibits brittle and featureless failure without any sign of significant plastic deformation. On the other hand, the PP/CaCO₃ nanocomposite exhibits extensive microcracking and/or crazing on the subsurface damage zone (Fig. 6.7). This behavior results in a higher impact strength for PP/CaCO₃ nanocomposite.

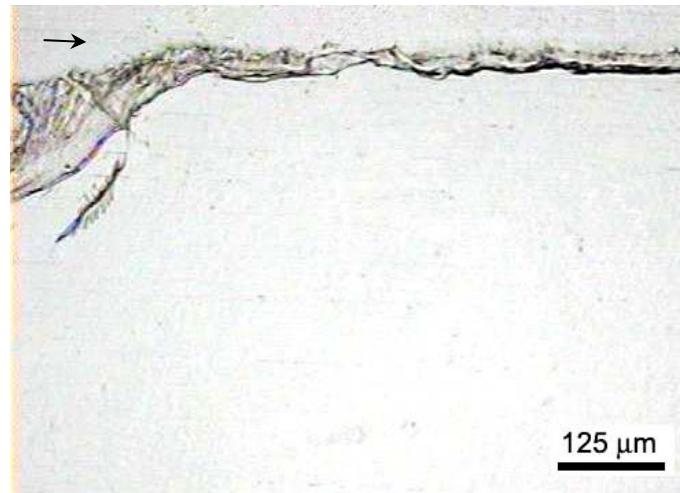
Unfortunately, the specimens after the Izod impact tests do not preserve information regarding the sequence of toughening events upon impact fracture. The advancing crack during the impact test has obliterated the operative fracture mechanisms along the crack tip and crack wake. No useful information can be extracted from further microscopy investigation using TEM. Comparison of results obtained between the DN-4PB Charpy impact tests and the Izod impact tests clearly indicates the usefulness of the DN-4PB Charpy impact tests for deciphering the impact toughening sequence of events of polymeric materials. Therefore, the DN-4PB impact test is recommended for identification and fundamental understanding of toughening mechanisms of polymers upon impact fracture.

Table 6.2

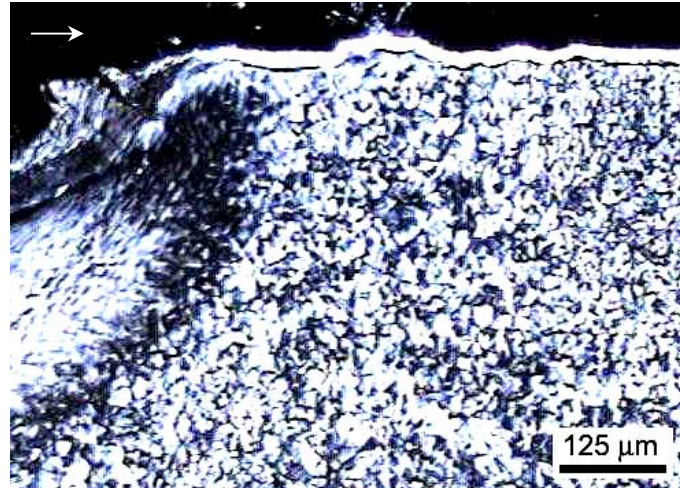
Impact strengths of the PP and PP/CaCO₃ nanocomposites.

Sample	Impact strength (J/m)
Neat PP	55.2±2.0
PP/CaCO ₃ *	128.6±9.9

* 9.2 vol% of CaCO₃ nanoparticle with mixing time of 30 min.

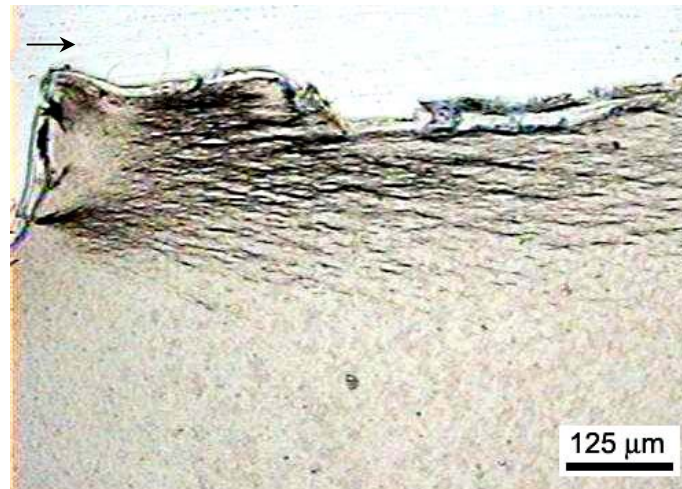


(a)

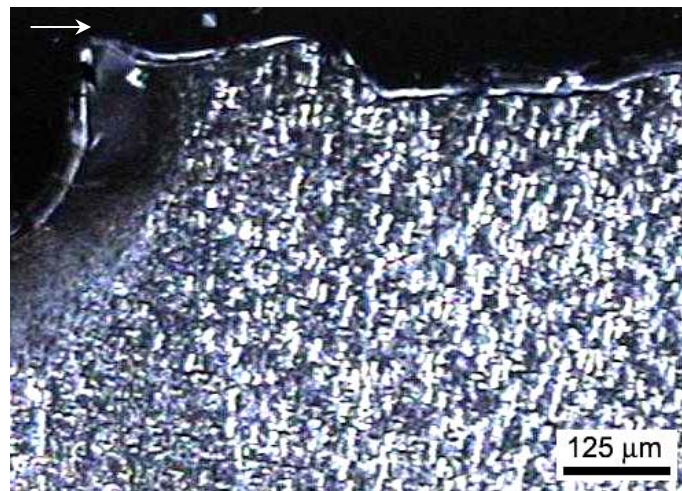


(b)

Fig. 6.6 TOM of neat PP: (a) bright field and (b) cross-polarized field. The arrow indicates the crack propagation direction.



(a)



(b)

Fig. 6.7 TOM of PP/CaCO₃ nanocomposite: (a) bright field and (b) cross-polarized field. The arrow indicates the crack propagation direction.

The present study shows that debonding and splitting of the aggregated CaCO_3 nanoparticles, which lead to massive crazing in PP, have helped trigger crack tip shear banding of PP matrix. The impact strength of PP is thus significantly improved. The present study also suggests that it is possible to use nanometer-sized rigid filler to toughen PP matrix and in the meantime increase the modulus of PP. Although the CaCO_3 nanoparticles do not appear to exhibit strong adhesion to PP matrix, the thermally-induced contraction of PP against the CaCO_3 nanoparticles upon cooling during molding of specimens produces sufficiently strong interfacial adhesion to prevent premature debonding between PP and the CaCO_3 nanoparticles. Thus, CaCO_3 nanoparticles turn out to be effective for improving both modulus and impact strength of PP.

It is noted that CaCO_3 particles are quite effective in initiating crazes in this study (Fig. 6.4(a)). Even for particles as small as 40-50 nm in size, signs of craze formation around those small particles are still present. This finding is in direct contradiction to many of the rubber [63-64] and rigid polymer [61] toughened PP systems we have investigated in the past, where only particles of a size of 300 nm or higher would show effectiveness in initiating crazes. One possible explanation to account for the discrepancy is that the CaCO_3 particles have helped to nucleate the formation of β -phase PP around the CaCO_3 particles, making it much easier to trigger the formation of crazes. Another possibility is that, during loading, the voids formed by debonding from the CaCO_3 particles grow to a significant size to allow for crazes to initiate and grow. The above conjectures, though plausible, still await further verification.

6.4 Summary

The morphology and impact toughening mechanisms in PP/CaCO₃ nanocomposite were investigated using OM and TEM techniques. It is clearly observed that the addition of CaCO₃ nanoparticles positively altered the spherulite size, crystal structure and toughenability in PP matrix. In this study, the main toughening mechanisms of the PP/CaCO₃ nanocomposite are massive crazing, followed by shear banding of the matrix. This leads to impressive improvements in both impact strength and modulus of PP matrix.

CHAPTER VII

CONCLUSIONS AND RECOMMENDATIONS

The roles of nanofiller structure on morphological characterizations and mechanical behaviors of thermoplastic nanocomposites have been studied in this dissertation. Various experimental techniques have been utilized to account for the evolution of morphology within semicrystalline nanocomposites. These techniques include optical microscopy (OM), small-angle X-ray scattering (SAXS), wide-angle X-ray scattering (WAXS), differential scanning calorimetry (DSC) and transmission electron microscopy (TEM). Several mechanical tests and the micromechanics-based models have also been performed to investigate the effect of the nanofiller structural parameters on the property enhancement of the nanocomposites.

7.1 Morphological Characterizations of the Nylon-6 Nanocomposites

At spherulitical scale, the incorporation of the well-dispersed nanoclays to the nylon-6 matrix reduces the chain mobility and the spherulite size of nylon-6, leading lower crystallinity in the nanocomposites: at lamellar scale, the exfoliated nanocomposites exhibit that the global orientation of clay layers, arising from extrusion-injection molding and simple shear process, dictates the orientation of crystalline lamellae. One of key observations is that the annealed reference nanocomposite shows

that the crystalline lamellae are oriented preferentially along $\sim 41^\circ$ counter-clockwise away from the clay orientation direction, which is confirmed by transmission electron microscopy (TEM) observations. A reduction in clay aspect ratio helps to form another weak preferred lamellar orientation, which is almost perpendicular to the clay layers. In addition, a misalignment in clay orientation strongly led to a more randomized-lamellar orientation: at crystallographic scale, wide-angle X-ray diffraction (WAXD) and differential scanning calorimetry (DSC) results reveal that the addition of nanoclay hinders chain mobility and promotes, therefore, the formation of γ -form. A decrease in clay aspect ratio and orientation leads to an increase the level of α -form by help of annealing. It is found that a large-scale simple shear process is an effective means to tailor the nanoscale structures within nylon-6 matrix. Based on the morphological parameters obtained from above observations, the possible molecular mechanisms leading to the final morphology of the nylon-6/clay nanocomposite are also discussed.

7.2 Effect of Clay Aspect Ratio and Orientation on Mechanical Behaviors of the Nylon-6 Nanocomposites

The mechanical properties of nylon-6/clay nanocomposites with variations in clay aspect ratio and orientation are studied. A large-scale simple shear process is utilized to alter the clay aspect ratio and orientation within the reference nanocomposite. It is found that the modulus, strength, and heat distortion temperature of the nanocomposites decrease as the clay aspect ratio and degree of orientation are reduced. Furthermore, the reduction of clay aspect ratio and orientation leads to an increase in

fracture toughness and ductility. The Halpin-Tsai and Mori-Tanaka micromechanics-based models are implemented to gain a better understanding with regard to the dependence of clay structural parameters, i.e. aspect ratio and orientation, on the reinforcement effect of the nanofillers. The micromechanical models can accurately describe the relationship between clay structural parameters and the corresponding moduli for exfoliated nanocomposites.

7.3 Impact Toughening Mechanisms in the PP/CaCO₃ Nanocomposite

The impact fracture mechanisms of polypropylene (PP) containing 9.2 vol% of calcium carbonate (CaCO₃) nanoparticles are investigated using optical microscopy and transmission electron microscopy. The incorporation of CaCO₃ nanoparticles reduces the size of spherulites and induces the formation of β -phase crystallites, which leads to a more ductile PP matrix. Double-notch four-point bending (DN-4PB) Charpy impact specimens and notched Izod impact specimens were utilized to study the fracture mechanism(s) responsible for the observed toughening effect. A detailed investigation reveals that the CaCO₃ nanoparticles act as stress concentrators to initiate massive crazes, followed by shear banding in PP matrix. These toughening mechanisms are responsible for the observed improved impact strength. A comparison of the fracture mechanisms observed between DN-4PB Charpy and Izod impact tests is also made to show the effectiveness of DN-4PB for investigation of impact fracture mechanisms of polymeric systems.

7.4 Recommendations for Future Work

The roles of nanofiller structure on morphological features and mechanical properties of polymer nanocomposites have comprehensively been investigated in this dissertation. More research efforts are still needed to further understand the complex nanofiller structure effect and to gain a more fundamental understanding of polymer nanocomposites. Some suggestions for further study are presented as follows;

7.4.1 Effect of nanofiller orientation and aspect ratio on property enhancement

Variations of nanofiller structural parameter have an effect on morphological characterizations and mechanical properties of polymer nanocomposites. Semicrystalline nanocomposites with unidirectional reinforcement and high aspect ratios show exceptional modulus improvement in the direction of orientation. However, it is still not clear which factors, nanofiller aspect ratio and orientation, strongly influence the mechanical properties. It is nontrivial to achieve a variety of conditioned specimens with different aspect ratio and orientation of nanofiller. Based on this dissertation work, a large-scale simple process is recommended as an available tool for tailoring the nanofiller aspect ratio and orientation *via* schemed processing scenarios. It is found that the A1-ECAE process only reduces the nanofiller aspect ratio, while the C2-ECAE route alters not only the nanofiller aspect ratio but also the nanofiller orientation [91,104].

7.4.2 Effect of dispersion of layer-structured nanofiller on reinforcement efficiency

In an earlier work by Sheng and Boyce [55], in order to explain the geometric natures of intercalated clay they proposed the effective nanoparticle concept, which consists of the clay layers and clay inter-layer galleries. In other words, effective clay structures were defined as the number of platelet per stacked clay (n) and the platelet inter-layer spacing (d_{001}) and were used to evaluate the mechanical property enhancement using the continuum-based micromechanical models: a increase in reinforcement efficiency related to decreasing the number of platelet a stack resulted from increase in effective clay aspect ratio and modulus, whereas a increase in reinforcement efficiency associated with to increasing inter-layer spacing resulted from increase in effective clay volume fraction. It was found that the fully exfoliated nanocomposite ($n=1$) did not show a significant increase in reinforcement efficiency. Furthermore, in order to evaluate exact reinforcement efficiency of exfoliated nanocomposites, the appearance of exfoliated nanoclay should be considered since its effect on modulus improvement is also strong. In particular, TEM micrographs show that exfoliated clay layer is much slightly curved shape than that of intercalated layers [91,104]. Those curvatures of clay layers may negatively have an effect on modulus of polymer nanocomposites. Therefore, it may not be necessary for an increase in modulus of polymer nanocomposites to achieve a nearly perfect exfoliation and dispersion of layer-structured nanofiller into a polymer matrix, when especially considering its processing difficulties and efforts. Instead, the optimal condition regarding modulus

enhancement could be determined by compromising effective filler structural parameters (n , d_{001} and the curvatures of layer) *via* numerical simulations.

7.4.3 Fabrication of desirable properties in terms of modulus and toughness in nanocomposites

In present research, the PP/CaCO₃ nanocomposite has shown an attractive way to improve both modulus and toughness, as well as damping property due to effective roles of CaCO₃ nanoparticles in toughenability of PP matrix. On the other hand, the nylon-6/clay nanocomposites exhibited significant improvement in modulus, while little loss in fracture toughness. Tzika *et al.* [124] found the elastic constants of transcrystallized nylon-6 induced by inclusion of rubber particles: the longitudinal modulus of transcrystalline nylon-6 ($E_{11,tc}$) improved by ~30% compared to neat nylon-6. Based on those results, they performed a FEM simulation of nylon-6/clay nanocomposites with three phases, i.e. clay, isotropic matrix and transcrystallized anisotropic matrix. The results showed that the contribution of orientation of polymer crystalline to the reinforcement of nanocomposites was minor compared to modulus enhancement by nanofillers, implying that the clay particle is still a dominant reinforcing phase. In the other hand, the effect of crystalline orientation on fracture toughness in PET was investigated [75,76]. Weon *et al.* [76] found that the molecular chain orientation significantly affected the fracture toughness of PMMA. The highest fracture toughness (K_{IC}) was found when the crack propagated perpendicular to the crystalline and molecular orientation direction. This suggests that an increase in fracture toughness of

polymer nanocomposites can be achieved by altering its fibrillar and molecular orientation. This result may be applied to the nanocomposite technology to improve the fracture toughness of polymer nanocomposite [34,124]. Consequently, the addition of nanofillers to polymer matrix leads to an increase in modulus, while a proper alteration of crystalline orientation results in an improvement in fracture toughness of polymer nanocomposites, which can also be achieved by a large-scale simple shear process.

REFERENCES

- [1] Kojima Y, Usuki A, Kawasumi M, Okada O, Fukushima Y, Kurachi T, Kamigaito O. *J Mater Res* 1993;8:1185.
- [2] Sue HJ, Gam KT, Bestaoui N, Spurr N, Clearfield A. *Chem Mater* 2004;16:242.
- [3] Liu L, Qi Z, Zhu X. *J Appl Polym Sci* 1999;71:1133.
- [4] Usuki A, Koiwai A, Kojima Y, Kawasumi M, Okada A, Kurauchi T, Kamigaito O. *J Appl Polym Sci* 1995;55:119.
- [5] Lan T, Pinnavaia TJ. *Chem Mater* 1994;6:2216.
- [6] Wang Z, Pinnavaia TJ. *Chem Mater* 1998;10:3769.
- [7] Vaia RA, Giannelis EP. *Macromolecules* 1997;30:7990.
- [8] Dennis HR, Hunter DL, Chang D, Kim S, White JL, Cho JW, Paul DR. *Polymer* 2001;42:9513.
- [9] Zheng W, Wong SC, Sue HJ. *Polymer* 2002;43:6767.
- [10] Park JH, Jana SC., *Polymer* 2003;44:2091.
- [11] Silva A, Rocha M, Moraes M, Valente C, Coutinho F. *Polym. Testing* 2000;21:57.
- [12] Kim GM, Lee DH, Hoffmann B, Kressler J, Stöppelmann G. *Polymer* 2000;42:1095.
- [13] Wang Y, Zhang L, Tang C, Yu D. *J Appl Polym Sci* 2000;78:1878.
- [14] Fu X, Qutubuddin S. *Polymer* 2001;42:807.
- [15] Mencil J, Varga J. *J Therm Anal* 1983;28:161.
- [16] Alexandre M, Dubois P. *Mater Sci Engng* 2000;28:1.
- [17] Kurian T, De PP, Tripathy DK, De SK, Peiffer DG. *J Appl Polym Sci* 1996;62:1729.
- [18] Laus M, Francescangeli O, Sandrolini F. *J Mater Res* 1997;12:3134.

- [19] Favier V, Canova GR, Shrivastava SC, Cavaille JY. *Polym Engng Sci* 1997;37:1731.
- [20] Chazeau L, Cavaille JY, Canova G, Dendievel R, Bouterin B. *J Appl Polym Sci* 1999;71:1797.
- [21] Herron N, Thorn DL. *Adv Mater* 1998;10:1173.
- [22] Messersmith PB, Giannelis EP. *J Polym Sci Part A: Polym Chem* 1995;33:1047.
- [23] Akelah A, Moet A. *J Mater Sci* 1996;31:3589.
- [24] Kojima Y, Usuki A, Kawasumi M, Okada A, Kurachi T, Kamigaito O. *J Appl Polym Sci* 1993;49:1259.
- [25] Yano K, Usuki A, Okada A, Kurauchi T, Kamigaito O. *J Polym Sci Part A: Polym Chem* 1993;31:2493.
- [26] Gilman JW. *Appl Clay Sci* 1999;15:31.
- [27] Vaia R A, Price G, Ruth PN, Nguyen HT, Lichtenhan J *Appl Clay Sci* 1999;15:67.
- [28] Lincoln DM, Vaia RA, Sanders JH, Phillips SD, Cutler JN, Cerbus CA. *Polym Mater Sci Eng* 2000;82: 230.
- [29] Huang JC, Zhu Zk, Yin J, Qian XF, Sun YY. *Polymer* 2001;42(3):873.
- [30] Chan CM, Wu J, Li JX, Cheung YK. *Polymer* 2002;43:2981.
- [31] Hoffmann H, Grellmann W, Zilvar V. *Polymer composites*, New York: Walter de Gruyter; 1986.
- [32] Badran BM, Galeski A, Kryszewski M. *J Appl Polym Sci* 1982;27:3669.
- [33] Liu ZH, Kwok KW, Li RKY, Choy CL. *Polymer* 2002;43:2501.
- [34] Thio YS, Argon AS, Cohen RE, Weinberg M. *Polymer* 2002;43:3661.
- [35] Shepherd PD, Golemba FJ, Maine FW. *Adv Chem Ser* 1974;134:41.
- [36] Usuki A, Kojima Y, Kawasumi M, Okada A, Fukushima Y, Kurauchi T, Kamigaito O. *J Mater Res* 1993;8(5):1179.
- [37] Okada A, Fukushima Y, Kawasumi M, Inagaki S, Usuk A, Sugiyami S, Kurauchi T, Kamigaito O. *US Patent* 4739007; 1988.

- [38] Kawasumi M, Kohzaki M, Kojima Y, Okada A, Kamigaito O. US Patent 4810734; 1989.
- [39] Fornes TD. Polyamide-layered silicate nanocomposites by melt processing, PhD dissertation, the University of Texas at Austin, Dept of Chem Engng; 2003.
- [40] Fujiwara S, Sakamoto T. JP Patent JP-A-51-109998; 1976.
- [41] Usuki A, Kawasumi M, Kojima Y, Okada A, Kurauchi T, Kamigaito O. J Mater Res 1993;8(5):1174.
- [42] Adams D, Doner D. J Compos Mater 1967;1(4):152.
- [43] Eshelby JD. Proc R Soc A 1957;241:376.
- [44] Hill R. J Mech Phys Solids 1965;13:213.
- [45] Tandon GP, Weng GJ. Polym Compos 1984;5(4):327.
- [46] Hermans J. J Proc Kon Ned Akad v Wetensch B 1967;65:1.
- [47] Mori T, Tanaka K. Acta Metall Mater 1973;21:571
- [48] Ashton JE, Halpin JC, Petit PH. Primer on composite materials: analysis. Westport, CT: Technomic; 1969.
- [49] Halpin JC. J Compos Mater 1969;3:732.
- [50] Halpin JC, Kardos JL. Polym Engng Sci 1976;16:344.
- [51] Cox HL. Br. J Appl Phys 1952;3:72.
- [52] Hill R. Proc Phys Soc A 1952;65:349.
- [53] Fornes TD, Paul DR. Polymer 2003;44:4993.
- [54] Tucker CL, Liang E. Compos Sci Technol 1999;59:655.
- [55] Sheng N, Boyce MC, Parks DM, Rutledge GC, Abes JI, Cohen RE. Polymer 2003;44:4993.
- [56] Rice JR. J Appl Mech 1968;35:379.
- [57] Rice JR. Fracture 1968;2:191.
- [58] Sue HJ, Yee AF. J Mater Sci 1993;28:2915.

- [59] Sue HJ, Yee AF. *J Mater Sci* 1989;24:1447.
- [60] Sue HJ. *Polym Eng Sci* 1991;31:270.
- [61] Wei GX, Sue HJ, Chu J, Huang C, Gong K. *J Mater Sci* 2000;35:555.
- [62] Sue HJ. *J Mater Sci* 1992;27:3098.
- [63] Wei GX, Sue HJ. *Polym Eng Sci* 2000;40:1979.
- [64] Li Y, Wei GX, Sue HJ. *J Mater Sci* 2002;37:2447.
- [65] Bucknall CB, Clayton D, Keast WE. *J Mater Sci* 1972;7:1443.
- [66] Aboulfaraj M, G'Sell C, Ulrich B, Dahoun A. *Polymer* 1995;36:731.
- [67] Sue HJ, Gam KT, Bestaoui N, Spurr N, Clearfield A, Miyamoto M, Miyatake N. *Act Mater* 2004;52:2239.
- [68] Weon JI, Gam KT, Boo WJ, Sue HJ, Chan CM. *J Appl Polym Sci*, submitted.
- [69] Creasy TS, Kang YS. *J Thermo Comp Mat* 2004;17:205.
- [70] Xia ZY. Processing-Structure-Property relationships in oriented polymers, PhD dissertation, Texas A&M University, Dept of Mech Engng; 2001.
- [71] Haouaoui M, Hartwig KT, Payzant EA. *Acta Materialia*, 2005;53(3):801.
- [72] Li CKY. Novel equal channel angular extrusion process for improving physical and mechanical properties of polymers, PhD dissertation, Texas A&M University, Dept of Mech Engng; 1999.
- [73] Li CKY, Xia ZY, Sue H-J. *Polymer* 2000;41:6285.
- [74] Xia ZY, Sue HJ, Hsieh AJ. *J Appl Polym Sci* 2001;79:2060.
- [75] Xia ZY, Sue HJ, Rieker TP. *Macromol* 2000;33:8746.
- [76] Weon JI, Creasy TS, Sue HJ, Hsieh A. *J Polym Eng Sci* 2005;45:314.
- [77] Kohan MI. *Nylon plastics handbook*, Cincinnati, OH: Hanser/Gardner Publications Inc.; 1995.
- [78] Babatope B, Isaac DH. *Polymer* 1992;33:1664.
- [79] Fouda IM, Oraby AH. *Polymer testing* 1999;18:235.

- [80] Murthy N, Bray R, Correale S, Moore R. *Polymer* 1995;36:3863.
- [81] Liu X, Wu Q. *Polymer* 2002;43:1933.
- [82] Illers KH. *Makromol Chem* 1978;179:497.
- [83] McNeil LE, Grimsditch M. *J Phys Condensed Matter* 1993;5:1681.
- [84] Mark JE. *Physical properties of polymers handbook*, Woodbury, NY: AIP Press; 1996.
- [85] Lincoln DM, Vaia RA, Wang ZG, Hsiao BS. *Polymer* 2001;42:1621.
- [86] Kojima Y, Usuki A, Kawasumi M, Okada A, Kurauchi T, Kamigaito O, Kaji K. *J Polym Sci Part B: Polym Phys* 1993;33:1039.
- [87] Weber G, Kuntze D, Stix W. *Colloid polym Sci* 1982;260:956.
- [88] Belta-Calleja FJ, Vonk GG. *X-ray scattering of synthetic polymers*, New York: Elsevier Science; 1989.
- [89] Verma R, Marand H, Hsiao BS. *Macromol* 1996;29:7767.
- [90] Fornes TD, Yoon PJ, Keskkula H, Paul DR. *Polymer* 2001;42:9929.
- [91] Weon JI, Sue HJ. *Polymer*, submitted.
- [92] Nam PH, Maiti P, Okamoto M, Kotaka T, Hasegawa N, Usuki A. *Polymer* 2001;42:9633.
- [93] Lee DC, Jang LW. *J Appl Polym Sci* 1996;61:1117.
- [94] Lee DC, Jang LW. *J Appl Polym Sci* 1998;68:1997.
- [95] Vaia RA, Ishii H, Giannelis EP. *Chem Mater* 1993;5:1694.
- [96] Christiani BR, Maxfield M. US Patent 5747560; 1998.
- [97] Gregar KC, Winans RE, Botto RE. US Patent 5308808; 1994.
- [98] Carrado KA, Xu L. *Chem Mater* 1998;10:1440.
- [99] Weimer MW, Chen H, Giannelis EP, Sogah DY. *J Am Chem Soc* 1999;121(7):1615.

- [100] Yano K, Usuki A, Okada A. *J Polym Sci, Part A: Polym Chem* 1997;35(11):2289.
- [101] Delozier DM, Orwoll RA, Cahoon JF, Johnston NJ, Smith JG, Connell JW. *Polymer* 2001;43(3):813.
- [102] Wang Z, Pinnavaia TJ. *Chem Mater* 1998;10(7):1820.
- [103] Fornes TD, Yoon PJ, Keskkula H, Paul DR. *Polymer* 2001;42:9929.
- [104] Weon JI, Xia ZY, Sue HJ. *J Polym Sci, Part B: Polym Phys*, submitted.
- [105] Williams LE. *Fracture of mechanics of polymer*, New York: Wiley; 1984.
- [106] Takemori M. *SPE ANTEC* 1978;24:216.
- [107] van Es M, Xiqiao F, van Turnhout J, van der Giessen E. In: Al-Malaika S, Golovoy AW, Wilkie CA, editors, *Specialty polymer additives: principles and applications*, Malden, MA: Blackwell Science; 2001 (chapter 21).
- [108] Hull D, Clyne TW. *An introduction to composite materials*, 2nd ed. New York: Cambridge University Press; 1996.
- [109] Manevitch OL, Rutledge GC. *J Phys Chem B* 2003;108:1428.
- [110] Tyan HL, Liu YC, Wei KH. *Chem Mater* 1999;11:1942.
- [111] Hasegawa N, Okamoto H, Kawasumi M, Usuki A. *J Appl Polym Sci* 1999;74:3359.
- [112] Gam KT, Miyamoto M, Nishimura R, Sue HJ. *Polym Engr & Sci* 2003;43:1635.
- [113] Pinnavaia TJ, Lan T, Kaviratna PD, Wang MS. *Mat Res Soc Symp Proc* 1994;346:81.
- [114] Hasegawa N, Kawasumi M, Kato M, Usuki A, Okada A. *J Appl Polym Sci* 1998;67:87.
- [115] Kawasumi M, Hasegawa N, Kato M, Usuki A, Okada A. *Macromolecules* 1997;30:6333.
- [116] Kurokawa Y, Yasuda H, Kashiwagi M, Oyo A. *J Mat Sci Letters* 1997;16:1670.
- [117] Usuki A, Kato M, Okada A, Kurauchi T. *J Appl Polym Sci* 1997;63:137.
- [118] Kato M, Usuki A, Okada A. *J Appl Polym Sci* 1997;66:1781.

- [119] Kurokawa Y, Yasuda H, Oya A. *J Mater Sci Letters* 1996;15:1481.
- [120] Holik AS, Kambour RP, Hobbs SY, Fink DG. *Microstructure Sci* 1979;7:357.
- [121] Friedrich K. *Adv Polym Sci* 1983;52/53:225.
- [122] Ouederni M, Philips PJ. *J Engng Appl Sci* 1996;2:2312.
- [123] Labour T, Ferry L, Gauthier C, Hajji P, Vigier G. *J Appl Polym Sci* 1999;74:195.
- [124] Tzika PA, Boyce MC, Parks DM. *J Mech Phys Solids* 2000;48:1893.

APPENDIX

**MECHANICAL PROPERTIES OF TALC- AND CaCO₃-
REINFORCED HIGH-CRYSTALLINITY POLYPROPYLENE
COMPOSITES**

A.1 Introduction

The main attraction of polypropylene (PP) is its high performance-to-cost ratio. PP can also be easily modified to achieve greatly enhanced properties. With regard to reinforcement effects, considerable research can be found in recent literature [1-13] on improving mechanical properties of PP using various kinds of inorganic fillers. It is now well recognized that the use of inorganic fillers is a useful tool for improving stiffness, toughness, hardness, chemical resistance, dimension stability, and gas barrier properties of PP [1-4]. The effects of inorganic fillers on the mechanical and physical properties of the PP composites strongly depend on the filler size, shape, aspect ratio, interfacial adhesion, surface characteristics and degree of dispersion [5-10]. Typically, the physical and mechanical properties of the polymers that contain nano-sized particles are superior to those containing micron-sized particles of the same filler type [11-13].

Talc and CaCO₃ are among the most commonly used fillers for PP reinforcement. CaCO₃ particles have an isotropic particulate structure, while talc has a plate-like structure [14]. In general, the introduction of inorganic fillers to PP leads to an increase

in modulus but a decrease in toughness and ductility. However, it is well known that most semicrystalline polymers can be effectively toughened by incorporation of well-dispersed secondary phase(s) in the matrix [15-19]. Blending PP with rubber particles is an attractive way to improve toughness. However, the significant drawback of rubber toughening is loss of Young's modulus and strength, which can greatly limit its engineering applications. Therefore, there is considerable interest to simultaneously improve both the stiffness and toughness of the polymer matrix. Several studies have demonstrated an increase in both stiffness and toughness of PP and high-density polyethylene (HDPE) using rigid particles [20-29].

Bartczak *et al.* [27] used calcium stearate modified- CaCO_3 particles with average diameters of 3.50, 0.70 and 0.44 μm to toughen HDPE. They found that the Izod impact toughness of HDPE could be improved from about 50 J/m to 800 J/m, depending on the size and loading of CaCO_3 utilized. Thio *et al.* [21] reported that the introduction of micrometer-scale CaCO_3 particles led to an improvement in the Izod impact strength of PP by up to four times. It was found that the main toughening mechanisms were crack deflection and interfacial debonding and plastic deformation of interparticle matrix ligaments. Recently, Chan *et al.* [11] reported that the fracture toughness, termed J_{IC} , of PP increased five-fold by incorporating nanometer-scale (ca. 40 nm) CaCO_3 particles, and the CaCO_3 nanoparticles acted as stress concentrators to promote toughening mechanisms.

This study, which is part of a larger effort to improve the stiffness and toughness of high-crystallinity PP (hcPP) systems to replace glass fiber-filled PP for engineering

applications, is to gain fundamental understanding on the mechanical behavior of hcPP/talc and hcPP/CaCO₃. It is hoped that, through this study, approaches for simultaneously improving toughness and stiffness of hcPP for structural applications can be established. A number of mechanics and microscopy techniques, such as the double-notch four-point-bending (DN-4PB) technique [23,28-33], transmission optical microscopy (TOM), transmission electron microscopy (TEM), differential scanning calorimetry (DSC) and wide-angle X-ray diffraction (WAXD), were employed to investigate the micro-plastic deformation in the hcPP composite systems. To elucidate the dependency of strain rate on the operative toughening mechanisms in hcPP, both the *J*-integral method under a quasi-static loading condition and the Izod impact test in a dynamic loading regime were carried out. Toughening mechanisms responsible for the observed toughness improvements under both quasi-static loading and dynamic loading conditions for hcPP/talc and hcPP/CaCO₃ composite systems are described. Approaches for strengthening and toughening of hcPP are also discussed.

A.2 Experimental Procedure

A.2.1 Sample preparation

In this study, the hcPP (BP Chemicals, Accpro[®] 9346), which possesses a high isotacticity and high heat resistance, has a melt flow rate of 2.16 kg at 230°C and a density of 0.906 g/cc. The two inorganic fillers chosen in this study are (1) surface-

modified talc ($\rho=2.780$ g/cc; ~ 2 μm in size; Luzenac[®] R7 talc) and (2) CaCO₃ nanoparticles ($\rho =2.660$ g/cc; ~ 44 nm in size; Guang Ping Nano Technology Group Ltd).

The hcPP resin was compounded, using twin-screw extruders, with talc (11.7 vol%) and CaCO₃ (11.9 vol%) by Luzenac North America and Hong Kong University of Science and Technology, respectively. Test specimens were injection-molded into ASTM Standard tensile and rectangular bars for mechanical testing.

A.2.2 DSC analysis

Non-isothermal crystallization behavior of the neat hcPP and hcPP composites was performed on a Perkin-Elmer Pyris-1 DSC. All tests were executed in a nitrogen atmosphere with a sample quantity of ~ 10 mg. The samples were first heated from 25 to 250 °C at a rate of 10 °C /min. Subsequently, the samples were annealed for one minute at 250°C and then cooled to 25 °C at the same rate. The melting temperature (T_m) was determined from the heating curve, while the crystallization temperature (T_c) was determined from the cooling curve.

A.2.3 X-ray characterization

WAXD experiments were performed at room temperature using a Bruker-AXS D8 powder diffractometer with a sealed X-ray source (Cu) in the standard vertical θ - 2θ geometry (40 kV and 50mA). A germanium incident beam monochromator was used to produce $K\alpha_1$ free radiation, and a Si(Li) detector was used for data collection. The

wavelength of the incident X-ray was 1.54 Å. Data were collected from 7° to 35° (2 θ) at a scanning rate of 1°/min.

A.2.4 Mechanical property measurement

For the dynamic mechanical analysis, specimens with dimensions of 42.0 mm \times 12.5 mm \times 3.5 mm were cut from injection-molded tensile bars and dried under vacuum at room temperature for 24 hrs. The tests were performed under torsional mode on a Rheometric Mechanical Spectrometer (RMS-800) through a temperature range of -140 to 180 °C. The heating chamber was purged with nitrogen gas to minimize sample degradation during the test. Auto-tension and auto-strain were applied to ensure the quality of data. Measurements were made at 5 °C intervals with 45 s of soaking time. The spectrometer was set to produce a sinusoidal wave function with the peak strain of 0.1 %. The glass transition temperature (T_g) was assigned to be the maximum $\tan \delta$ peak temperature.

Tensile properties were evaluated according to ASTM D 638. Specimens were “dog-bone” shaped and had dimensions of 63.5 mm \times 25.4 mm \times 5.2 mm in the gauge length region. The gripping regions at both ends were 12.7 mm wide. The tensile specimens parallel to the flow direction (FD), as shown in Fig. A.1, were tested using a screw-driven mechanical testing machine (Sintech II) at a constant crosshead speed of 0.085 mm/s at room temperature. An extensometer was attached to the gage length region to measure the displacement during deformation. The Young’s modulus was

calculated at 0.5 % strain and the yield stress was determined in accordance with the ASTM Standard. The average values and standard deviations were calculated after testing five specimens of each sample.

The J -integral values were obtained according to the plane strain fracture toughness standard ASTM E 813. A single-edge-notch 3-point-bend (SEN-3PB) specimen geometry was chosen for the J -integral test. The specimens had dimensions of 65.0 mm \times 12.5 mm \times 3.5 mm. According to ASTM E 813, the maximum load for pre-cracking should be limited to prevent the influence of plastic deformation in the case of a quasi-static fracture test. Under this load limit, the ratio of the initial crack length (a_i) to the specimen width (W), a_i/W , was controlled to be approximately 0.5 by tapping a liquid nitrogen-chilled razor blade to wedge open the initial crack. The crack propagation direction was parallel to the transverse direction (TD), as depicted in Fig. A.1. A screw-driven mechanical testing machine (Instron Model 1125) was used to conduct the testing at a constant crosshead speed of 0.5 mm/min at room temperature, and the multiple specimen technique was employed for the measurement. The J_{IC} values were determined at the point of intersection between the J - R curve and the blunting line, $J = 2\sigma_y\Delta a$ (where σ_y is the yield stress).

Notched Izod impact tests were conducted according to ASTM D 256 on a pendulum impact tester (Model TMI 43-02). Before the testing, the width and the depth of the specimens were measured using a micrometer. The impact strength was determined by dividing the absorbed energy by the initial cross-sectional area under the

notch. Five specimens of each sample were tested and then the average values and standard deviations were calculated and reported.

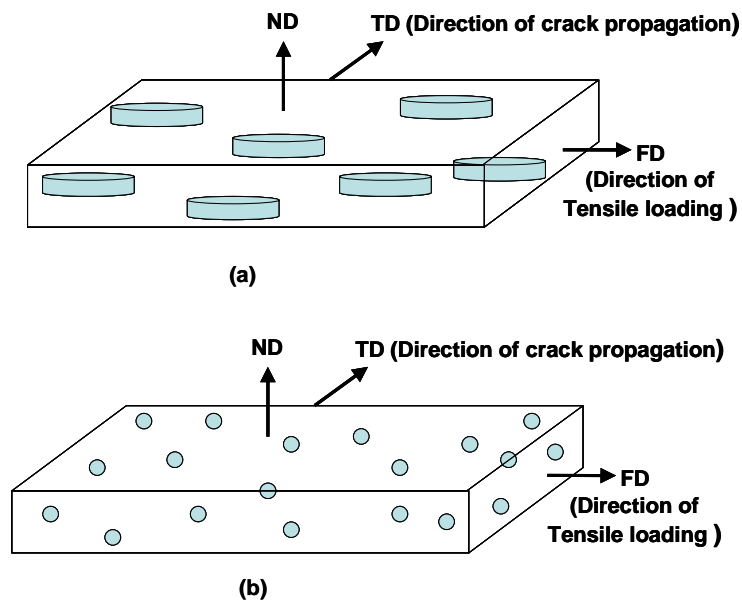


Fig. A.1 Schematic of injection molded specimens: (a) dispersed talc particles are oriented along the injection molding direction (FD) and (b) the hcPP/CaCO₃ nanocomposite.

A.2.5 Microscopy and toughening mechanism investigation

The morphology and toughening mechanisms in neat hcPP and hcPP composite systems were investigated using the DN-4PB technique [23,28-33], TOM, and TEM. The DN-4BP samples were machined into dimension of 63.5 mm × 12.7 mm × 3.5 mm.

DN-4BP bars were notched with a 250 μm radius notch cutter to a depth of 3.18 mm. The distance between two notches of DN-4BP bars was 11.2 mm. Sharp cracks were then generated by a fresh blade which had been chilled in liquid nitrogen. The details of the DN-4PB test specimen are shown in Fig. A.2. The DN-4PB tests were performed using a screw-driven mechanical testing machine (Instron Model 1125). Cross-head speeds of 0.508 and 50.8 mm/min at room temperature were applied to generate sub-critical fracture of the hcPP samples. The DN-4PB Charpy impact tests were conducted on a pendulum impact tester (Model TMI 43-02) with a modified double-head striker. The DN-4-PB damage zone of the subcritically propagated crack was cut along the crack propagation direction but perpendicular to the fracture surface using a diamond saw. The plane strain core region of the crack tip damage zone was prepared for both TOM and TEM investigations.

In the TOM investigation, the damage zones were polished into thin sections with thicknesses of ~ 40 μm . These thin sections were observed using an Olympus BX60 optical microscope under both bright field and cross-polarization conditions to observe the overall damage zone size and features.

For the TEM experiments, the plane strain core regions of the damage zone and the intact region were carefully trimmed to an appropriate size (an area of 5 mm \times 5 mm) and embedded in DGEBA epoxy/diethylenetriamine. The epoxy was cured at room temperature overnight. The cured block was further trimmed to about 0.3 mm \times 0.3 mm. The trimmed block was faced off by a diamond knife and then stained with RuO_4 . The faced-off block was exposed to the vapor of an aqueous RuO_4 solution (0.5% by weight)

for 3 h. Ultra-thin sections, ranging from 60 to 90 nm, were obtained using a Reichert-Jung Ultracut E microtome with a diamond knife at room temperature. The thin sections were placed on 200 mesh formvar-coated copper grids and examined using a Zeiss-10C transmission electron microscope at an accelerating voltage of 80 kV.

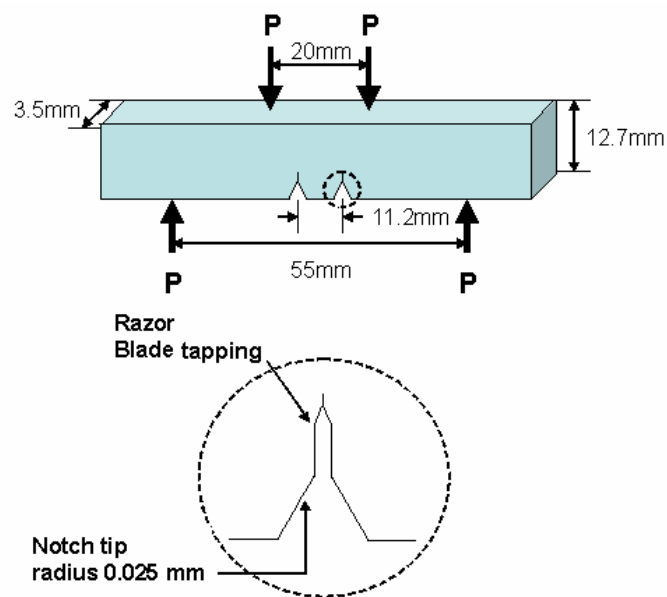


Fig. A.2 Details of the DN-4PB test specimen.

A.3 Results and Discussion

A.3.1 Dispersion in hcPP composites

Figs. A.3 and A.4 are TEM micrographs of the hcPP/talc and the hcPP/CaCO₃, respectively. It is found that the talc particles have an average aspect ratio of ~31 and are

well dispersed. In addition, the layered particles of talc are seen to be aligned along the injection-molding direction (FD), which may help contribute to good mechanical properties along the FD. On the contrary, significant amounts of aggregates are observed in the hcPP/CaCO₃ nanocomposite. Our earlier work [23] showed that a good dispersion could be obtained in the hcPP/CaCO₃ if the CaCO₃ loading is below 9.2 vol%. High CaCO₃ volume fraction may have caused the coalescence of CaCO₃ nanoparticles because of their high surface energy. The effect of the agglomeration of CaCO₃ fillers on hcPP mechanical properties will be discussed in detail later.

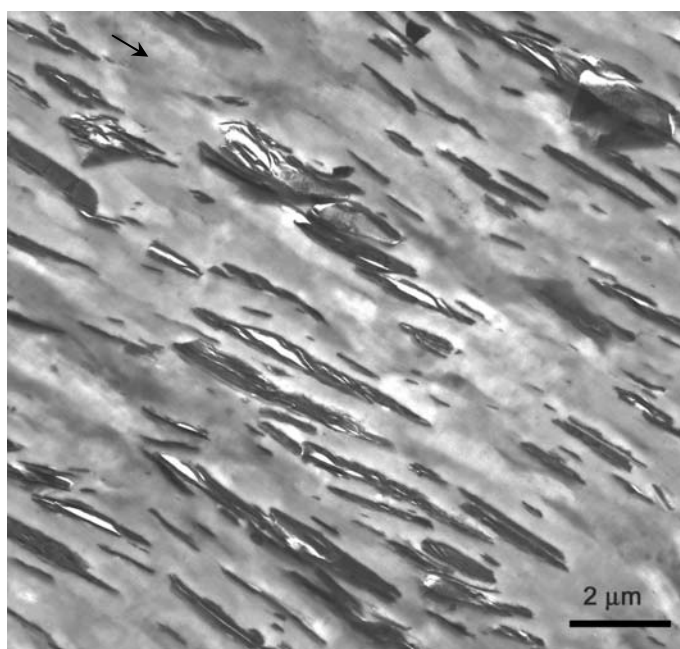


Fig. A.3 TEM micrograph of the hcPP/talc. The arrow indicates the flow direction.

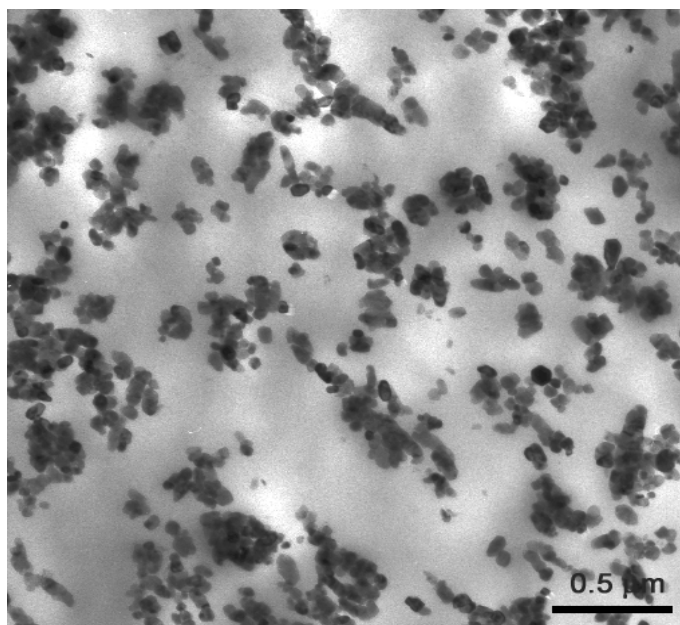


Fig. A.4 TEM micrograph of the hcPP/CaCO₃.

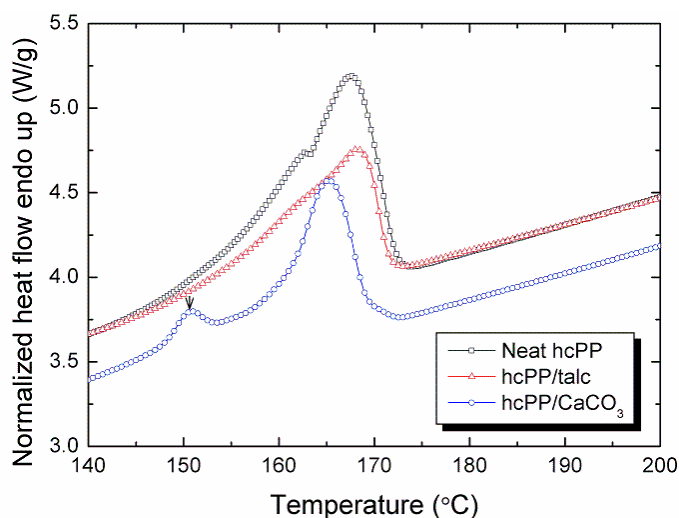
A.3.2 Crystallization of the hcPP composites

The DSC thermographs of the neat hcPP and hcPP composites are shown in Fig. A.5. The weight percentage crystallinity is calculated by integrating the area under the DSC melting endothermic peak (from 120 to 200°C) and dividing by the heat of fusion with 100% crystalline PP ($\Delta h_0 \approx 209 \text{ J/g}$) [19]. In the case of the hcPP composites, the heat of fusion needs to be normalized to the actual weight of hcPP. Table A.1 gives the summary of the DSC test results. It should be noted that the addition of talc particles to

the hcPP matrix did not have any significant effect on T_m , T_c , or crystallinity (χ_c). Whereas, when the CaCO_3 nanoparticle was dispersed in hcPP, a drop of 8°C in T_c and a slight decrease in χ_c were observed. Those findings are in direct contradiction to earlier work by Chan *et al.* [11], wherein the incorporation of the same size and type of CaCO_3 has increased T_c by 10°C for a general purpose PP. The reason for the delayed hcPP/ CaCO_3 nanocomposite crystallization might be due to an unusual interaction between hcPP and CaCO_3 nanoparticles. In general, crystallization starts at chain folds to minimize the Gibbs free energy state. However, the presence of CaCO_3 nanoparticles in hcPP, which has a much higher isotacticity index, may have restricted chain mobility thereby inducing the formation of less-stable β -phase crystals [34,35]. In other words, the incorporation of CaCO_3 nanoparticles into hcPP can decrease the T_c and χ_c by introducing a kinetic hindrance [36]. A reduction in chain mobility by kinetic hindrance results in the formation of imperfect crystallites (β -phases) and low heat of fusion, and thus, the crystal growth of hcPP is retarded [35,37].

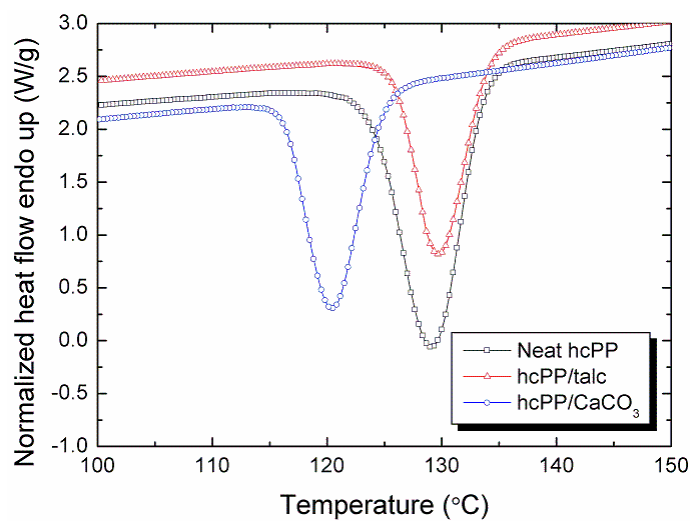
To further validate the presence of the β -phase crystals in hcPP, WAXD experiments were performed. Fig. A.6 shows the WAXD pattern of the neat hcPP and hcPP/ CaCO_3 nanocomposite. Except for the strong crystallite peaks observed for α -phase crystals, a weak peak at $2\theta = 16.0^\circ$ that corresponds to the (300) crystal plan of β -phase crystals is observed. Therefore, this confirms that β -phase is formed due to the presence of CaCO_3 nanoparticles in the hcPP matrix. It is known that the β -phase is rarely formed unless β -nucleating agents are used [38,39]. Zhang *et al.* [24] found that

the amount of β -phase PP increases as the content of surface modifier of CaCO_3 particles is increased. This means that the β -phase crystals are probably formed at or near the interface of the surface-modified CaCO_3 particles. In other words, the CaCO_3 particles may be encapsulated by the β -phase crystals. If so, it may significantly affect the toughening mechanisms and the mechanical behavior of hcPP/ CaCO_3 nanocomposite. Additional study is needed to validate this conjecture.



(a)

Fig. A.5 DSC spectra of neat hcPP and hcPP composites: (a) the melting curve and (b) the cooling curve. The arrow indicates the β -form PP.



(b)

Fig. A.5 Continued.

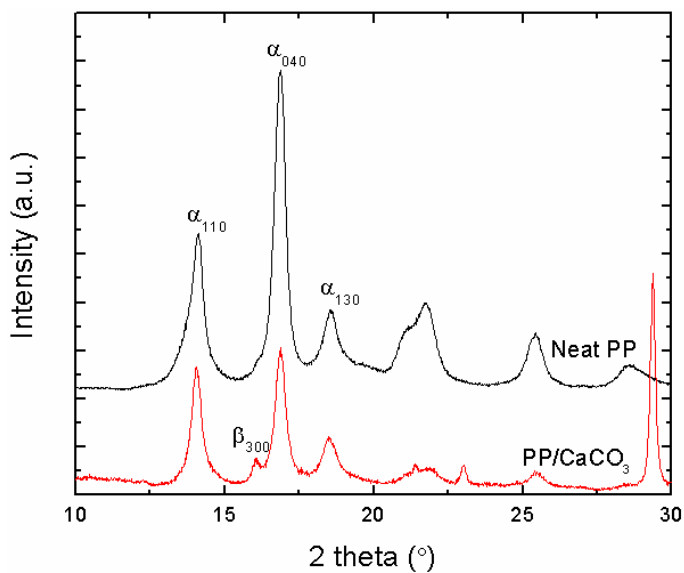
Fig. A.6 X-ray diffractions of neat hcPP and hcPP/CaCO₃ composite.

Table A.1

Summary of thermal properties of neat hcPP and hcPP composites.

Sample	T_m (°C)	T_c (°C)	χ_c (%)	T_0 (°C)	t_c (min)	T_g (°C)
Neat hcPP	167	129	48.2	136	0.7	6
hcPP/talc	167	130	48.1	136	0.6	7
hcPP/CaCO ₃	151 ^a , 165	121	46.7	127	0.6	8

T_m : peak melting temperature, ^a: T_m of β -crystals, T_c : peak crystallization temperature, χ_c : wt% crystallinity, T_0 : onset of crystallization temperature, t_c : overall time of non-isothermal crystallization ($=|T_0 - T_c|/R$), R is the cooling rate [40], and T_g : glass transition temperature obtained from DMA.

A.3.3 Mechanical properties

The effects of temperature on the dynamic mechanical properties of the neat hcPP and hcPP composites are shown in Fig. A.7. The addition of talc and CaCO₃ particles into the hcPP matrix have resulted in a considerable increase in stiffness throughout the entire range of temperature scanned, as shown by the plots of storage moduli (G') against temperature. This increase in G' is due to the reinforcing effect of talc and CaCO₃ particles. It is interesting to note that the hcPP/CaCO₃ nanocomposite shows a higher loss tangent delta curve throughout the entire temperature range investigated. This means that the hcPP/CaCO₃ nanocomposite exhibits unusual

molecular damping characteristics that may be due to the presence of the β -phase crystals around the CaCO_3 nanoparticles. These unique characteristics may have contributed to the improved toughening effects observed, as discussed below.

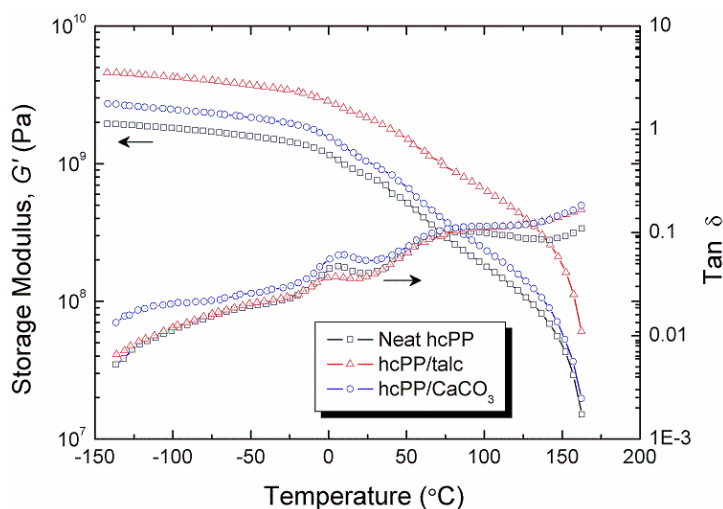


Fig. A.7 Dynamic mechanical spectra of neat hcPP and hcPP composites.

Typical engineering stress-strain curves are shown in Fig. A.8. The neat hcPP exhibits a relatively ductile tensile drawing as compared to the hcPP composites. The key tensile properties of the hcPP and hcPP composites are reported in Table A.2. As

expected, the hcPP composites exhibit higher Young's moduli and a slightly lower yield stress but a significant reduction in elongation at break. The hcPP/talc composite has a more significant increase in modulus than that of hcPP/CaCO₃ nanocomposite, due to the higher aspect ratio of talc and the talc orientation that arises from flow alignment found in the hcPP/talc composite (Fig. A.3). The large increase in modulus suggests an efficient stress transfer from polymer matrix to inorganic fillers. The decrease of yield stress is likely due to the debonding between inorganic fillers and the hcPP matrix at large deformations [21]. In particular, a higher drop in yield stress is observed for hcPP/CaCO₃, possibly due to the splitting of aggregated particles as well as debonding between CaCO₃ particles and the hcPP matrix [23].

The fracture toughnesses of the neat hcPP and hcPP composites were determined in terms of the J - R curve and J_{IC} . The J - R curve with blunting lines and exclusion lines for the hcPP/CaCO₃ is representatively given in Fig. A.9. Table A.3 shows the J_{IC} values for the neat hcPP and the hcPP/CaCO₃. It is noted that the hcPP/CaCO₃ exhibits a significant increase in fracture toughness by about 450%. In the case of the hcPP/talc composite, the addition of talc results in a slight decrease in J -integral value, which is due to the strong molecular confinement effect of talc. It should be mentioned that the hcPP/CaCO₃ does not break during the J -integral test conducted at a slow rate: on the other hand, the neat hcPP and hcPP/talc exhibit brittle unstable fracture when the crack extension is beyond 1.5 mm.

The results from the notched Izod impact strength tests, performed at room temperature, are listed in Table A.3. Macroscopically, all samples show signs of brittle

impact fracture behavior, which shows no stress-whitening or signs of plastic deformation on the fracture surface. The addition of CaCO_3 particles to hcPP does not seem to improve the notched Izod impact strength. It is well known that the toughenability of polymeric materials depends on both loading rate and temperature of testing. A higher testing rate may suppress the occurrence of some toughening mechanisms, such as crazing and shear yielding, thus causing embrittlement of the polymer. The detailed investigations of the corresponding fracture mechanisms of hcPP/ CaCO_3 under slow and fast rates are described below.

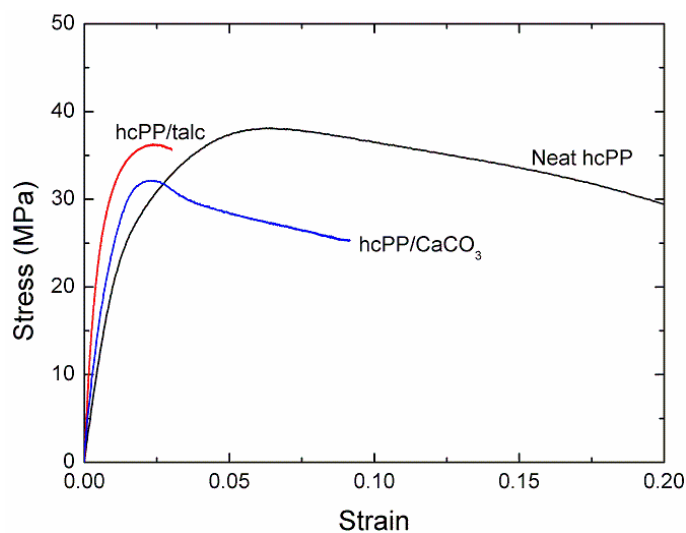


Fig. A.8 Typical stress-strain curve of neat hcPP and hcPP composites.

Table A.2

Mechanical properties of neat hcPP and hcPP composites.

Sample	Young's modulus (GPa)	Storage modulus at 25°C (GPa)	Yield stress (MPa)	Elongation at break (%)
Neat hcPP	2.10±0.11	0.80	38.1±0.18	290
hcPP/talc	4.31±0.39	1.73	34.9±0.28	4
hcPP/CaCO ₃	2.84±0.10	1.04	31.3±0.75	9

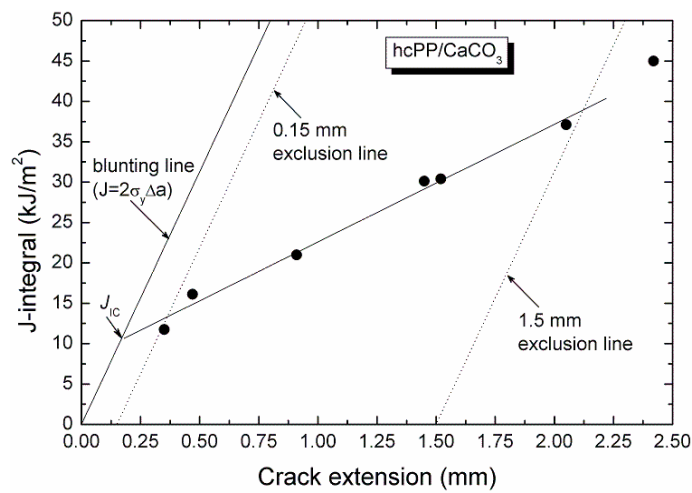
Fig. A.9 Representative J - R curves of hcPP/CaCO₃ composite.

Table A.3

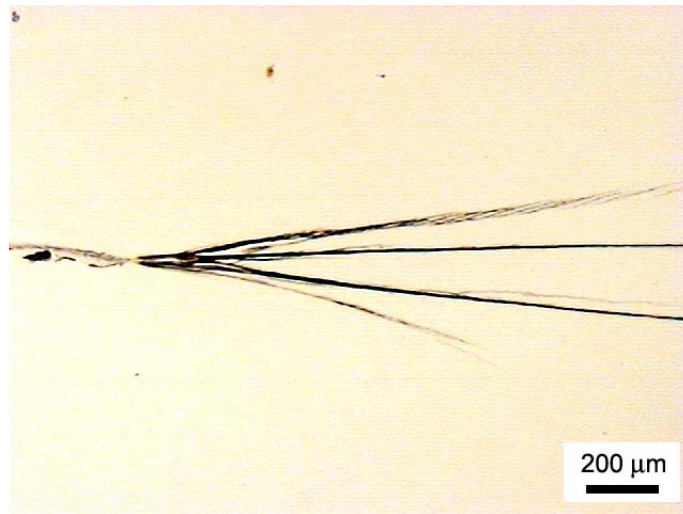
J-integral and Izod impact strength of neat hcPP and hcPP composites.

Sample	J_{IC} (kJ/m ²)	Impact strength (kJ/m ²)
Neat hcPP	2.3	2.4±0.09
hcPP/talc	1.8	2.4±0.12
hcPP/CaCO ₃	10.7	2.6±0.24

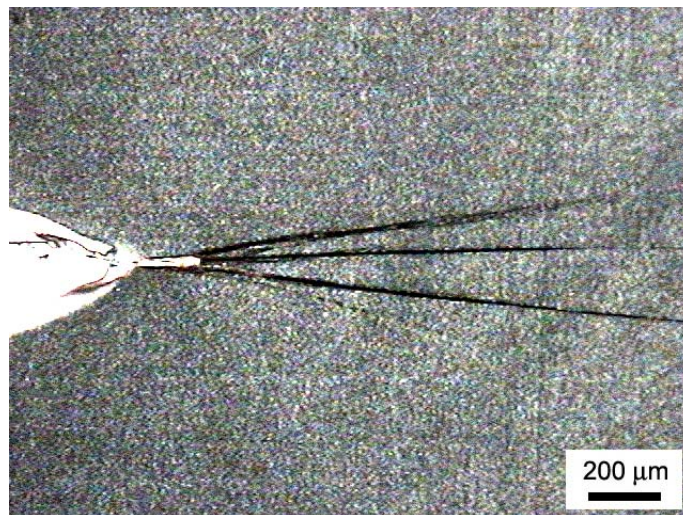
A.3.4 Fracture mechanism investigation

Toughening mechanism in neat hcPP

For comparison purposes, the toughening mechanism investigation of the neat hcPP is carried out first using TOM. Fig. A.10 shows the micrographs of a DN-4PB tested specimen. As expected, the damage zone around the crack tip shows nearly featureless crack tip damage (Fig. A.10): no sign of plastic deformation is observed. This fracture mechanism corresponds well to the observed low toughness value [41,42].



(a)



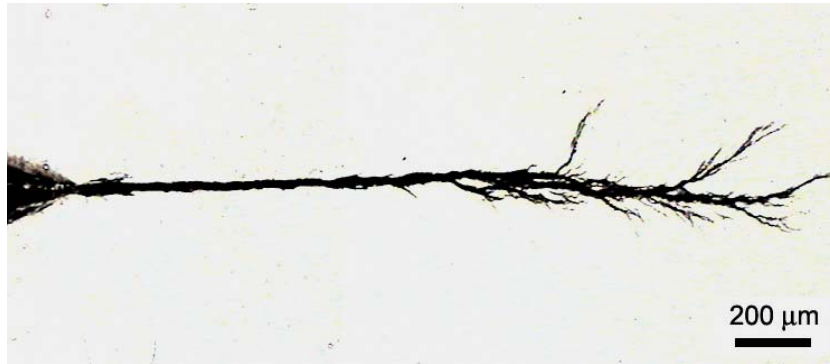
(b)

Fig. A.10 TOM of DN-4PB (0.508 mm/min) neat hcPP specimen taken under: (a) bright field and (b) cross-polarized light. The crack propagates from left to right.

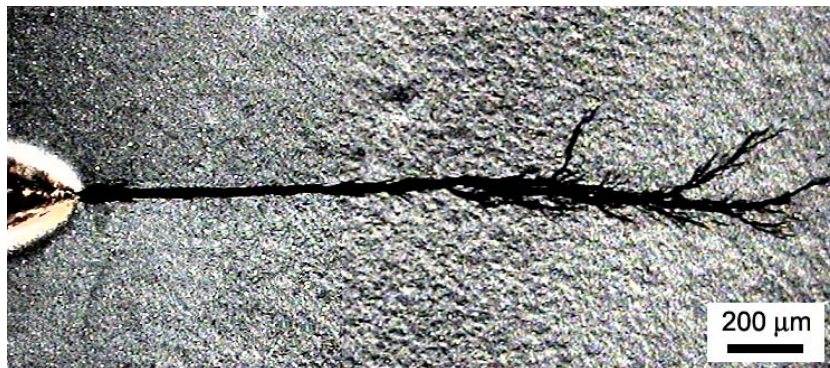
Toughening mechanism in hcPP/talc

TOM micrographs of the DN-4PB specimen of the hcPP/talc show crack deflection, microcracking, and bifurcation as the crack extends toward the edge of the specimen (Fig. A.11(a)). This phenomenon may be due to the edge effect within the specimen, where a higher degree of molecular orientation as well as talc orientation is commonly observed. No sign of birefringence is observed in the crack tip damage zone under cross-polarized light (Fig. A.11(b)). This implies that talc embrittles the hcPP matrix and leads to a lower fracture toughness. Only when the crack grows toward the highly oriented region will the less effective crack deflection, microcracking, and bifurcation mechanisms to become operative.

The TEM study performed in the sub-fracture surface zone clearly shows that the fracture behavior in hcPP/talc is in a brittle fashion (Fig. A.12). Stacked layer structure of talc is found throughout the sample. Debonding between talc particles and the hcPP matrix is also observed, indicating that the interfacial bonding is weak. Talc particles appear to be effective in generating crack deflection, bifurcation, and microcracking. These fracture mechanisms are promoted due to the dispersion and orientation of talc along the injection molded direction (Fig. A.3).

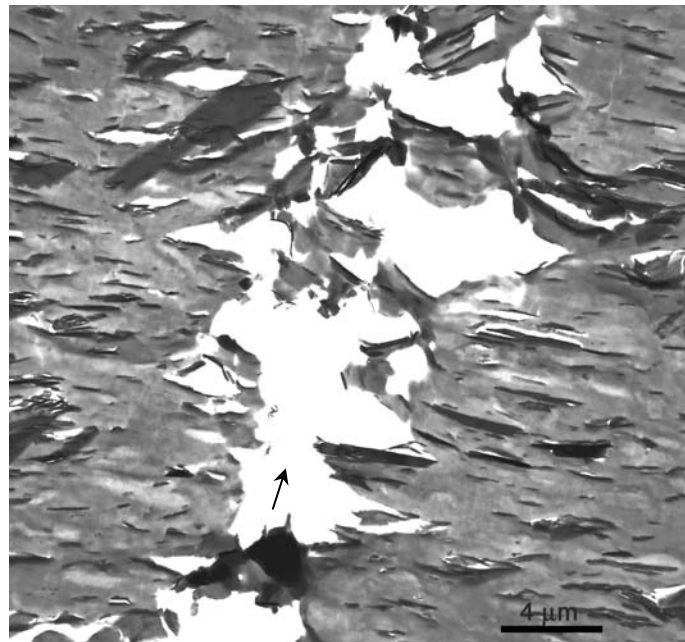


(a)

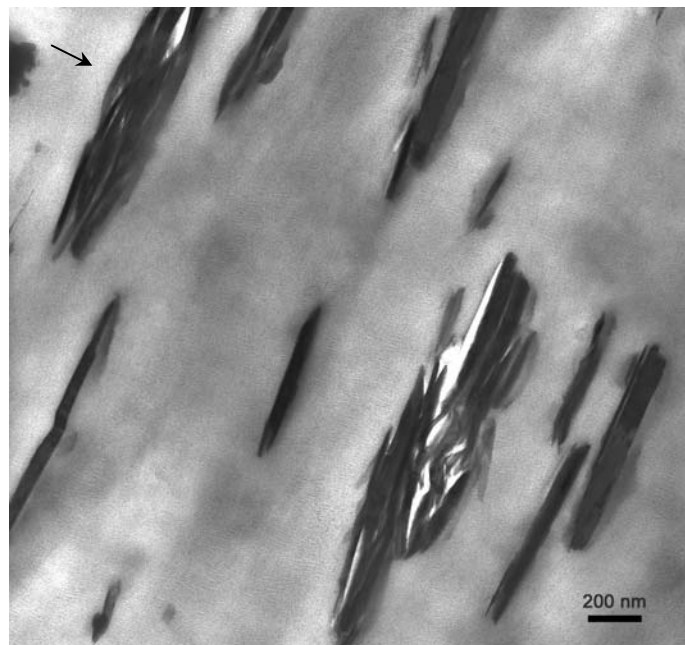


(b)

Fig. A.11 TOM of DN-4PB (0.508 mm/min) hcPP/talc specimen taken under: (a) bright field and (b) cross-polarized light. The crack propagates from left to right.



(a)



(b)

Fig. A.12 TEM micrographs of DN-4PB hcPP/talc composite taken at: (a) the crack tip and (b) undamaged region. The arrow indicates the crack propagation direction.

Toughening mechanism in hcPP/CaCO₃

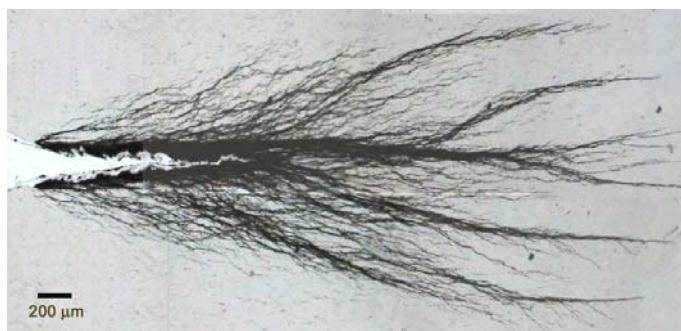
The detailed toughening mechanisms of general purpose PP/CaCO₃ nanocomposite, which exhibit significant crazing and shear banding, has been described elsewhere [11,23]. TOM micrographs of DN-4PB of hcPP/CaCO₃ nanocomposite, tested at a rate of 0.508 mm/min (slow regime), exhibit intense crazing (Fig. A.13(a)) [7,15,23]. The presence of a birefringence zone under cross-polarized light indicates that shear yielding mechanisms have also occurred around the crack tip and crack wake (Figs. A.13(b) and A.13(c)) [7,15,23]. It is noted that at slow testing speed, the toughening mechanisms observed in hcPP/CaCO₃ the same as those observed in general purpose PP/CaCO₃, but having a much smaller damage zone size.

In order to study the dependency of strain rate on fracture behavior of hcPP/CaCO₃ nanocomposite, additional DN-4PB tests under a testing speed of 50.8 mm/min and an impact speed of 3.4 m/s (i.e. Charpy impact test) were performed. At a testing speed of 50.8 mm/min, it is found that a much smaller light scattering crazing zone and an accompanying birefringent zone are formed (Fig. A.14). When the DN-4PB Charpy impact test (3.4 m/s) is performed, only a small microcrack and/or crazing zone around the arrested crack tip is observed (Fig. A.15(a)). Insignificant birefringence, if any, at the crack tip damage zone is observed (Fig. A.15(b)). As a result, a low Izod impact strength value for the hcPP/CaCO₃ nanocomposite is found. The above study suggests that the fracture behavior of hcPP/CaCO₃ is very sensitive to testing rate.

It is interesting to note that, as shown in Fig. A.16, the CaCO₃ nanoparticles appear to be capable of serving as nucleating agent to grow long lamellae in the hcPP

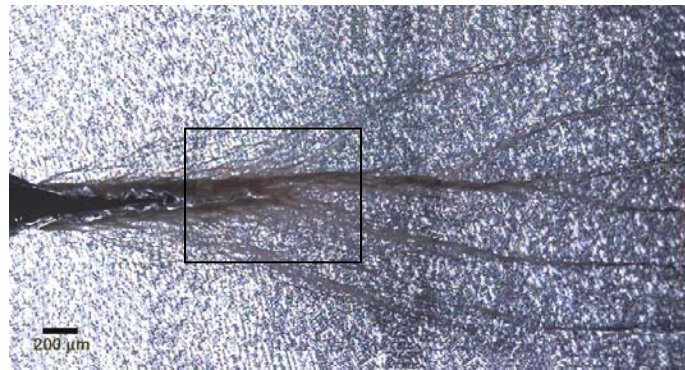
matrix. These lamellae may be those of the β -phase crystals observed from the WAXS and DSC results. If true, the main reason for the effectiveness of CaCO_3 nanoparticles in strengthening and toughening of PP and hcPP [11,21,23,24] may be its ability to nucleate the β -phase crystals around the CaCO_3 nanoparticles.

Based on the above results, the toughening process for hcPP/ CaCO_3 is proposed. Fig. A.17 illustrates a schematic of the morphological features in hcPP/ CaCO_3 . There are three key roles that the CaCO_3 nanoparticles have played to account for the stiffening and toughening of hcPP/ CaCO_3 nanocomposite: (1) the high stiffness of CaCO_3 particles, which are responsible for modulus improvement, (2) the nucleation of β -crystals around the hcPP/ CaCO_3 particles to increase the ductility of hcPP [43-46], and (3) the promotion of massive crazing and the subsequent shear banding (for the slow rate testing case). Therefore, any kind of inorganic filler particles that can help nucleate the formation of β -phase crystals would potentially improve both modulus and toughness of general purpose PP and hcPP.

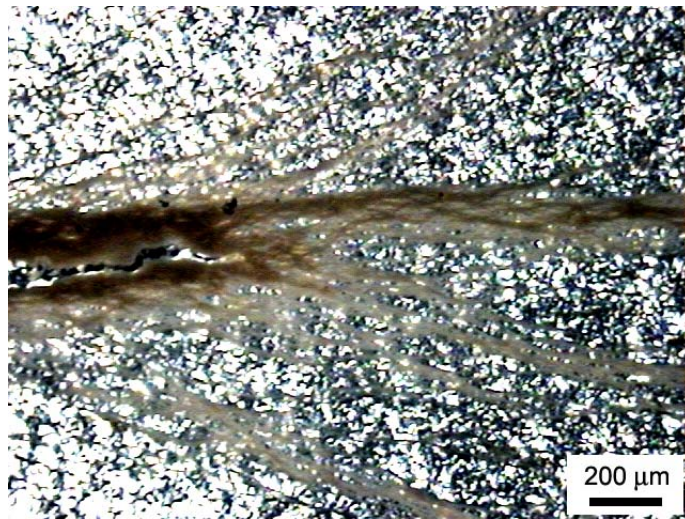


(a)

Fig. A.13 TOM micrographs of DN-4PB (0.508 mm/min) hcPP/ CaCO_3 composite taken under: (a) bright field, (b) cross-polarized light and (c) a higher magnification of (b). The crack propagates from left to right.

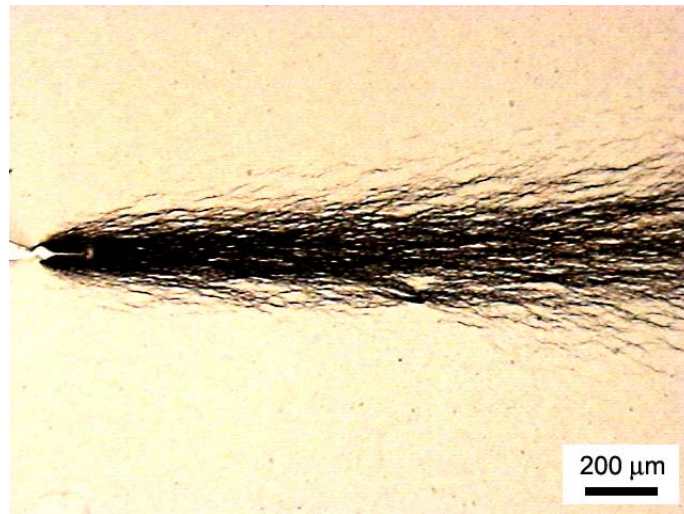


(b)

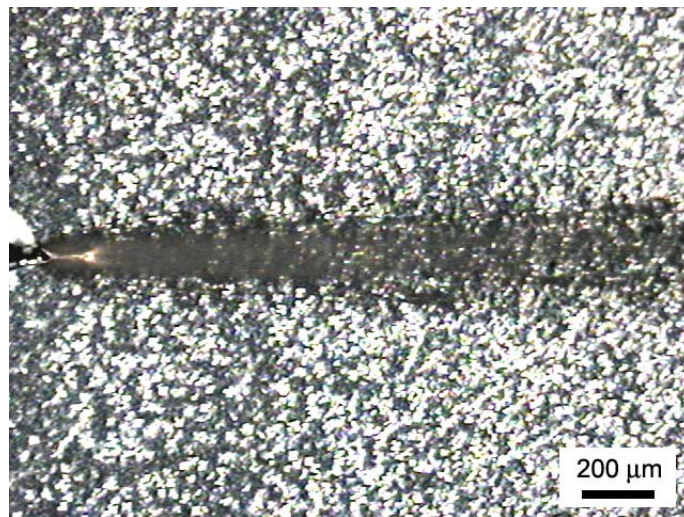


(c)

Fig. A.13 Continued.

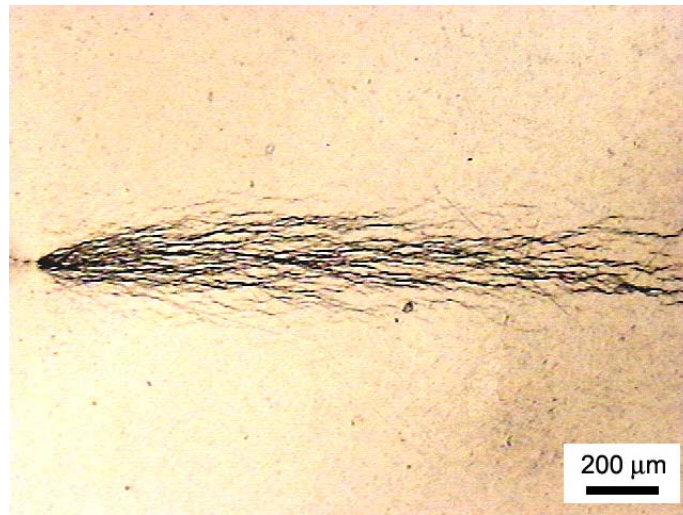


(a)

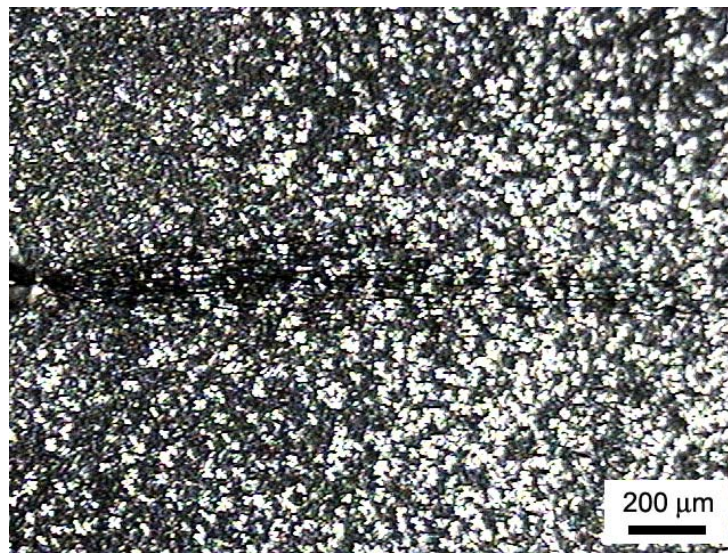


(b)

Fig. A.14 TOM micrographs of DN-4PB (50.8 mm/min) hcPP/CaCO₃ composite taken under: (a) bright field and (b) cross-polarized light. The crack propagates from left to right.

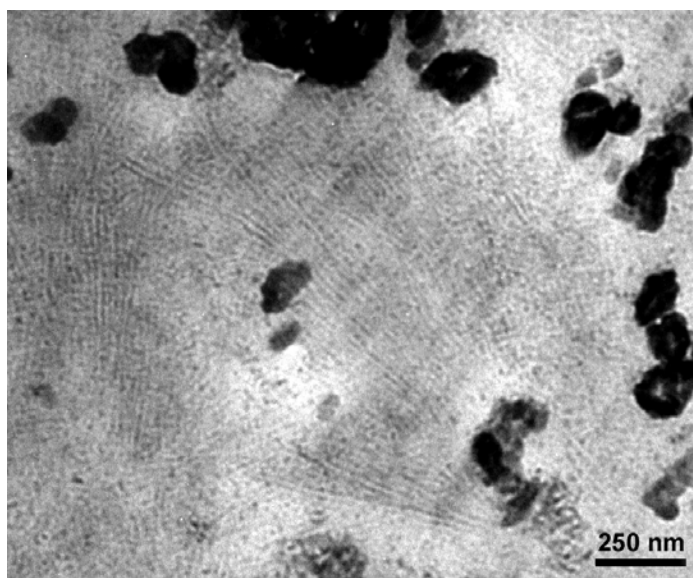


(a)

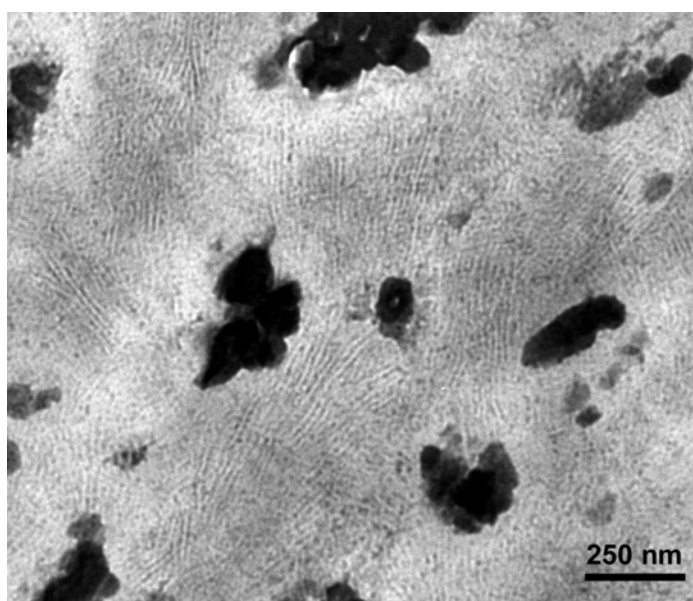


(b)

Fig. A.15 TOM micrographs of DN-4PB Charpy impact hcPP/CaCO₃ composite taken under: (a) bright field and (b) cross-polarized light. The crack propagates from left to right.



(a)



(b)

Fig. A.16 TEM micrographs taken from different regions showing the crystalline lamellae around the CaCO₃ particles of the hcPP/CaCO₃ composite.

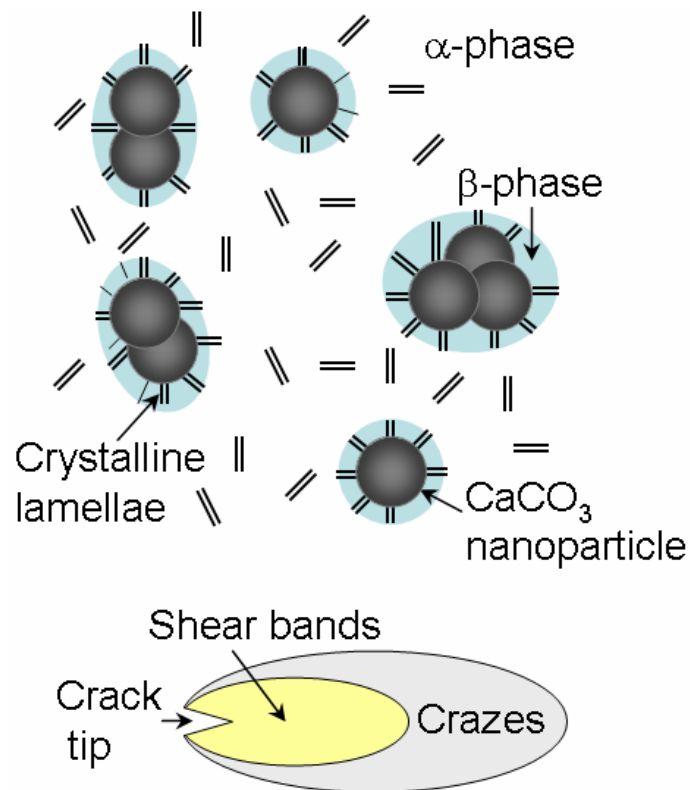


Fig. A.17 Schematic of the proposed morphological features of the hcPP/CaCO₃ composite and toughening mechanisms.

A.4 Summary

Strengthening and toughening mechanisms of talc and CaCO₃ reinforced hcPP-based composites have been examined. The high aspect ratio and high degree of orientation of talc along the tensile direction are responsible for the observed dramatic improvement in modulus. The fracture toughness of hcPP is significantly affected by the addition of CaCO₃ at slow testing speeds. It is believed that CaCO₃ nanoparticles act as

effective nucleation sites to trigger massive crazing and shear yielding in the hcPP matrix. Our results suggest that the incorporation of CaCO₃ nanoparticles into hcPP can produce attractive polymer nanocomposite with improved modulus and toughness.

A.5 Reference

- [1] Tabtiang A, Venables R. *Eur Polym J* 2000;36:137.
- [2] Wah CA, Choong L, Neon GS. *Eur Polym J* 2000;36:789.
- [3] Premphet K, Horanot P. *Polymer* 2000;41:9283.
- [4] Bartczak Z, Argon AS, Cohen RE, Weinberg M. *Polymer* 1999;40:2347.
- [5] Liang JZ, Li RKY. *J Appl Polym Sci* 2000;77:409.
- [6] Mitsubishi K, Kodama S, Kawasaki H. *Polym Engng Sci* 1985;25:1069.
- [7] Wei GX, Sue HJ. *J Mat Sci* 2000;35:555.
- [8] Jancar J, DiBenedetto AT. *Polym Engng Sci* 1993;33:559.
- [9] Demjen Z, Pukanszky B, Jozsef N. *Composites Part A* 1998;29:323.
- [10] Rothon R, *Particulate-filled polymer composites*, New York: Wiley; 1995.
- [11] Chan C, Wu J, Li J, Cheung Y. *Polymer* 2002;43:2981.
- [12] Sumita M, Shizuma T, Miyasaka K, Ishikawa K. *J Macromol Sci Phys* 1983;B22:601.
- [13] Sumita M, Tsukurmo T, Miyasaka K, Ishikawa K. *J Mater Sci* 1983;18:1758.
- [14] Fujiyama M, Wakino T. *J Appl Polym Sci* 1991;42:2749.
- [15] Wei GX, Sue HJ, Chu J, Huang C, Gong K. *J Mater Sci* 2000;35:555.
- [16] Sue HJ. *J Mater Sci* 1992;27:3098.
- [17] Wei GX, Sue HJ. *Polym Eng Sci* 2000;40:1979.
- [18] Li Y, Wei GX, Sue HJ. *J Mater Sci* 2002;37:2447.

- [19] Wei GX, Sue HJ, Chu J, Huang C, Gong K. *Polymer* 2000;41:2947.
- [20] Bartctczak Z. *J Macromol Sci Part B: Phys* 2002;B41:1205.
- [21] Thio YS, Argon AS, Cohen RE, WeinbergM. *Polymer* 2002;43:3661.
- [22] Gaymans WCJ, Westzaan C, Huetink J, Gaymans RJ. *Polymer* 2003;44:261.
- [23] Weon JI, Gam KT, Boo WJ, Sue HJ, Chan CM. *J Appl Polym Sci*, submitted.
- [24] Zhang QX, Yu ZZ, Xiea XL, Mai YW. *Polymer* 2004;45:5985.
- [25] Argon AS, Cohen RE. *Polymer* 2003;44:6013.
- [26] Fu Q, Wang GH. *Polym Eng Sci* 1992;32:94.
- [27] Bartczak Z, Argon AS, Cohen RE, Weinberg M. *Polymer* 1999;40:2331.
- [28] Sue HJ, Yee AF. *J Mater Sci* 1993;28:2915.
- [29] Sue HJ. *Polym Eng Sci* 1991;31:270.
- [30] Sue HJ, Yee AF. *J Mater Sci* 1989;24:1447.
- [31] Lu J, Wei GX, Sue HJ, Chu J. *J Appl Polym Sci* 2000;76:311.
- [32] Lu J, Li CKY, Wei GX, Sue HJ. *J Mater Sci* 2000;35:271.
- [33] Wei GX, Sue HJ. *J Appl Polym Sci* 1999;74:2539.
- [34] Zuiderduin WCJ, Westzaan C, Huetink J, and Gaymans RJ. *Polymer* 2003;44:261.
- [35] Kowaleski T, Galeski A. *J Appl Polym Sci* 1986;32:2919.
- [36] Greco R, Coppola F. *Plast Rubber Process Appl* 1986;6:35.
- [37] Maurer FHJ, Schoffeleers HM, Kosfeld R, Uhlenbroich T. Analysis of polymer filler interaction in filled polyethylene. *Progress in science and engineering of composites*. Tokyo: ICCM-IV; 1982. p.803.
- [38] Liu JJ, Wei XF, Guo QP. *J Appl Polym Sci* 1990;41:2829.
- [39] McGenity PM, Hooper JJ, Paynter CD, Riley AM, Nutbeem C, Elton NJ, Adams JM. *Polymer* 1992;33:5215.
- [40] Wu Z, Zhou C, Zhu N. *Polymer Testing* 2002;21:479.

- [41] Greco R, Ragosta G. *J Mater Sci* 1988;23:4171.
- [42] Olf HG, Peterlin A. *J Polym Sci polym phys* 1974;12:2209.
- [43] Tjong SC, Shen JS, Li RKY. *Polymer* 1996;37:2309.
- [44] Tjong SC, Li RKY, Cheung T. *Polym Eng Sci* 1997;37:166.
- [45] Labour T, Vigier G, Seguela R, Gauthier C, Orange G, Bomal Y. *J Polym Sci, Part B: Polym Phys* 2002;40:31.
- [46] Labour T, Ferry L, Gauthier C, Hajji P, Vigier G. *J Appl Polym Sci* 1999;74:195.

VITA

Jong Il Weon was born in Busan, Republic of Korea on August 1, 1970 to Yong-Ae Hwang and Yong-Hae Weon. He received his B.S. degree from Dongguk University in 1993. After completing his military service as an officer for three years, he worked for the Ssangyong Engineering & Construction, Co., Ltd. After that, he obtained a M.S. degree from Sungkyunkwan University in 1998 and then worked as a researcher in the Safety and Structural Integrity Research Center (SAFE). He joined the Ph.D. program at Texas A&M University in January 2001. His research interests include characterization and the structure-property relationship of polymer nanocomposites.

His permanent address is:

883-25 Bangbae-dong Cheocho-gu

Seoul 137-841

Republic of Korea